Titre: Title:	Upscaling Surface Treatments on Polylactic Acid (PLA) Exclusion Nets for Sustainable Agriculture
Auteur: Author:	William Simon
Date:	2024
Type:	Mémoire ou thèse / Dissertation or Thesis
Référence: Citation:	Simon, W. (2024). Upscaling Surface Treatments on Polylactic Acid (PLA) Exclusion Nets for Sustainable Agriculture [Mémoire de maîtrise, Polytechnique Montréal]. PolyPublie. https://publications.polymtl.ca/61855/

URL de PolyPublie: PolyPublie URL:	https://publications.polymtl.ca/61855/
Directeurs de recherche: Advisors:	Jason Robert Tavares, Marie-Josée Dumont, & Adya Karthikeyan
Programme: Program:	Génie chimique

POLYTECHNIQUE MONTRÉAL

affiliée à l'Université de Montréal

Upscaling surface treatments on polylactic acid (PLA) exclusion nets for sustainable agriculture

WILLIAM SIMON

Département de génie chimique

Mémoire présenté en vue de l'obtention du diplôme de *Maîtrise ès sciences appliquées*

Génie chimique

Décembre 2024

POLYTECHNIQUE MONTRÉAL

affiliée à l'Université de Montréal

Ce mémoire intitulé :

Upscaling surface treatments on polylactic acid (PLA) exclusion nets for sustainable agriculture

présenté par **William SIMON**

en vue de l'obtention du diplôme de *Maîtrise ès sciences appliquées*

a été dûment accepté par le jury d'examen constitué de :

Marie-Claude HEUZEY, présidente
Jason Robert TAVARES, membre et directeur de recherche
Marie-Josée DUMONT, membre et codirectrice de recherche
Adya KARTHIKEYAN, membre et codirectrice de recherche
Jean-Marie RAQUEZ, membre

DEDICATION

To my parents, who gave me life and the desire to understand it,

To my brother, who showed me that true fraternity is not rivalry,

To my guides and mentors, who helped me realize life is a creation.

ACKNOWLEDGEMENTS

First and foremost, I would like to express my deepest gratitude to my master's supervisor, Jason R. Tavares, for accepting me as his student. Thank you for your unparalleled guidance and all the opportunities over the past two years, including conferences, the internship at École Centrale de Lyon (thanks to LTDS!), co-peer reviewing, grading exams, teaching assistantship, volunteer work at associations and committees, and participation in events like the 3-Minute Thesis and imaging contests. And of course, thank you for diligently reading all those weekly reports!

I would also like to extend my thanks to my wonderful co-supervisors: Adya Karthikeyan, who was a great lab mentor at the beginning of my master's journey and continued guiding me as a co-supervisor, constantly challenging my assumptions and conclusions alongside the expert eye of Marie-Josée Dumont.

I am grateful to the jury members, Prof. Heuzey and Prof. Raquez for dedicating their time and interest to this work, allowing me to take one step further on the path of knowledge. This journey would not have been possible without financial support from CREPEC, RQRAD, Prima, and NSERC.

Special thanks to my hardworking interns, Thomas Badiali (quantifying slack) and Stella Bernegoue (yarn cross-section) - without your assistance, this project would have been much more difficult. Big thanks to all current and past members of the PhotoSEL team for the knowledge shared and the good times! A heartfelt thanks to Prof. Virgilio and his team for their help with the challenging microtome and for all the stimulating discussions with Arthur Lassus and Parniyan Talebpour. I am also grateful to other research teams who provided invaluable assistance during my project, including Prof. Dumont's team, Mary Hnatyshyn from Prof. Maric's team, Nila Davari from Prof. Boffito's group, and Alexandre Carriere from Prof. Santato's group.

Thanks to the Polytechnique community, including dedicated teachers, technicians, hardworking students, vibrant associations, and incredibly friendly teams (Hello, Bruno's Team!). Special appreciation to Matthieu Gauthier, Claire Cerclé, and Anik Desforges for their unwavering patience and cheerful attitude, even after countless interruptions—I promise to keep it up in the future!

I will not say much more, lest I run out of things to express in my future thesis. Thank you all for welcoming me once again! Finally, I want to thank my parents, brother, and friends for always reminding me that life should be simple: if you do not understand it today, there is a 100% chance you will figure it out tomorrow.

Recursively yours,

William SIMON

RÉSUMÉ

Ce mémoire explore la mise à l'échelle du traitement hydrophobe sur des filets d'exclusion en acide polylactique (PLA), qui offrent une alternative durable aux pesticides et aux filets en polyéthylène à base de pétrole utilisés dans l'agriculture. Les filets en PLA sont attrayants en raison de leur nature biosourcée et compostable, mais leur hydrophilie pose des défis pour les applications extérieures, entraînant une dégradation plus rapide en favorisant les croissances bactériennes et fongiques sur les cultures. Un processus de cristallisation induite par solvant en deux étapes, appelé Dip-Dip-Dry (DDD), a été développé dans notre laboratoire pour conférer des propriétés quasi-superhydrophobes au PLA en créant une surface rugueuse qui repousse l'eau. Le traitement DDD fonctionne en deux étapes sur du PLA amorphe. Le polymère est trempé dans un solvant déliant les chaînes en surface puis plongé dans un bain de coagulant pour créer un repliement de ces chaines et les figer. Dans le cas d'un matériau cristallin, une préchauffe est nécessaire pour donner de la mobilité aux chaines et faciliter l'action du solvant en surface.

La mise à l'échelle de ce traitement sur les fils de PLA a présenté des défis en raison de la mobilité limitée des chaînes provoquée par la tension appliquée pendant le processus bobine-à-bobine, ce qui a entravé la formation de la rugosité de surface. Diverses stratégies ont été explorées, notamment l'introduction d'une longueur additionnelle de fil pour donner du jeu dans le montage et permettre la réorganisation des chaînes lors du préchauffage, assurant ainsi la texturation de la surface. Il a été constaté que la température de préchauffage et la longueur supplémentaire du fil influençaient la création de la morphologie de surface. Une augmentation du rétrécissement et de la rugosité de surface se produit au-dessus d'une température critique (environ 125 °C pour le fil multifilament et 140 °C pour le fil monofilament), identifiée entre les points de recristallisation et de fusion. Cette augmentation du rétrécissement est linéairement dépendante de la longueur additionnelle donnée. Lors de la caractérisation manuelle de la longueur supplémentaire, il a été montré qu'avoir en entrée le double de la longueur en sortie permettait d'avoir une surface texturée tout en conservant des propriétés mécaniques acceptables. Les essais sur le setup en continu ont montré que les paramètres devaient être ajustée et contrôlés précisément pour éviter les ruptures de fil. Enfin, d'autres recommandations pour la mise à l'échelle du processus et d'autres procédés ont été discutés pour produire commercialement des filets de PLA hydrophobes.

Dans une optique d'éco-conception, le PLA avait été choisi pour sa compostabilité. En empêchant la stagnation de l'eau et en augmentant la cristallinité de surface du matériau, le traitement de surface est supposé ralentir le processus de biodégradation. De manière à concevoir des filets compostables, il devient donc nécessaire de concevoir un prétraitement en vue de la fin de vie de ces produits. Si la dégradation est potentiellement affectée par les propriétés hydrophobes conférées lors du traitement, alors il est nécessaire de développer un procédé permettant de revenir à la mouillabilité initiale du PLA. Une découverte clé de cette recherche est que la mouillabilité du PLA traité peut être inversée considérablement pour conférer des propriétés hydrophiles par une simple exposition de 2 heures aux rayons UVC. L'irradiation UVC provoque une scission des chaînes, réduisant d'un facteur 2 le poids moléculaire moyen provoquant une diminution des températures caractéristiques du polymère (fusion, transition vitreuse et dégradation). Aucun changement chimique majeur n'a été détecté à la surface. L'augmentation de la mouillabilité semble due à l'orientation des liaisons polaires vers la surface rendue possible par l'augmentation de la mobilité des chaines visibles par une habilité à recristalliser 10 fois supérieure des échantillons exposés aux UVC comparés à ceux non exposés. Le comportement mouillant est visible par des phénomènes d'absorption capillaire de la goutte. Ce comportement est resté stable et visible même un an après exposition indiquant la permanence des modifications induites par les rayons UVC.

ABSTRACT

This report explores the upscaling of hydrophobic treatment on polylactic acid (PLA) exclusion nets, which offer a sustainable alternative to pesticides and petroleum-based polyethylene nets used in agriculture to repel pests. PLA nets are desirable due to their biobased and compostable nature, but their hydrophilicity presents challenges for outdoor applications, leading to faster degradation and promoting bacterial growth on crops. A two-step solvent-induced crystallization process, known as Dip-Dip-Dry (DDD), was developed in our lab to impart hydrophobicity to PLA by creating a rough surface that repels water. The polymer is dipped in the solvent to slightly dissolve the surface and free some chains. Then, the polymer is dipped in a nonsolvent, which will cause polymer chains to shrivel and form recrystallized structure. In the case of crystalline samples, difficulties were encountered when trying to free some chains at the surface. A preheating step was necessary to form DDD microstructure.

Similarly, upscaling the DDD treatment for yarns introduced challenges due to the limited chain mobility caused by applied tension during the process, orienting the polymer chains and hindering surface roughness formation. Various strategies were explored, including introducing slack to enable chain reorganization, thereby improving the treatment's effectiveness. It was found that both preheating temperature and extra length of yarn influenced the surface texturation. Shrinkage was increased alongside surface texturation above a critical temperature (approximately 125 °C for multifilament yarn and 140 °C for monofilament yarn), which was identified between the recrystallization and melting points. Manual studies of the additional length provided at the entry of the treatment have shown that doubling the length at the exit of the treatment is sufficient to form surface texturation while preserving adequate mechanical properties. The study concludes with guidelines for upscaling the process and other potential ways to upscale treatment.

While the treatment prevents water stagnation, it is deemed to slow the biodegradation process due to the formation of a more crystalline surface. It was then necessary to find ways to give back compostability to the PLA material. A key finding of this research was that the wettability of a solvent-treated hydrophobic PLA (water contact angle of 147.2 ± 0.6°) can be reversed to a wicking sample with water contact angle stabilizing shortly at 22.5 ± 3.1° through a single 2-hour UVC exposure. UVC irradiation causes chain scission, significantly reducing molecular weight by a

factor of 2 and altering thermal properties. No major chemical changes were detected at the surface. Increase in wettability is deemed to come from the orientation of polar bonds to the surface that became possible from the increase in chain mobility linked to recrystallization ability which was evaluated as being 10 times greater for UVC-exposed samples. The wicking behavior remained stable even one year after exposure, indicating the permanence of UVC-induced changes.

TABLE OF CONTENTS

LIST OF TABLES

LIST OF FIGURES

LISTE OF SYMBOLS AND ABBREVIATIONS

ACA: Advancing Contact Angle

AFM: Atomic Force Microscopy

AKD: Alkylketene Dimer

AOP: Advanced Oxidation Processes

ATR-FTIR: Attenuated Total Reflectance - Fourier Transform Infrared Spectroscopy

BCE: Before Christ Era

BHC: Benzene Hexachloride

DAK: Dialkylketone

DBD: Dielectric Barrier Discharge

DDD: Dip-Dip-Dry

DIW: Deionized Water

DLVO: Derjaguin, Landau, Verwey, and Overbeek

DSC: Differential Scanning Calorimetry

DDT: Dichlorodiphenyltrichloroethane

EG: Ethylene Glycol

EG DDD: Ethylene Glycol Preheated Dip-Dip-Dry

FEP: Fluorinated Ethylene Propylene

FTIR: Fourier Transform Infrared Spectroscopy

GPC: Gel Permeation Chromatography

GUI: Graphical User Interface

HDPE: High-Density Polyethylene

IPM: Integrated Pest Management

IR: Infrared

IRDA: Research and Development Institute for the Agri-environment in Quebec

LVSEM: Low-Vacuum Scanning Electron Microscope

PE: Polyethylene

PICVD: Photo-Initiated Chemical Vapor Deposition

PLA: Polylactic Acid

PMRA: Pest Management Regulatory Agency

PP: Polypropylene

RCA: Receding Contact Angle

RH: Relative Humidity

SEM: Scanning Electron Microscope

SE: Surface Energy

TGA: Thermogravimetric Analysis

THF: Tetrahydrofuran

Tg: Glass Transition Temperature

Tm: Melting Temperature

TRL: Technology Readiness Level

UV: Ultraviolet

VUV: Vacuum Ultraviolet

WCA: Water Contact Angle

XPS: X-ray Photoelectron Spectroscopy

XRD: X-ray Diffraction

LIST OF APPENDICES

CHAPTER 1 INTRODUCTION

1.1 The early battles against pests in the context of growing crops

Combatting pests to increase agricultural yields is not new. 4,500 years ago, Sumerians already used powdered sulfur to control insects and related pests [1, 2]. Sulfur, heavy metals, and salts were the first chemical compounds discovered to act as pesticides. Heavy metals such as arsenic compounds and mercury were first used by the ancient Chinese civilizations around 1100 BCE. Then, the Romans discovered plant-based pesticides instead of mineral-based ones. They found that crushing olive pits produced an oil with the ability to kill pests. More precisely, the first pesticides used were targeting mainly insects (insecticides). Later on, chemical compounds with the ability to kill larger animals such as rodents (rodenticides) were developed, such as "Paris Green" in 1814. The need to prevent diseases and infestations of cultures from fungal or weed sources pushed science to identify new chemicals in the 19th century during the Victorian Era. This was also influenced by different large-scale blights such as the Great French Wine Blight and the Irish Potato Famine that both plagued the mid-19th century. One of the earliest known agricultural fungicides was the Bordeaux mixture, introduced in the late 19th century, in the Bordeaux region of France. This mixture of copper (II) sulfate and calcium hydroxide was found to be highly effective to combat fungal and mildew infections in vineyards. It is still used today, especially in organic farming, as a fungicide. Under the impulsion to discover new pesticides or fungicides and to improve their effectiveness, this branch of science experienced a significant boost. Rapidly, the small-scale production founded on natural extracted compounds to produce insecticide and fungicides led to the creation of a considerable synthetic pesticides industry in the 20th century.

1.2 Discovery and prime of synthetic pesticides

The first synthetic pesticides used were organochlorine compounds, such as BHC (Benzene hexachloride) and DDT (dichlorodiphenyltrichloroethane); their synthesis dates back to 1825 and 1874, respectively [2-4]. However, their use as insecticides was only discovered decades later. Chemist Paul Hermann Müller was awarded the Nobel Prize in 1948 for reporting DDT's insecticidal properties in 1939. This industrially produceable pesticide was seen as the remedy to fight diseases carried by insects such as typhus, malaria and dengue fever [5]. DDT saved

thousands of lives during World War II because it was deemed to have a low to null effect on mammals. As DDT was easy to apply and produce, it was characterized as a wonder product which eventually led to overuse, compounded by its persistence. From being overly used, DDT had a considerable impact on marine fauna and flora. The marine biologist Rachel Carson published the book “Silent Spring” in 1962 to showcase the effect of pesticides on marine biology and the food chain [6]. The increasing concentration of DDT in fish species impacted their predators such as ospreys, whose eggs became too thin and fragile to incubate, as DDT inhibits calcium metabolism in birds or more specifically calcium transport at the plasma membrane of mucosal epithelium, which diminished the thickness of the shell [7]. As such, eggs were breaking under the weight of the bird that tried to incubate them. The New Jersey osprey population declined from more than 500 pairs before 1950 to 68 pairs in 1975, an 86.4% reduction in population. Ospreys were then considered to be an endangered species in the New Jersey state alongside other water-loving birds [8]. From gathering numerous pesticides harmful consequences on the environment in Carson’s book, more control on use of pesticides was needed. The U.S. Environmental Protection Agency (EPA) canceled uses of DDT by 1972 except for countries using DDT to fight against Malaria such as India, which is today the only remaining DDT producer [9].

1.3 Problem of pesticides and commercial alternatives in the agricultural field

DDT is just one of many pesticides in use. While DDT has caused environmental damage, its effects are well understood due to several studies, which is not the case for many other pesticides currently in use. Since the 1940s, extensive research and production of pesticides has been done. According to the Health Canada Pest Management Regulatory Agency (PMRA), responsible for the introduction and regulation of pesticides in the Canadian market, there were 7 to 27 new ingredients per year between 2011 and 2021 in pesticides products sent for registration and approval. Furthermore, out of the 7600 approved pesticides in Canada, there are more than 600 different ingredients. Problems caused by pesticides are not limited only to their active compounds, but also additives used such as antioxidants, stabilizers, etc. In 8 out of the 9 most sold pesticides, additives used were found to be a thousand times more toxic than the active compound itself [10].

Pesticides’ noxious effect on the environment and our health has been widely documented in literature. A 2024 review made by Kaur et al. [11] showed different health problems arising from

different pesticides exposure based on more than 150 articles analyzed. The review summarizes the potential side effects of exposure to the most used pesticides such as organochlorine, organophosphates, carbamate, pyrethroids, and neonicotinoids. The most commonly reported harmful effects of pesticides on humans include long-term health issues, such as neurodevelopmental and behavioral disorders, birth defects, asthma, and an increased risk of cancer. The most at-risk individuals are farmers and agricultural workers, who are exposed daily to these chemicals. It has also been reviewed [12] that exposure to pesticides via food diminishes male fertility by reducing sperm count (hindering spermatogenesis) and diminishing motility by affecting sperm morphology.

From the numerous evidences of pesticides impacts on human health, fauna and flora brought to the general audience by whistleblowers such as Louis Robert [13], pesticides reduction has become a political stake despite intense lobbying from the highly influential corporations. As an example, COP15 targeted a 50% reduction of "overall risk posed by pesticides and highly hazardous chemicals" by 2030. Similar figures can be found in the Sustainable Agriculture Plan in Québec for the period ranging from 2020 to 2030. Whereas debates over promoting encouraging policies (incremental innovation) and interdictions policies (disruptive innovation) are at the heart of the political stage regarding pesticides, science is questioning the overuse of pesticides and the impact on our health. Studying the impacts of neonicotinoid seed treatments in corn and soybean cultures in Quebec, it was found that the pesticide-based treatment was only needed in less than 5% of the cases [14]. Determining when pesticides are necessary and when alternative methods, such as using predators or parasitoids, can be employed, is crucial for developing a sustainable agricultural system. This is known as integrated pest management (IPM). The strategy is to reduce pesticides usage by shifting from a toxicology point of view of killing pests, to an economical and environmental view of using the minimum required pesticides doses to ensure crop yield, while allowing some definite quantities of pests in the culture. IPM is also predicted to help in reducing growth of pesticides-resistant pests [15] compared to maintaining high doses of pesticides. Concurrently, crop yields need to increase, as it is estimated that around 700 million people suffer of undernutrition [16], despite estimates in 2009 that current practices could nourish 10 billion people [17]. Hunger is not linked to food shortage but most likely to inequalities. Poor people

cannot afford to have a nutritive diet with quality food in sufficient quantities, which also leads to waste. Gustavsson et al. found [18] that losses and wastes in the agriculture domain are tantamount to 33% of agricultural production. Being aware of this context is particularly relevant to understand that some problems relate to conservation and access to food worldwide rather than insufficient yields due to pests.

Despite this, the current world pesticide consumption continues growing [19] and pesticides still represent between 2.5 to 7% of a farmer's budget. As such, viable alternatives to pesticides are needed and being developed. Some have preconized replacing synthetic chemicals with nature-derived pesticides [11]. Nevertheless, biopesticides do not currently represent a viable solution; it is estimated that every year, we lose 2% of the insects' species and biopesticides contribute to this decline. Low environmental impact solutions include techniques such as electrostatic pest exclusion [20], plasma activated water [21] and sexual confusion practices [22]. Electrostatic pest exclusion is a promising alternative with the potential to selectively capture, repel or kill insects depending on the electric field applied [23, 24]. However, as showcased in the Jobe et al. 2024 review [25], this technique needs upscaling and more research on the type of conductors used. For example, the cost of the technique determined by the material's durability alongside the material's costs is said to be low but not determined. Furthermore, this technique seems to also share a disadvantage with pesticides: via evolution, insects might become resistant to electric fields [25].

Sexual confusion practices started in the 1980's. The principle is to deliver high amounts of sexual pheromones to avoid insects finding themselves and reproducing. Under the influence of numerous signals, insects are unable to find mates to reproduce. Other pheromones can also be used such as alarm pheromones to put insects under high stress and disable their drive to reproduce. This technique represents a promising component of an effective IPM. Nevertheless, as introduced during the early stages of this technique, the biological factor can be a limiting factor during upscaling. As shown in Klassen et al. review [26], major disadvantages are the fact that pheromones tend to be species-specific, and that pheromones are expensive ($3000/kg-$7000/kg). The cost is also related to the high purity needed for pheromone-induced confusion to be effective. Furthermore, pheromones are volatile compounds that tend to disappear by diffusion into the environment. As such, to limit costs, pheromones must be dispensed according to time of pest

occurrence and population density. In most cases, pheromone dispensing is deemed to be a secondary technique to prevent pests alongside exclusion nets, or limited use of pesticide, mass trapping or predators/parasitoids release.

1.4 Scientific approach to solve problem

As part of IPM, exclusion nets are becoming increasingly frequent. Nets act as a physical barrier to insects. By tailoring the mesh size, the nets can allow small insects to reach the culture while preventing harmful pest to enter the culture [27]. The Research and Development Institute for the Agri-environment in Quebec (IRDA), has spearheaded tests of exclusion nets and produced several articles to prove the effectiveness of exclusion nets by reducing the number of apples damaged by insects and weather (ex: hail, freezing) without hindering quality (size, weight, maturity, color, hardness, green/red color ratio, and Brix Degrees (measurement of the quantity of sugar in a solution)), and total number of apples [28-30] as seen in Figure 1.1. Furthermore, it has been shown that, contrary to pesticides, exclusion nets do not seem to effect birds' communities [31].

Figure 1.1: Image of single-row nets alongside comparative results of apple tree diameter, maturity, and total yield with and without nets. Courtesy of Larose et al. (IRDA), from presentation at the 3rd RQRAD Congress [29, 30]

Numerous studies have shown that physical barriers can be economically viable. As an example, the use of insect-proof screens for protecting tomatoes resulted in an estimated benefit of 112.9 million USD over 5 years in Israel [32]. Exclusion nets are generally made of High-Density Polyethylene (HDPE) polymer. Nevertheless, as there are generally no recycling facilities, they tend to get landfilled. Petroleum-based plastics tend to accumulate in the environment and generally require more time to degrade than biobased compostable polymers. As such, exclusion nets tend to link agricultural field to other intertwined challenging domains such as waste management, plastic pollution, climate change and more generally environmental impact. Mukherjee et al. [33] showed using life cycle assessment that biobased compostable polylactic acid (PLA) exclusion nets could be an alternative to reduce ecotoxicity impact of the exclusion nets. However, PLA tends to be more expensive than HDPE. Based on Mukherjee et al.'s values, PLA is 0.80 $/kg more expensive than HDPE. As such for PLA nets to be economically viable, the net has to have added values to the product, for example by increasing the quantity or the quality of the crop yield by reducing diseases. This also includes having a similar lifetime and equivalent or better mechanical properties as petroleum-based exclusion nets to reduce potential destruction by tearing the net.

PLA is generally produced from corn, sugar beet, maize, potato, and sugarcane. PLA has ester functional groups in its polymer-chain backbone, with hydroxyl and carboxyl groups at the end of the chain. These polar groups facilitate intermolecular interactions with water, namely through hydrogen bonding. Retained by the resulting hydrophilicity, water stagnating on a material surface can promote bacterial and fungal growth. This might cause a durability issue for outdoors applications, as it has been well documented since 1997 [34] that aerobic micro-organisms such as bacteria and fungi can degrade PLA [35, 36].

As such, the susceptibility of bioplastics towards biodegradation in humid conditions limits their usage in outdoor applications and brings about the requirement for controlled humidity during bulk storage in warehouses. Tuning the surface properties from wetting (hydrophilic) to non-wetting (hydrophobic) could optimize the behavior of bioplastics such as PLA for different periods of its life cycle i.e. hydrophobic during use and storage to prevent degradation, hydrophilic at the end of life to promote microbial attachment and thus compostability. The benefits of hydrophobicity can

vary significantly depending on the application. For instance, making agricultural nets hydrophobic can reduce humidity levels, which in turn inhibits fungal and bacterial growth. This reduction in microbial growth can lead to a decreased need for fungicide usage [37]. This can represent one way to have an added value to the net which would make financially more viable the use of a more expensive PLA nets compared to traditional HDPE or PP nets. Furthermore, as micro-organisms' actions decrease this means a more durable product, which is a positive point during usage and a point to consider during end-of-life.

1.5 Hypotheses and research objectives

To summarize, the inherent hydrophilicity or wetting of water on biobased plastics represents a problem to some applications such as agricultural exclusion nets. Stagnating water represents a medium for bacterial and fungi growth, which can lead to diseases and loss of crops. As such, water repellent properties are needed to ensure high yields when using biobased exclusion nets. Nevertheless, hydrophobic treatments might have an indirect impact on compostability of the exclusion nets. As shown in Emelyanenko et al. recent review [38], superhydrophobic surfaces help in combatting bacterial attack because of their water-repellent properties and low adhesion to substances of various natures. As such either droplets of bacterially contaminated liquids spontaneously roll off the surface and clean the surface of bacterial cells ("self-cleaning surfaces"), or hydrophobic surfaces prevent their adhesion to the surface. In both cases, the possibility of micro-organisms sticking to the surface and degrading PLA will be limited. Therefore, to address the end-of-life of surface-treated nets, an additional treatment is required to switch wettability from hydrophobic to hydrophilic, ensuring the material remains compostable.

1.5.1 General objective

The aim of this work is to explore methods for scaling up the hydrophobic treatment on polylactic acid (PLA) from the laboratory to larger applications. The goal is to produce hydrophobic, biobased exclusion nets for sustainable agriculture while ensuring that the material can be compostable, thereby addressing its end-of-life environmental impact.

CHAPTER 2 LITERATURE REVIEW

2.1 Introduction to the field of wettability

2.1.1 General introduction and theoretical model

The science of wetting is observable in our daily life. It can be seen in the kitchen with the Leidenfrost effect, which happens when liquid droplets are laid on a surface such as a frying pan heated above a certain temperature. The difference in temperature allows the formation of a layer of vapor beneath the droplet, which allows the droplet to stay and move in the pan with very low friction [39]. More commonly, water repellent surfaces for waterproof products such as raincoats, sports gear, or even self-cleaning tablecloths are already commonly found in the market. Self-cleaning surfaces for example can be water-repellent surfaces where contaminants are washed away when water is rolling off the surface. Lotus leaves, which are now regarded as the epitome of self-cleaning surfaces, were first described from a wettability point of view in 1997 by Barthlott and Neinhuis. [40].

Wettability is the part of science characterizing interaction of liquid and solid. The first basic model concerns a water droplet resting on a material surface. θ is the contact angle, r_{drop} is the contact radius of the drop, and γ_{ij} stands for interfacial tension between the i and j phases which are either s for solid, g for gases, or l for liquid (Figure 2.1).

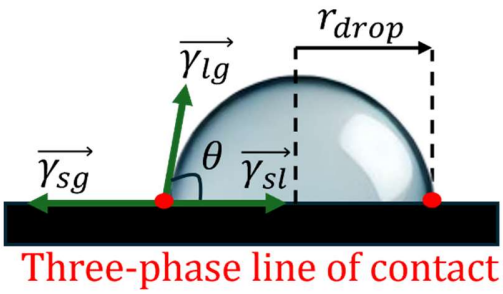

Figure 2.1: Image of droplet shape and contact angle on a flat surface resulting from balanced force equation at the gas/liquid/solid three-phase line of contact. Adapted from Bruel et al. [41]

Resulting from the balanced force equation projected on the three-phase line of contact, Young's equation is obtained (2.1).

$$\gamma_{sg} - \gamma_{sl} - \gamma_{lg}\cos(\theta) = 0 \tag{2.1}$$

This equation can also be rewritten by replacing the gas initial g by v if vapor is concerned. This equation also rearranges to calculate the contact angle (2.2) of a material.

$$\cos(\theta) = \frac{\gamma_{sg} - \gamma_{sl}}{\gamma_{lg}} \tag{2.2}$$

Formally, when referring to Young's equation, one refers to Thomas Young's essay called "Essay on the Cohesion of Fluids" published in 1805 [42]. In his work, he depicted the competition between the liquid inner cohesive forces and the liquid-solid adhesive forces [43]. This would lead to an equilibrium contact angle of the liquid on a solid that would be specific to the liquid and solid used. This can be transcribed as a mechanically balanced force equation, as seen earlier.

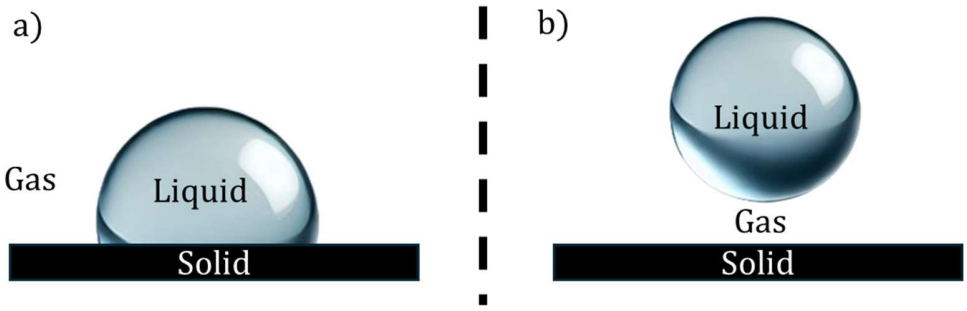

Figure 2.2: Schema for understanding Dupré's equation a) wetting b) non-wetting

Under the principle of energy minimization, wetting occurs if the solid-liquid interfacial energy γ_{sl} is lower than the sum of the solid-gas interfacial energy and the liquid-gas interfacial energy ($\gamma_{sv} + \gamma_{lv}$). This concept, depicted in Figure 2.2, is transcribed in equation (2.3).

$$\gamma_{sv} + \gamma_{lv} > \gamma_{sl} \tag{2.3}$$

By introducing the notion of work of adhesion W_{sl} to characterize liquid adhesion to the solid, the Dupré equation is found (2.4).

$$W_{sl} = \gamma_{sv} + \gamma_{lv} - \gamma_{sl} \tag{2.4}$$

Equation 2.3 can then be written as wetting occurs if the adhesion work is positive ($W_{sl} > 0$).

Moreover, taking both Young's equation and the Dupré equation, the Young-Dupré's equation is formed (2.5). For some authors, Young's interpretation would refer to the equation below rather than the one commonly known nowadays as Young's equation [44].

$$W_{sl} = \gamma_{lv}(1 + \cos(\theta)) \tag{2.5}$$

Adhesion work clearly helps to understand if the wetting of a surface occurs and how it operates. To further understand the last part, the spreading coefficient S_e will be used. The spreading coefficient is defined as the difference between the work of adhesion and the work of cohesion $W_{ll} = 2\gamma_{lv}$. The work of cohesion is obtained using Dupré's equation stating that the work of adhesion of an interface i-j with i and j phases is equal to $W_{ij} = \gamma_i + \gamma_j - \gamma_{ij}$ and as such if i and j are the same phases and there is no interface, the work is called work of cohesion and is equal to $W_{ii} = 2\gamma_i$.

$$S_e = W_{sl} - W_{ll} = \gamma_{sv} - \gamma_{lv} - \gamma_{sl} = \gamma_{lv}(\cos(\theta) - 1) \tag{2.6}$$

The expression above is only valid in the case of thermodynamic equilibrium to obtain the expression of the work of cohesion. The sign and value of the spreading coefficient will determine the behavior of the droplet on the surface. If the spreading coefficient is positive, then it means that solid-vapor interfacial tension is greater than the sum of liquid-vapor and solid-liquid interfacial tension. In other words, the forces resisting the spreading are lower than the force responsible for the increase in solid-liquid interfacial area (the "spreading" force). This means water will spread until forming a liquid film of 0° contact angle (total wetting). By comparison, if the spreading coefficient is negative, partial wetting or non-wetting occurs. Figure 2.3 illustrates equation (2.6) and correlates visible behavior of the droplet to contact angle and spreading coefficient values. The terminology of the wettability domain is also included when water is used as the probing liquid [45]. This will serve as definition for the different terms: spreading, hydrophilic, hydrophobic, overhydrophobic and superhydrophobic. In literature [46], the term 'ultrahydrophobic' is often used as a less standardized synonym for surfaces with performance comparable to or surpassing that of superhydrophobic surfaces, characterized primarily by contact angles greater than 150°. However, it is important to note that the definition of non-wetting surfaces goes beyond just a high contact

angle; it also encompasses the critical criterion of very low contact angle hysteresis, typically less than 10°. Contact angle hysteresis is later defined in detail but can be briefly described as a measure of how easily a droplet can roll off the surface. Lower hysteresis indicates that the droplet interacts minimally with the surface, allowing it to move easily and not adhere. This combination of high contact angle and low hysteresis ensures that water droplets do not stick and instead roll off effortlessly, a property essential for applications such as self-cleaning.

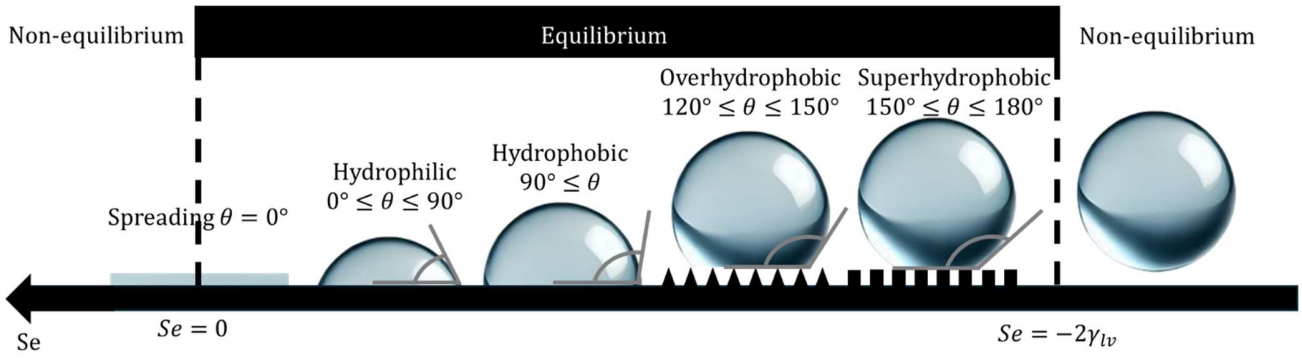

Figure 2.3: Water droplet behavior as a function of contact angle and spreading coefficient.The spreading coefficient allows to better understand the wetting of surface in the case of triple-phase line moving to increase contact angle. Alternatively, a drying parameter can be used to study the case of triple-phase line movement associated with a decrease in contact angle. This is the case if γ_{sl} is greater than $\gamma_{sv} + \gamma_{lv}$. In other words, if decreasing the solid-liquid interface allows to minimize the free energy, then the droplet will be removed from the surface by reducing contact line under the actions of surface forces. As such, introducing the drying coefficient D verifying $D = \gamma_{sl} - \gamma_{sv} - \gamma_{lv}$, if $D > 0$, then the droplet will leave the surface, and the surface will be dry. In this case, a thin gas film will separate the droplet from the solid surface like the Leidenfrost effect described earlier.

For the observant reader, it will be evident that additional pillars were introduced beneath the droplet in both the overhydrophobic and superhydrophobic regimes in Figure 2.3. The models presented were based on an ideal flat surface, where contact angle could easily be defined and was hypothesized to be only dependent on the chemistry between the solid and liquid used. As such, this angle is often called either the chemical angle or the Young angle [46]. On flat surfaces,

complete wetting can be encountered and produced by chemistry alone. However, chemistry alone has not yet been able to produce a non-wetting surface. The most hydrophobic flat materials are made of simply carbon and fluorine bonds (fluorinated materials) to avoid interactions with water. Shafrin and Zisman [47] reported in 1964 maximum contact angle value of 120° for a flat surface, which was made of methacrylic acid polymer with fluorinated side chains. Consequently, overhydrophobicity and superhydrophobicity seem unreachable for perfectly flat surfaces. This was confirmed later by Shibuichi et al. from the Kao Corporation in 1996 [48]. The experiment consisted of measuring the contact angle of water/1,4-dioxane mixtures on alkylketene dimer surfaces. Varying the content of water in 1,4-dioxane allowed to have a complete set of various contact angles on the alkylketene surfaces. Three different surfaces were tested: alkylketene dimer (AKD), 90 wt.% AKD and 10 wt.% dialkylketone (DAK), 80 wt.% AKD and 20 wt.% DAK with DAK being the product of hydrolysis of AKD. For each type, a flat and a rough surface were synthesized allowing to compare contact angles of different liquids on same-chemistry surface but with different roughness. The result is known as the Kao Diagram (Figure 2.4): a plot of the cosine of the contact angle on the rough surface θ^* (written θ_f in Figure 2.4) as a function of the cosine of the contact angle on the smooth surface θ (Young angle). Most surfaces have a certain degree of roughness. As such, the contact angle on the rough surface is called the apparent contact angle θ^*.

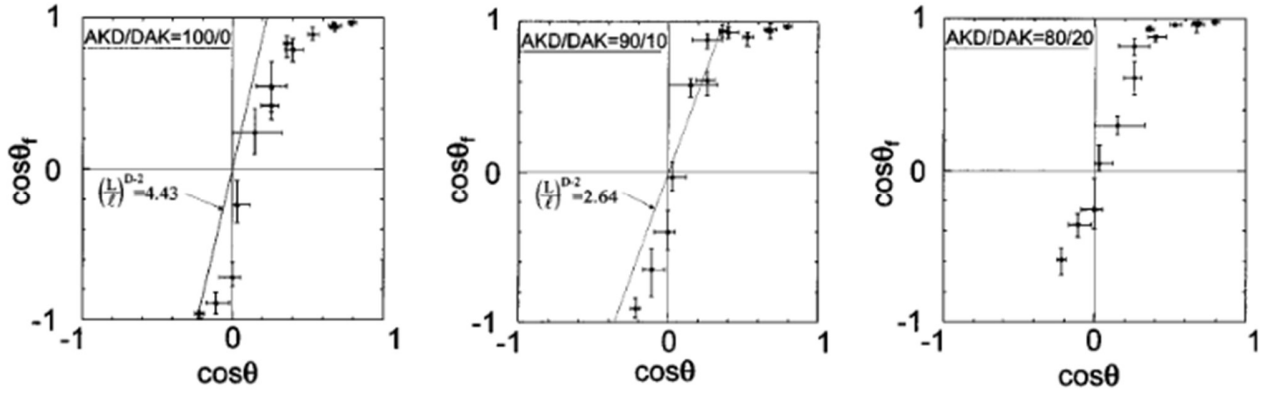

Figure 2.4: Kao diagrams for the three different AKD/DAK surfaces based on water/1,4-dioxane mixtures as probing liquids. Reprinted with permission from Shibuichi, S., et al., Super water-repellent surfaces resulting from fractal structure. Journal of Physical Chemistry, 1996.

100(50): p. 19512-19517. Copyright 1996 American Chemical Society. [48]This experiment showed that minimum and maximum value obtained for $\cos(\theta)$ are respectively approximately -0.3 and 1. This transcribed in a minimum and maximum contact angle on smooth surface equals to respectively approximately 0° and 107°. This concurs well with previous observations. This graph also shows a minimum and maximum value obtained for $\cos(\theta^*)$ of approximately -1 and 1, which depicts that full wettability spectrum, from 0° to 180°, can be obtained on a rough surface.

Roughness:

To characterize the dependence of the apparent contact angle on the Young angle, the following equation was derived by Wenzel with r being the roughness factor verifying $r = \frac{actual\ surface}{geometric\ surface}$ [49].

$$\cos(\theta^*) = r\cos(\theta) \tag{2.7}$$

This equation is obtained when considering energy variation from the displacement dx of a droplet on a rough surface as shown in Figure 2.5. This is transcribed in equation (2.8) under the assumption that water fills every microgroove and fits the surface perfectly.

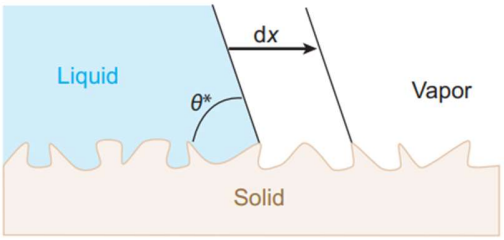

Figure 2.5: Image of a liquid droplet on a rough surface. Extracted with permission from Quéré's review
[46]

$$dE = r(\gamma_{sl} - \gamma_{sg})\,dx + \gamma_{lg}\,dx\cos(\theta^*) \tag{2.8}$$

Minimizing energy implies the derivative of the energy is equal to 0 i.e. $\frac{dE}{dx} = 0$, which means:

$$-r(\gamma_{sl} - \gamma_{sg}) = \gamma_{lg}\cos(\theta^*) \tag{2.9}$$

Using Young's equation, one can then express θ^* as a function of θ and the Wenzel equation (2.7) is then obtained. Consequently, wetting properties are proportional to the roughness, and as such to the increase in the actual surface. As the minimum actual surface is a flat surface (straight line), r is then greater or equal to 1. For flat surfaces, $r = 1$ and the Young's equation is obtained. For $r > 1$, roughness increases the natural behavior of the solid.

$$r > 1 \Rightarrow \frac{\cos(\theta^*)}{\cos(\theta)} > 1$$

If the surface is hydrophilic, $0° < \theta < 90°$ which means $\cos(\theta) > 0$ and $\cos(\theta^*) > \cos(\theta)$. In the range $\left[0, \frac{\pi}{2}\right]$, cosine is a positive strictly decreasing function which means $\theta^* < \theta$. As such the apparent contact angle will be lower than the chemistry angle and the surface hydrophilicity will be increased.

If the surface is hydrophobic, $90° < \theta < 180°$ which means $\cos(\theta) < 0$ and $\cos(\theta^*) < \cos(\theta)$. In the range $\left[\frac{\pi}{2}, \pi\right]$, cosine is a negative strictly decreasing function which means $\theta^* > \theta$. As such the apparent contact angle will be greater than the chemistry angle and the surface hydrophobicity will be increased.

Although Wenzel depicts well most behaviors of a water droplet on a rough surface, assumptions coming with this model make it non applicable to some cases, especially in the case of surfaces with extreme wettability. For example, in the case of superhydrophobic surfaces, air pockets or "plastrons" are present beneath the surface. As such, water does not infiltrate the surface. The contribution of air pockets to the increase in contact angle must be considered.

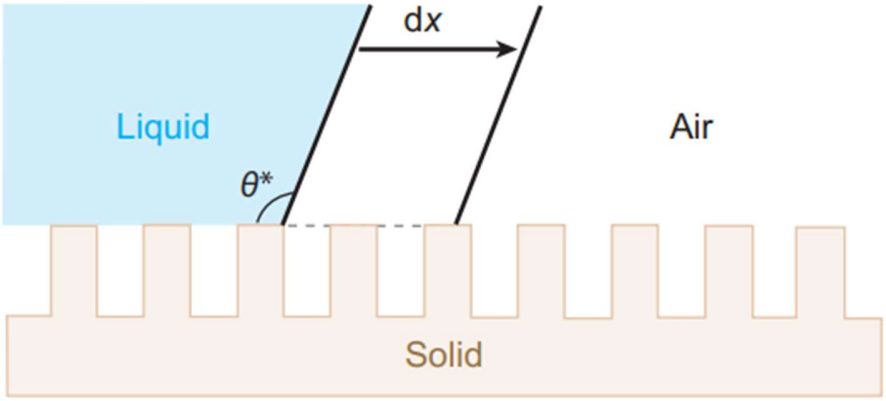

Figure 2.6: Illustration of the Cassie-Baxter regime. Extracted with permission from Quéré's review [46]In the Cassie-Baxter regime [50], the droplet sits on top of the pillars and grooves (Figure 2.6). The general model developed by Cassie [51] considers a composite contact represented by the contribution of the solid-liquid and gas-liquid interface to the apparent contact angle θ^*:

$$\cos(\theta^*) = \phi_{sl}\cos(\theta) + \phi_{lg}\cos(\theta_{lg}) \tag{2.10}$$

ϕ_{sl} is the fraction of the solid-liquid surface to the apparent total contact area, ϕ_{lg} is the fraction of the liquid-gas surface to the apparent total contact area, and $\phi_{sl} + \phi_{lg} = 1$.

θ_{lg} represents the contact angle at the ideal liquid gas interface i.e. 180° thus:

$$\cos(\theta^*) = \phi_{sl}\cos(\theta) - \phi_{lg}$$

$$\Leftrightarrow \cos(\theta^*) = \phi_{sl}(1 + \cos(\theta)) - 1 \tag{2.11}$$

The last equation is known as the Cassie-Baxter equation, developed in 1944. From the same reasoning that Wenzel applied on its solid surface, a roughness factor r_f can be added to the equation to counter uncertainty on ϕ_{sl} [52].

$$\cos(\theta^*) = r_f\phi_{sl}(1 + \cos(\theta)) - 1 \tag{2.12}$$

There is a criterion for the existence of the air pockets. Assuming flat liquid-gas interfaces, then wet and liquid surface areas are proportional to $(r - \phi_{sl})$ and $(1 - \phi_{sl})$. In order for air pockets to exist, the energy to maintain the air pockets is thus lower than the energy needed to fill them:

$$(r - \phi_{sl})(\gamma_{sl} - \gamma_{sg}) > (1 - \phi_{sl})\gamma_{lg} \tag{2.13}$$

As such, one can define from Young's equation a minimum angle $\theta > \theta_{min}$ for the Cassie-Baxter regime verifying:

$$-\cos(\theta)\,(r - \phi_{sl}) > (1 - \phi_{sl})$$

$$\Leftrightarrow\ \cos(\theta) < -\frac{1 - \phi_{sl}}{(r - \phi_{sl})} = \cos(\theta_{\min}) \tag{2.14}$$

This last equation is coherent with $\theta > \theta_{lim}$, as cosine is a strictly decreasing function in the range $[0, \pi]$. From the same logic used to find criteria, the Cassie-Baxter equation (2.11) can be proven based on energy variation and minimization $\frac{dE}{dx} = 0$ as shown below:

$$dE = \phi_{sl}(\gamma_{sl} - \gamma_{sg})\,dx + (1 - \phi_{sl})\gamma_{lg}\,dx + \gamma_{lg}\,dx\cos(\theta^*)$$

$$0 = \phi_{sl}(\gamma_{sl} - \gamma_{sg}) + (1 - \phi_{sl})\gamma_{lg} + \gamma_{lg}\ \cos(\theta^*)$$

$$0 = -\phi_{sl}\cos(\theta) + (1 - \phi_{sl}) + \ \cos(\theta^*)$$

$$\cos(\theta^*) = \phi_{sl}\cos(\theta) - (1 - \phi_{sl}) = \phi_{sl}(1 + \cos(\theta)) - 1$$

Nevertheless, the Cassie-Baxter model is based on a crenellated surface with right-angled edges. A variety of different pillars geometries can then be invented, and the equation needs to be changed. For example, Bico et al. [53] derived the equation (2.15) in case of pillars with hemispherical top layers:

$$\cos(\theta^*) = \phi_{sl}(1 + \cos(\theta))^2 - 1 \tag{2.15}$$

As such, pillars geometry can affect wettability and will be discussed further in details in another section of this literature review. As an intermediary conclusion to the superhydrophobic models developed, it can be said that by considering the solid-liquid fraction, the roughness factor and the geometry of the pillar in the equation used, researchers have ways to fit theoretical models to experimental behavior. This is also true regarding superhydrophilicity or wicking regimes, in which the liquid is absorbed by capillary action.

The spreading regime was introduced earlier. Liquid film propagation (Figure 2.7.a) will first be studied to develop on the hemiwicking state after (Figure 2.7.b).

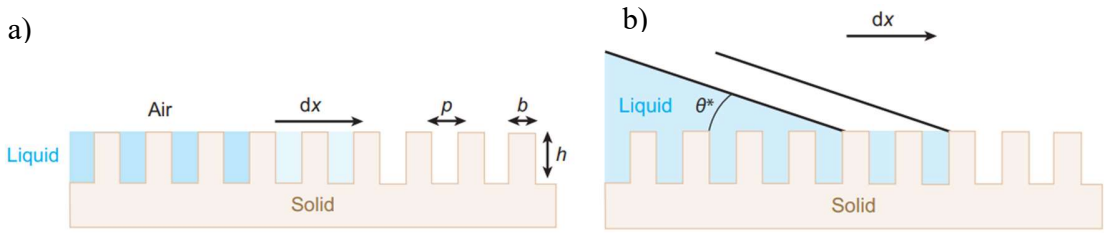

Figure 2.7: a) Liquid film propagation on a rough surface b) Hemiwicking state. Schemas extracted with permission from Quéré's review [46]

From a dx displacement, some grooves and pillars are filled. The liquid-gas interface is increased from a factor proportional to the holes top surface, which means $(1-\phi_p)$ with ϕ_p being the density of pillars. More complex, the solid-liquid interface increases by the same amount as the solid-gas interface diminishes, as microgrooves are filled. This surface change is proportional to $(r-\phi_p)$.

$$dE = (r-\phi_p)(\gamma_{sl}-\gamma_{sg})\,dx + (1-\phi_p)\gamma_{lg}\,dx \tag{2.16}$$

Propagation of the droplet arises if

$$(r-\phi_{sl})(\gamma_{sl}-\gamma_{sg}) < (1-\phi_{sl})\gamma_{lg}$$

$$\Leftrightarrow -\cos(\theta) < \frac{1-\phi_p}{r-\phi_p} \Leftrightarrow \cos(\theta) > \frac{1-\phi_p}{r-\phi_p} = \cos(\theta_{max}) \tag{2.17}$$

As cosine is a strictly decreasing function in the range $[0,\pi]$, a maximum angle is found regarding droplet propagation criterion. The hemiwicking surface is a special case where a droplet is seen alongside film propagation beneath the surface.

The variation of the apparent contact angle due to the displacement needs to be considered:

$$dE = \phi_{sl}(\gamma_{sl}-\gamma_{sg})\,dx - (1-\phi_{sl})\gamma_{lg}\,dx + \gamma_{lg}\,dx\cos(\theta^*) \tag{2.18}$$

Under energy minimization, the expression of the Cassie-Baxter equation for hemiwicking surfaces is obtained:

$$\cos(\theta^*) = \phi_{sl}\cos(\theta) + (1-\phi_{sl}) = 1 + \phi_{sl}(\cos(\theta)-1) \tag{2.19}$$

In other words, taking the Cassie rule of composite contact and applying $\theta_{lg} = 0°$ for a hemiwicking surface, we loop on the same result. Consequently, the hemiwicking regime is also called the Cassie impregnating regime [54].

$$\cos(\theta^*) = \phi_{sl}\cos(\theta) + \phi_{lg}\cos(\theta_{lg}) = \phi_{sl}\cos(\theta) + \phi_{lg} = \phi_{sl}\cos(\theta) + (1 - \phi_{sl}) \quad (2.20)$$

Although numerous works [55-61] have shown some limitations and hypotheses inherent to the Cassie and Wenzel models, plotting the different regimes shown (Cassie-Baxter hydrophobic regime, Wenzel regime, and Cassie impregnating regime) in a Kao diagram alongside experimental measurements, has shown great success in fitting experimental data, as illustrated by Quéré and his team in Figure 2.8 [46, 53]. Limitations and hypotheses are presented in Appendix A. This introduction to wetting forms the basis to understand the next sections on how to assess wettability (section 2.1.2), how to modify a surface to impart hydrophobicity (section 2.1.3) and then going to the specific wettability case of textiles (section 2.1.4).

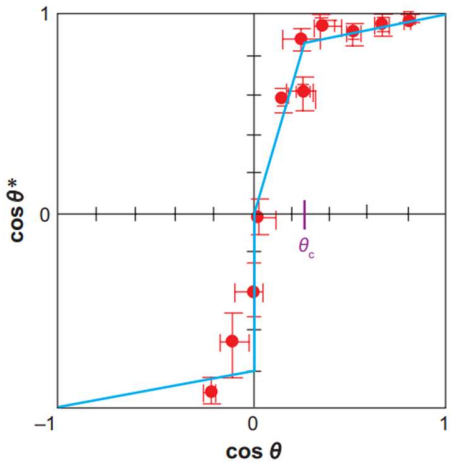

Figure 2.8: Illustration of a Kao diagram. The blue straight lines are respectively Equation 7, 8 and 9 reading from left to right. Extracted with permission from Quéré's annual review [46]

2.1.2 Assessing wettability

As shown earlier with the different regimes and contact angles, there exists a variety of wettability behaviors. To quantify and qualify the different surfaces, different techniques have been used based

on either contact angles or on interfacial tensions, which are linked via Young's equation and can both be used to characterize wettability.

Contact angles-based methods:

The simplest and most widespread method to get a static contact angle is the sessile drop method using an optical tensiometer (Figure 2.9.a). The idea is to lay a 1 to 5 µL droplet on a solid surface and measure the corresponding angles formed between the three-phase contact line and the tangent to the droplet profile (Figure 2.9.b). The volume of the droplet should be kept constant as it has been shown to have an effect on the contact angle [62, 63]. Accuracy to the order of microliters is obtained using thin needle connected to a high-pressure automated pump. A high-resolution camera is used to obtain high magnification of the contact line. Studying both the left and right sides of the droplets in contact with the solid surface can give a first estimate of the accuracy of the test. This method has allowed to show the numerous parameters affecting wettability such as relative humidity [64], time after laying droplet, or small changes in surface topography, as will be discussed in the section 2.1.3. This test is particularly simple and convenient, but accuracy is quite dependent on operator experience and adherence to protocols. As shown in the Laplace theory, there are a multiplicity of equilibrium drop shapes providing different apparent contact angle for a given volume [65]. As such, it is quite common to encounter at least a ±2° uncertainty in the contact angle measurement [66]. Generally, 2 to 5 drops per surface are studied on three substrates to ensure homogeneity and repeatability.

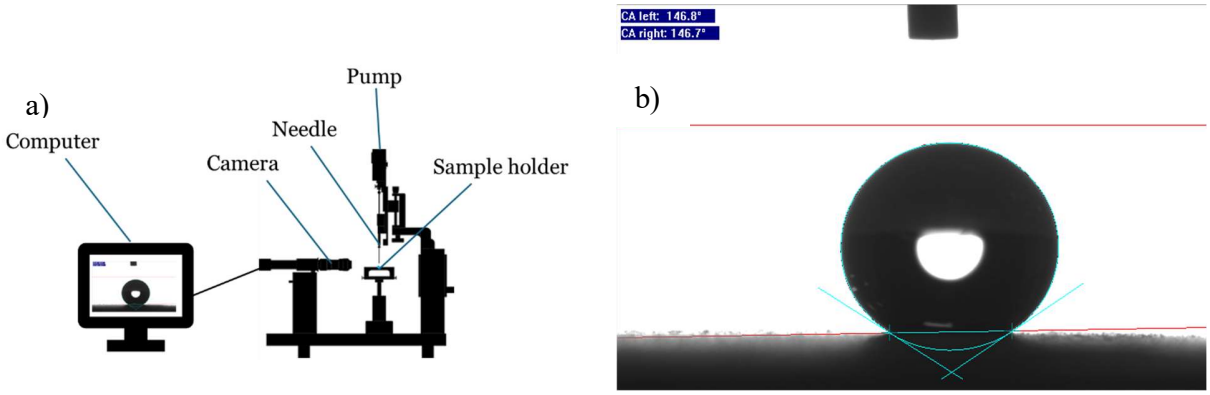

Figure 2.9: a) Schema of the tensiometer adapted from Dataphysics icon b) image of a water droplet on a surface-treated substrate obtained from high-resolution camera in the tensiometer

In the case of water spreading or superhydrophilic regimes with an apparent angle below 10°, tangent assignment can be unprecise. For high surface free energy materials or porous materials such as hydrogels, a variation of this method called the captive bubble method was created. The surface is submerged in a liquid bath. An air bubble is laid on the surface using an inverted needle, and the contact angle is measured on the recorded video using a high-resolution camera. This test has some advantages as well as some disadvantages [66]. First, the surface is saturated with the liquid, which prevents the contribution of liquid adsorption over time from the surface that can be seen in the sessile drop method. Surrounding liquid prevents droplet evaporation. In both cases, the disadvantage associated is the necessity of liquid in high quantities. Probing liquids used to test wettability can be inexpensive and stable (ex: water) or costly and subject to degradation (ex: diiodomethane). This technique also requires the air bubble to be visible when under the liquid, which means only translucent liquids can be used. Finally, this technique allows to study some parameters more precisely, such as control over the environment temperature and dynamic control of the liquid concentration.

Both techniques can also be used dynamically by increasing or decreasing the droplet or the bubble volume, while still being attached to the tip of the needle. Adapting volume by injecting and withdrawing probing fluid can give additional information on the wettability behavior such as the advancing and the receding contact angles respectively shortened as ACA and RCA (Figure 2.10).

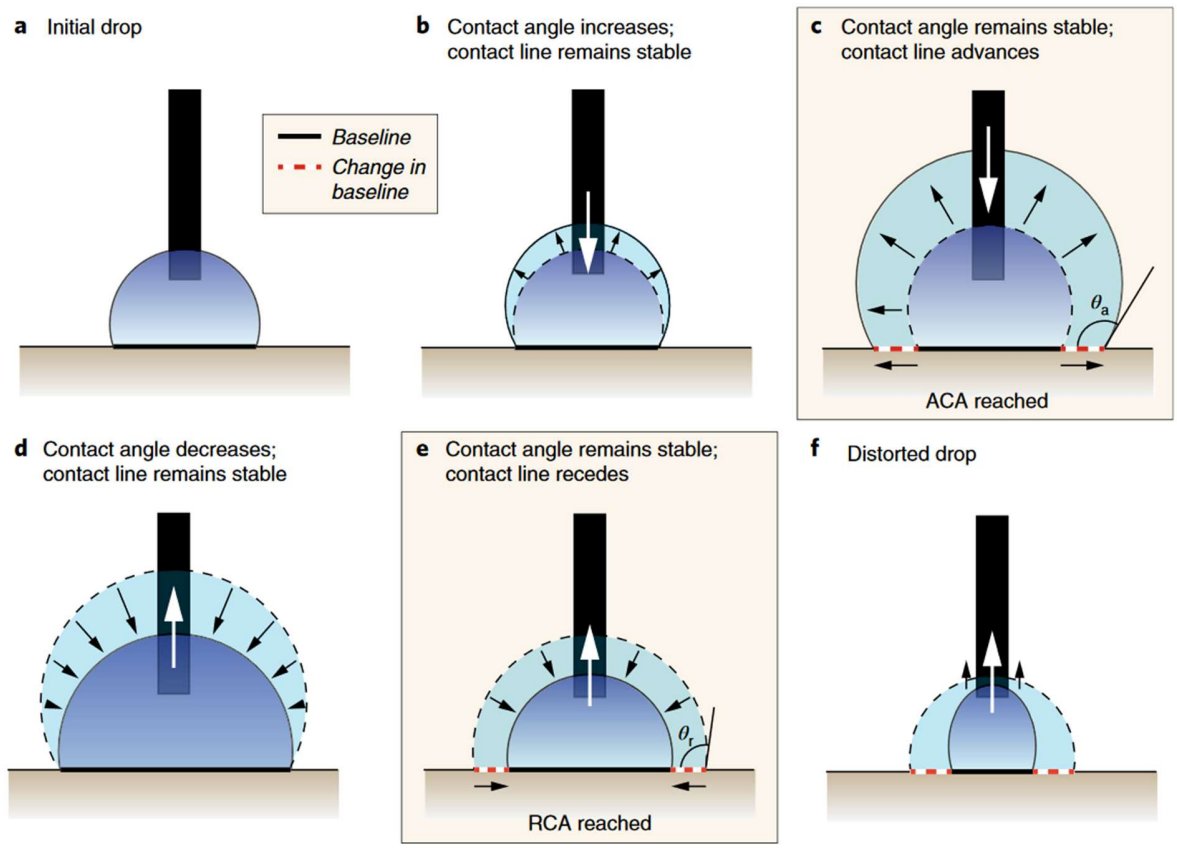

Figure 2.10: Phases during an ACA-RCA measurement test. Reprinted with permission from Huhtamäki et al. [67]In the first phase of the test, a millimetric drop is dispensed onto the surface of interest. As the volume increases, two phases appear. In the first phase, the contact points of the droplet are pinned, and the contact angle increases due to water injection and increasing volume. Then, at some point the triple-phase line will move, which defines the second phase. The increase in volume is then correlated with an increase in surface area at the interface as the contact angle cannot overshoot a maximum value. The contact angle measured just before the movement of the triple-phase line is the ACA. Similarly, when water is withdrawn, the contact angle will first decrease as the droplet volume decreases without movement of the contact points. Eventually, the triple-phase line will move in a second phase and the minimum angle before the movement is called the RCA.

As the volume tends to grow above the first ACA observed in the advancing phase (image 12.c), multiple contact angles values can be obtained when doing a test. Similarly for receding phase,

when water is withdrawn below the first RCA observed, numerous values of RCA can be obtained. Multiple values of advancing and receding contact angles help in having a first sight of the accuracy of this technique called needle-in-drop. During the test, a large amount of data is generated. In order to improve accuracy by selecting the exact time corresponding to the movement of the droplet and to improve repeatability and reproducibility among researchers, Professor Kietzig and her lab developed a graphical user interface (GUI) to automatically analyze needle in drop test videos [68]. Figure 2.11 was extracted from their article to depict the notion of movement of the droplet during the test plotted by the GUI named ARCA finder, alongside the epitome of the notion of numerous equilibrium contact angles that can be obtained during a test due to surface roughness. By putting threshold into the variation of the contact points, noises or non-significant movement (or "pseudo-movements") can be filtered.

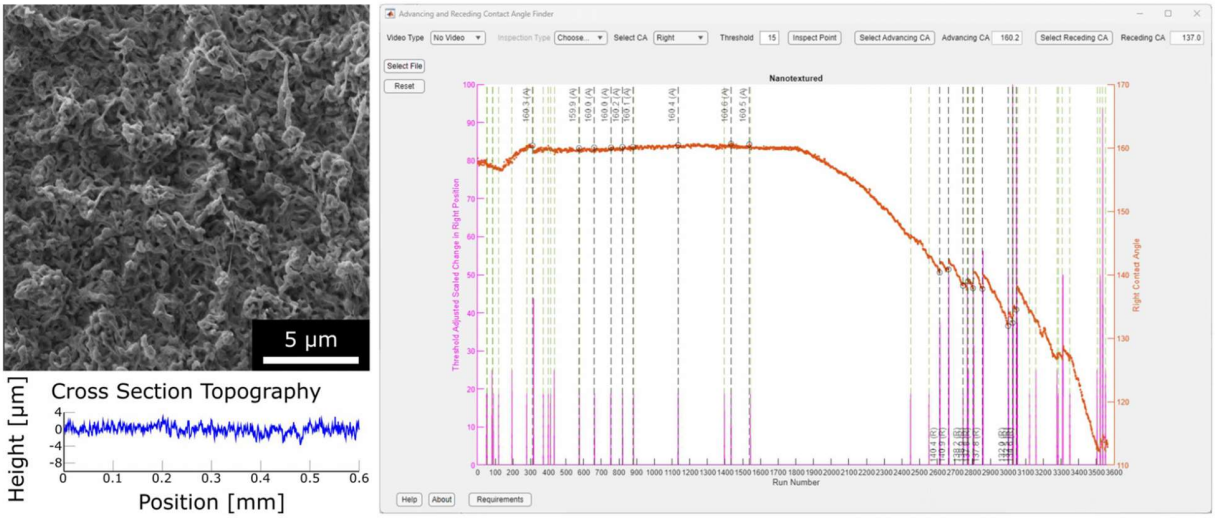

Figure 2.11: SEM image and needle-in-drop test analyzed by ARCA finder on nanotextured PTFE data (advancing phase from run number 1–1550, equilibrium phase from 1550 to 1850, and receding phase from 1850 to 3600). Extracted with permission from [68]

The needle-in-drop technique is one of the most widespread techniques due to its simplicity. This method is particularly useful to measure hysteresis (defined below), which is a key element in the wettability field. As depicted earlier there can be multiple equilibrium contact angles when studying a heterogeneous surface. The link between heterogeneity and creation of metastable states

local minimum in Gibbs free energy) compared to an ideal surface according to Gibb's free energy is presented in Figure 2.12.

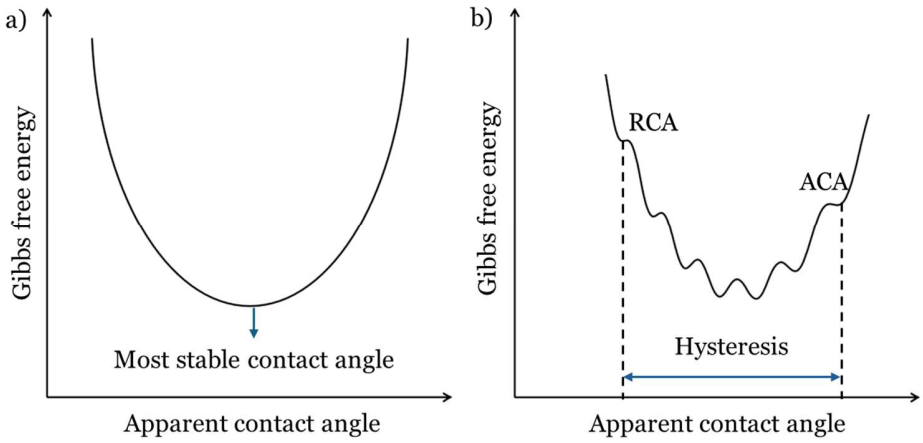

Figure 2.12: Schema of Gibbs free energy as a function of the apparent contact angle for a) an ideal surface b) for an heterogeneous surface. Adapted from [67] with permissions

Hysteresis H is defined as the difference between the ACA and the RCA, with ACA being always greater than RCA for heterogeneous surfaces and equals to RCA for ideal surfaces ($H = 0$). The shape and angle on a heterogeneous surface are dependent on the history of the spreading process, especially ACA and RCA being rate-dependent for high capillary number. The capillary number N_{Ca} represents the ratio of viscous forces to the interfacial forces (Equation 2.21):

$$N_{Ca} = \frac{\eta_l v}{\gamma_{lg}} \tag{2.21}$$

η_l being the dynamic viscosity of the liquid, v being a characteristic liquid velocity and γ_{lg} the liquid - gas interfacial tension [69]. For low capillary number ($N_{Ca} < 10^{-5}$), viscous forces are low enough that triple phase line movement does not induce variation of the contact angle, which would mean a thermodynamically stable state [41] and stable contact angle depicted in Figure 2.10.c and 2.10.e.

Similar as the sessile drop method, the needle in drop method can also be adapted to the captive bubble technique where an air bubble is grown onto a surface submerged in a liquid [70]. Other methods to measure ACA and RCA exist such as the tilted version of the sessile drop method known as the tilted plate. There are also two variations of this method. In the first case, a droplet is laid on the surface of interest fixed to the support holder. Then, the angle β (Figure 2.13) is increased from 0° (horizontal) to 90° (vertical) until the droplet moves at specific angle called slip angle. Using the last images before the droplet slides, one can find the minimum and maximum contact angle of a liquid on a specific substrate.

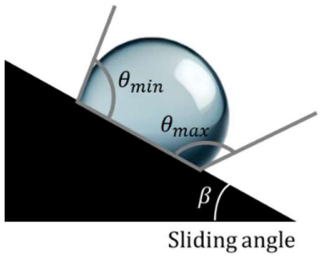

Figure 2.13: Schema of the tilted plate method using a droplet with sliding angle

This method has some disadvantages such as in some cases, for example high hysteresis, the droplet does not slide. Furthermore, no trivial link exists between θ_{min} and θ_r, or θ_{max} and θ_a. Theoretically, Krasovitski and Marmur [71] showed that for hydrophilic solids, the simplification $\theta_a = \theta_{max}$ could be done as shown in but that for all the other cases the ratios $\frac{\theta_{max}}{\theta_a}$ and $\frac{\theta_{min}}{\theta_r}$ could be different than unity. These results are in contradiction with experimental results from Extrand and Kumagai [72] and the model developed by El Sherbini and Jacobi [73], which fits the previous data with a root mean square error of 0.98. Model used by El Sherbini and Jacobi come from the model developed by Wolfram and Faust for a droplet with a circular contact zone, which was expanded and applied by Furmidge, Extrand and Gent for parallel sided and elliptical contact line [74]. Nevertheless, as shown by Pierce et al. [75], the assumption of $\theta_{max} = \theta_a$ and $\theta_{min} = \theta_r$ can generally be considered valid for angles below 130°. In the case of surfaces with extreme wettability such as superhydrophobic surfaces, results have been shown to diverge from model.

The second method, also called the tilted plate method, consists of letting a plate rest on top of water and immerging one end for two menisci to form on the two sides of the plate. After rotating the plate, one of the menisci will become flat and angle between the flat liquid and the plate forms the contact angle as seen in Figure 2.14.

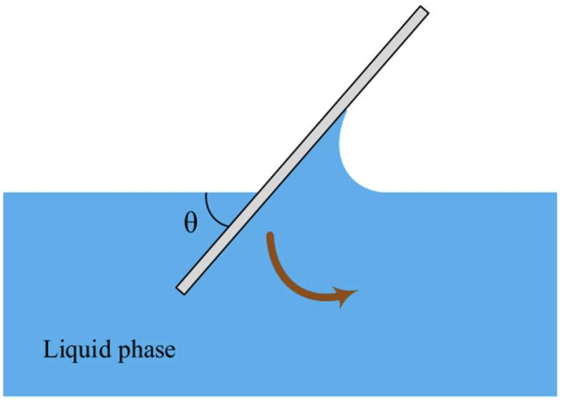

Figure 2.14: Tilted plate method variation using a large liquid bath. Extracted without modification from [66]. License: CC BY 4.0

This method is highly dependent on the operator skills and as shown earlier when tilting the liquid, correlations to obtain the advancing and receding angle is not trivial. In the same vein, the Wilhelmy plate and the capillary rise methods exist.

In the Wilhelmy balance method, a solid plate is slowly dipped vertically in a liquid bath and the angle formed between the liquid meniscus and the plate can be estimated [66]. More accurately, force tensiometers can measure the force variation on the plate due to contact with liquid. When inserting and withdrawing the plate, the advancing and receding angles can respectively be determined in the force diagram by extrapolating the values to volume displaced (dotted line on Figure 2.15).

$$f = \gamma_{lg} p \cos(\theta) - V \Delta\rho g \tag{2.22}$$

In this equation, f is the force variation applied on the plate, p is the perimeter of the substrate, θ is the angle formed between the liquid and the plate, γ_{lg} is the liquid-gas interfacial tension, V is the displaced volume, $\Delta\rho$ the liquid-gas density difference, and g is the acceleration of gravity.

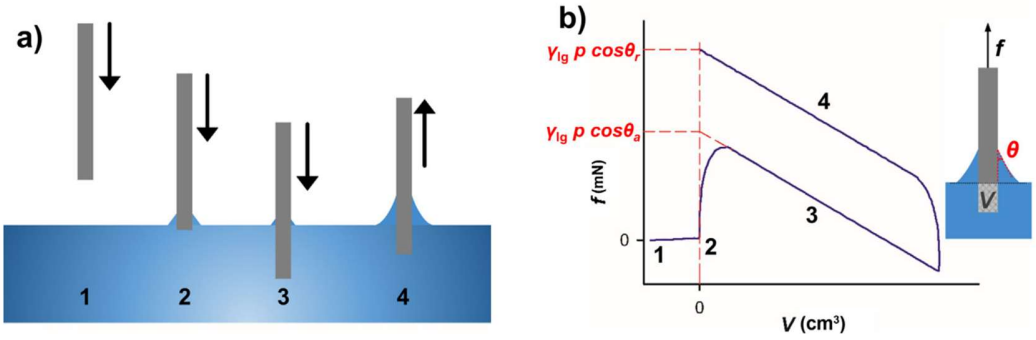

Figure 2.15: Wilhelmy balance method: (a) during test, the plate is pushed into the water (1,2) until immersion (3) and then withdrawn (4). b) Force variation f is plotted as a function of displaced volume alongside extrapolation to obtain ACA and RCA. Figure extracted with permission from [41]

Tests based on measuring force variation due to liquid-solid interfacial tension are numerous. Generally, force sensors or strain gauges are used to record the force variation. Other elements than a plate can be used as long as the equation to obtain liquid-gas interfacial tension is adapted. For example, a ring can also be used [76]. This method is sometimes called Lecomte de Noüy ring after the name of the scientist who developed a setup to make the method rapid and convenient [77]. Inversely, the force sensor can be attached to the syringe, the droplet is put in contact with the solid surface and then the force needed to pull off the droplet is measured. This is called the drop-adhesion test and requires specific surface and needle properties for droplet not to detach from the syringe.

The last type of method commonly used is the Washburn capillary rise method (Figure 2.16.a). This method consists of immersing a capillary tube filled with powders in the liquid and studying the liquid propagation in the capillary as a function of time. There are 3 phases (Figure 2.16.b) during this test and the second phase holds the key to estimate the advancing contact angle from Equation 2.23:

$$h^2 = \frac{r_{eff}\gamma_{lg}\cos(\theta_a)}{2\eta_l}t \tag{2.23}$$

h is the liquid height in the capillary, r_{eff} is the ideal cylindrical pore radius, t is time and η_l is liquid dynamic viscosity.

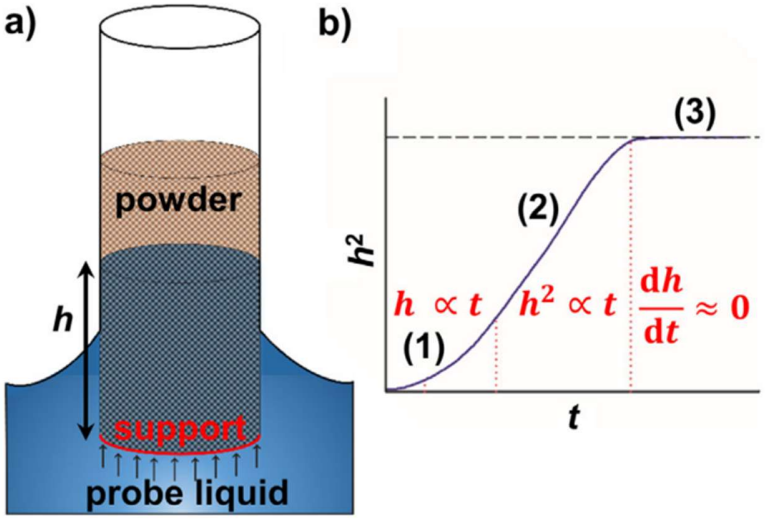

Figure 2.16: a) Schema of the Washburn capillary rise and b) the different regimes during capillary tube immersion. Extracted with permission from Bruel et al. [41]

This method does not provide information regarding the receding angle and hysteresis. Although this method is specifically used for powders with an average particle diameter between 15 and 200 µm, a variation exists for solid surfaces that is very similar to the Wilhelmy plate method. Instead of one plate slowly dipped into water as in the Wilhelmy method, two small parallel plates are dipped into water simultaneously. The water rises between the two plates and forms a curved surface. Integrating the Laplace equation allows to obtain an equation relating the contact angle with the liquid height between the two plates similarly to how the water would raise in the capillary tube.

Interfacial tension-based methods:

Less direct methods can involve the direct measurement of interfacial tensions. The greater the difference in interfacial tension between the liquid and the top surface, the less likely the wetting is observed. Measuring the interfacial tension of liquids or molten polymers is generally done using

the pendant drop method [78], the sessile-drop and captive-bubble methods [79], or the breaking thread method [80, 81].

The first equation developed to correlate the surface free energy of a liquid and a solid to the interfacial tension and ultimately the contact angle was given by Good and Girifalco. Starting from the work of adhesion obtained in the previous equation from the work of Dupré:

$$W_{ij} = \gamma_i + \gamma_j - \gamma_{ij} \Leftrightarrow \gamma_{ij} = \gamma_i + \gamma_j - W_{ij} \tag{2.24}$$

Introducing an interaction parameter ϕ to take into account molecular interaction:

$$\phi = \frac{W_{ij}}{\left(W_{ci}W_{cj}\right)^{\frac{1}{2}}} = \frac{W_{ij}}{\left(2\gamma_i * 2\gamma_j\right)^{\frac{1}{2}}} = \frac{W_{ij}}{2\left(\gamma_i\gamma_j\right)^{\frac{1}{2}}} \tag{2.25}$$

The Good and Girifalco equation is found (equation 2.26) and can be combined with Young's equation to be related to the contact angle, assuming surface free energies are equal to interfacial tension formed when air is the medium i.e. $\gamma_{sg} = \gamma_s$ and $\gamma_{lg} = \gamma_l$.

$$\gamma_{ij} = \gamma_i + \gamma_j - 2\phi\left(\gamma_i\gamma_j\right)^{\frac{1}{2}} \tag{2.26}$$

Different variations of the Good and Girifalco equation have been developed to further match data to a theoretical model and identify specific interactions such as dispersive and polar interactions, written respectively as follows ${\gamma_{ij}}^d$ and ${\gamma_{ij}}^p$. Commonly used models based on dispersive and polar interaction are the Fowkes equation, the Owens and Wendt equation or Wu's equation. Kitazaki and Hata added a term to account for hydrogen bond interactions. Finally, the latest model is the Lifshitz-van der Waals acid-base approach and its variations, where Van der Waals interactions and acid-base interactions are considered. Wu's harmonic-mean (2.27) was used later and has been written below.

$$\gamma_{ij} = \gamma_i + \gamma_j - \frac{4{\gamma_i}^d{\gamma_j}^d}{{\gamma_i}^d + {\gamma_j}^d} - \frac{4{\gamma_i}^p{\gamma_j}^p}{{\gamma_i}^p + {\gamma_j}^p} \tag{2.27}$$

For more information regarding the different models, readers are advised to consult the Drelich et al. review [82] and the Suryiadi et al. article [83]. For further information regarding comparison of wettability methods and applicability, the reader is invited to pursue in the review papers of Bruel

et al. [41] and Aslannezhad et al. [66]. In this project, to evaluate wettability, the sessile drop method was used for flat surfaces and specific methods for meshes and yarns were used, as will be presented in next section.

2.1.3 Specific case of textiles

Measuring wetting on textiles can be quite challenging. First, as shown in models before, air pockets beneath a droplet can affect the wettability properties of a surface. Under the same principle, holes in a mesh can also influence measurement compared to the same material when flat.

When studying the wettability of a mesh, for example for oil-water separation purposes, the sessile-drop method is generally used [84-89]. Nevertheless, it should always be used as a comparative method between similar meshes to ensure consistency of the effect of the holes. Designing a net for agricultural purposes, droplet impact on a mesh or rain tests are more appropriate to study the wettability [37, 90, 91]. A mesh holder [92], as shown in Figure 2.17, can be used to set a specific tilt angle for a rain test. Typically, a syringe pump dispenses water from a specified height for a set duration or volume. The water ingress on the net is then determined by measuring either the mass of the net before and after the test or the volume of unretained water.

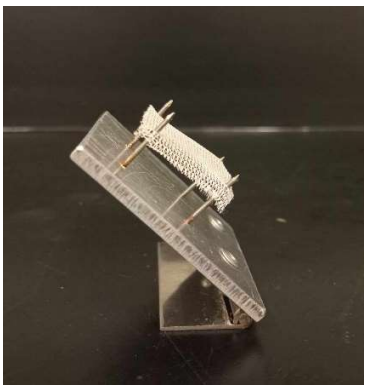

Figure 2.17: Mesh holder used during rain test with a tilt angle of 45°.

In the case of fibers, specific methods have been developed. In the same way as what was presented before, two types of methods exist: the direct measurements of contact angles and force-based methods, all of which can be applied to single or several fibers. Laying a droplet on a single

monofilament yarn or fiber is one of the first methods used (Figure 2.18). This method has been found to be correct for droplets laid symmetrically to the fiber axis (assumption for the mathematical model used), which appears in most cases only for contact angles below 60° [93, 94].

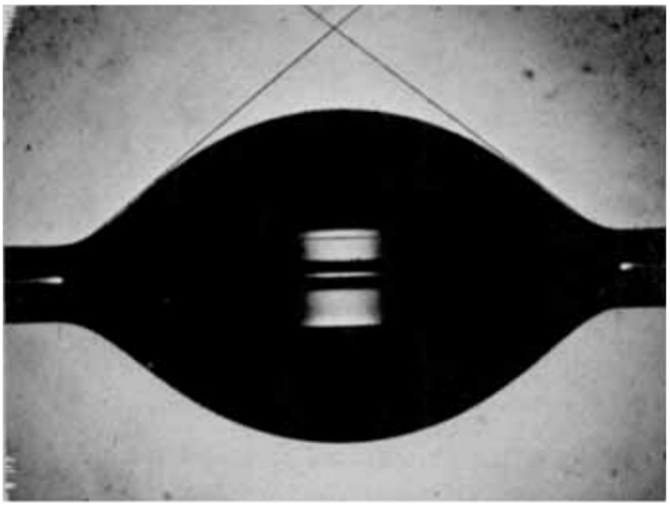

Figure 2.18: Photomicrograph of symmetrical droplet to the fiber axis for single fiber wettability assessment. Extracted with permission from [94]

Measuring wettability using a single fiber has seen more progress with meniscus techniques, where the fiber is slowly submerged in water and similarly to Wilhelmy plate method, the contact angle formed between the liquid meniscus and the sample is studied. In the meniscus technique, the receding contact angle can be measured. Difficulties appear when measuring the advancing contact angle of hydrophobic samples, as the three-phase line will be under the liquid surface [95]. Similarly to the Wilhelmy plate, this technique can be completed with force measurement on the fiber during the wetting and de-wetting cycle. This technique has been called capillarography in its early days [96]. This technique is mostly adapted to thin fibers or rods bigger than 200 μm. This technique, and variations by putting one to four fibers together, have been tested in the literature by Garat et al. [97] as seen in Figure 2.19.

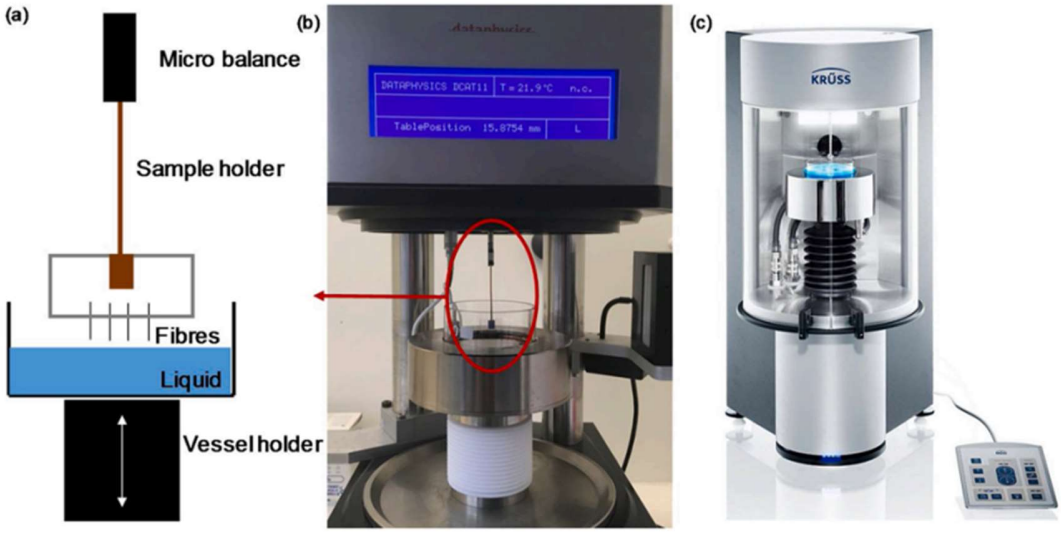

Figure 2.19: (a) Schema of wettability assessment of fibers using force tensiometer (four fibers depicted in schema) with equipment already available such as (b) DCAT11 and (c) K100SF tensiometers. Extracted with permission from [97]

The last method to assess wettability properties of fibers consists in laying a droplet on two parallel fibers [98, 99]. Depending on the contact angle, the spacing ratio and the form of the droplet between the two fibers ("barrel-shaped" or "liquid-bridges wetting") as seen in Figure 2.20, Bedarkar et al. derived relations to correlate wetting length to a theoretical contact angle. The method has been based on finite elements simulations, but more experiments are needed to allow its use to evaluate wettability for specific applications.

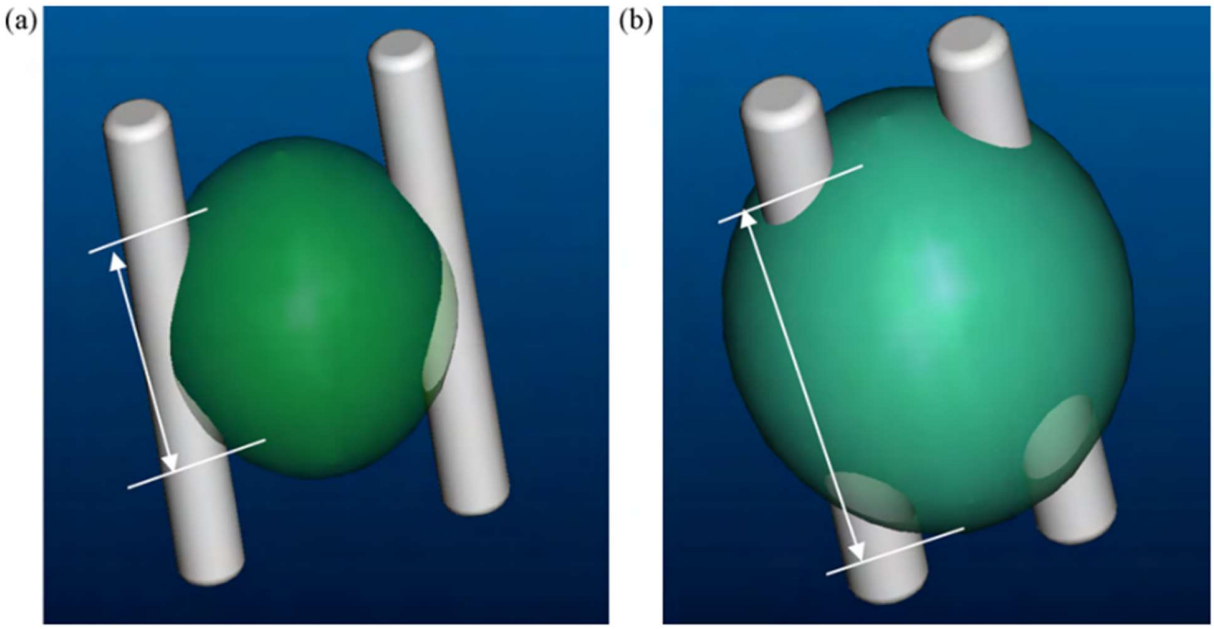

Figure 2.20: Illustrations of droplet forming either (a) a droplet bridge or (b) a barrel-shaped droplet on two parallel fibers. Extracted with permission from [98]

2.2 Surface modification

2.2.1 General introduction to surface modification

To reach specific applications, surface modification has been used to tailor the wettability of a surface. As shown earlier, among a material's intrinsic properties, surface free energy calculated with specific interactions between the two phases forming the interface defines the chemistry contact angle, commonly known as Young's angle. Due to surface heterogeneity and roughness, the apparent contact angle can differ from Young's angle. Tailoring surface roughness allows to define specific surface wettability from liquid spreading to repellency (also called superlyophobicity when referring to solvent wetting). Methods to tailor the roughness and reach superhydrophobicity will be discussed in the following section.

2.2.2 Surface modification to impart hydrophobicity

The natural world provides naturalists and surface scientists with a wide spectrum of wettability behaviors. Early studies of superhydrophobic surfaces concern the duck's feathers observation based on Thomson book "Biology of Birds" published in 1923 [50]. Cassie and Baxter attributed the water repellency of duck feathers to their surface structure. Later, Barthlott and Neinhuis further supported this relationship by demonstrating a correlation between surface morphology and contact angle across various plant species, as illustrated in Figure 2.21.

Inspired by the observations of natural water-repellent surfaces such as lotus leaves, scientists designed morphologies or specific coatings on material surfaces to impart specific wettability properties. As shown earlier, direct modification of the surface by increasing roughness increases the natural wettability behavior: hydrophilic surfaces become more hydrophilic, and hydrophobic surfaces become more hydrophobic. Consequently, chemical composition changes or coatings are necessary to transform hydrophilic surfaces to hydrophobic surfaces. Similar to direct methods, superhydrophobicity can then be reached by increasing roughness.

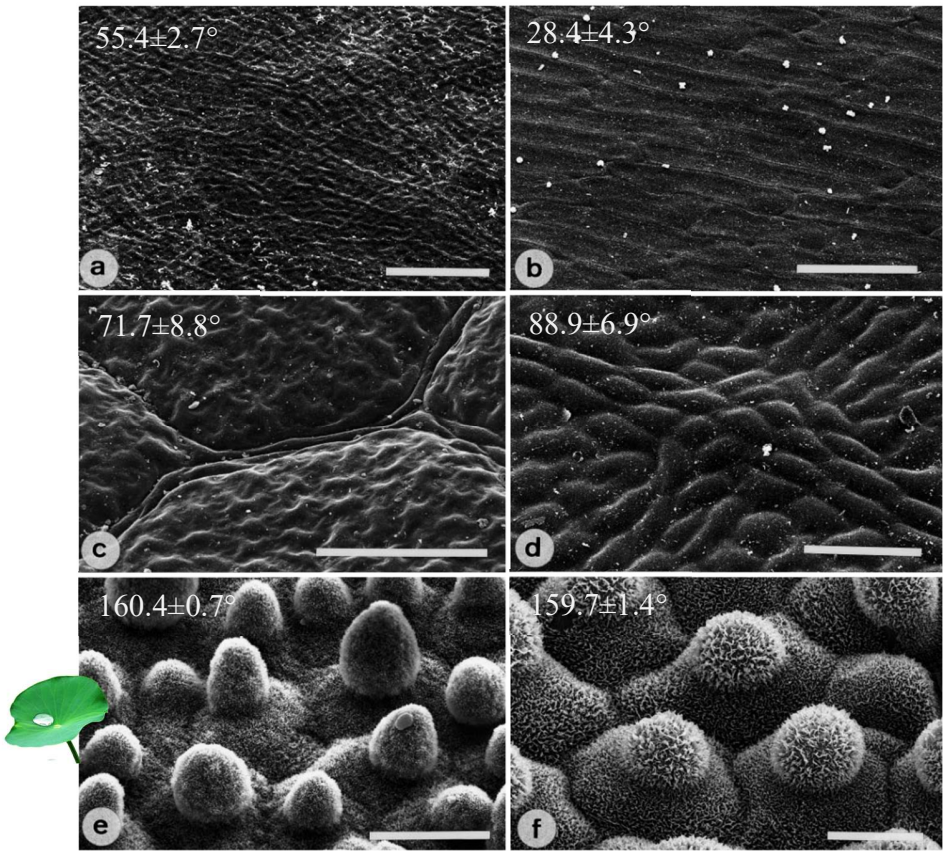

Figure 2.21: SEM images of the adaxial leaf surface of different plant surfaces illustrating water contact angle (top-left corner) as a function of leaf roughness. The plants used are a) Gnetum gnemon, b) Heliconia densiflora, c) Fagus sylvatica, d) Magnolia denudate, e) Nelumbo nucifera (sacred lotus), f) Colocasia esculenta. Bars are 100 µm (a–d) and 20 µm (e–f). Image extracted and adapted with permission from Barthlott and Neinhuis [40].

The limit between hydrophobicity and hydrophilicity was introduced earlier as a water contact angle of 90°. However, in more specific fields such as adsorption studies and surface modification, the threshold for hydrophilic and hydrophobic classification is often refined. Yoon et al. showed the existence of long-range (below 100 nm) attraction forces between hydrophobic surfaces. Using a hydrophobic surface-treated glass sphere attached to the tip of an atomic force microscope (AFM), Yoon et al. [100] probed the attraction forces between the sphere and different wettable silica plates in deionized water. Attraction forces could be measured for silica plates with a water

contact angle down to 75°. Plotting the decay length D_0 of the force measured in Yoon et al. experiment, as a function of the plate water adhesion tension τ_0 verifying (2.28) using $\gamma_0 = 72.8\, dyn/cm$, Vogler showed the existence of two different regimes delimiting an adsorption limit.

$$\tau_0 = \gamma_0 \cos(\theta) \tag{2.28}$$

Similar to DLVO (Derjaguin, Landau, Verwey, and Overbeek) theory, forces are segmented into attractive (hydrophobic) and repulsive (hydration) forces as seen in Figure 2.22. The adhesion threshold also called "Berg limit" [101] is defined as the point below which adhesion forces are no longer detected (interpolation of the linear trend of the long-range attraction forces to a null decay length), which stands for $\tau_0 = 30\, \frac{dyn}{cm}$, meaning a 65° contact angle.

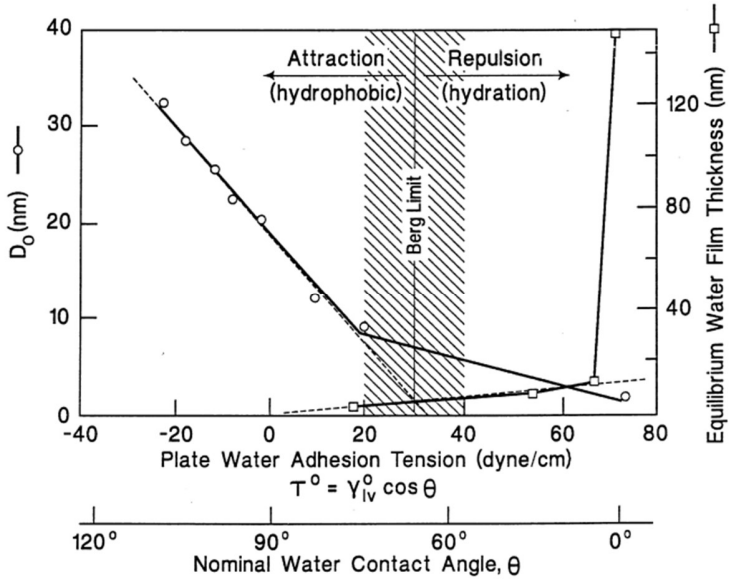

Figure 2.22: Plate water adhesion tension as a function of the decay length to illustrate the Berg limit. Extracted with permission from [102]

This adhesion angle has also been shown in the work of Si et al. [103] where unidirectional transport was only possible if the critical angle was lower than 65° (absence of long-range hydrophobic forces stabilizing the water droplet). As such, to summarize the prerequisite for modifying surface by roughness, there is an intrinsic wetting threshold delimiting hydrophobic and

hydrophilic behavior that is deemed to be at 65°. The higher the Young angle, the more chances to reach superhydrophobicity. As shown in Elzaabalawy and Meguid's simulations [104], contact angles above 150° on rough surfaces were only obtained for Young contact angles greater than 100° for conical pillars, 93° for squared pillars, 96° for cylindrical pillars, and 106° for parabolic pillars. Consequently, superhydrophobicity is subjected to the initial Young contact angle and pillar geometry. Using contact angles between 65° and 90° can result in overhydrophobic surfaces with contact angles near 130° following the Wenzel model, without reaching the Cassie-Baxter state. As such, for insufficiently high Young contact angles or to ensure the maximum contact angle possible (above 160°), coatings with non-polar compounds such as fluorine-based coatings are used on textured surfaces.

Mechanisms to change roughness are numerous and range from techniques allowing full control over the final morphology, such as patterning methods, to other methods with less precise patterns leading to roughness with irregular and amorphous shapes.

Patterning methods:

These techniques allow precise control over the final surface morphology such as designing patterns. For example, Lui et al. [105] used low-speed wire electrical discharge machining to cut horizontal and vertical stripes on a stainless steel 304 surface to form square pillars responsible for superhydrophobicity (water contact angle of ~162.5°), once the surface was coated with a fluorine-based coating. Photolithography is also a common technique found in literature to create precise morphology such as pillars [106]. In photolithography, patterns can be carved using a laser or can be selectively designed using a photoresist layer on top of the material. Positive photoresists become soluble when exposed to light or other stimuli. Selective exposure with goal of removing specific areas or layers of a material is done using a photomask, which acts as a stencil delimiting the zones to dissolve. Removal of the exposed material that has become soluble is done using a solution or a solvent. The same process can be done using a negative photoresist, whose material becomes insoluble after exposure to light or other stimuli. In this case, the unexposed material will be removed during the last step. Lithography has multiple variations depending on the stimuli used to remove the unwanted parts of the surface, such as light, UV, X-rays, electrons, protons, or ions [107]. Depending on the stimuli used, lateral resolutions can be very precise, ranging from 100 nm

down to 10 nm. Alternatively, direct removal can be achieved using heat, mechanical scanning probes, or solvents. Other methods described in the literature include focused ion beam milling techniques and molding-based methods. Molding-based methods are similar to thermal nano-imprint lithography, where a mold is used to shape the material. In these techniques, the material is cast onto the mold, resulting in the material taking on the complementary morphology of the mold [108]. In the case of thermal nano-imprint, a heated mold is pressed into contact with a resin on the material, imprinting the desired pattern and removing the unwanted parts[109].

Patterns can be micropillars but also grooves, lines, microcavities, gratings, etc. These techniques allow to basically 'draw' the surface morphology with a non-negligible cost. Their uses are mainly on metals and ceramics and have been used considerably to understand the role of pillars, their size and geometries (cube, sphere, cylindrical, cone, parabolic, thin peaks, pyramid, wires, etc.), their height and spacing on the surface and how properties might be affected [104, 110, 111]. For example, T-shaped pillars and variations (mushroom-shape, triply re-entrant structures, etc.) have superamphiphobic properties which means superhydrophobicity and superoleophobicity [112].

Techniques with less control over final morphology

In the case of polymers and specifically PLA, several surface engineering methods have been explored, such as PICVD (photo-initiated chemical vapor deposition) [37], inductively coupled plasma with fluorocarbon-based coatings [113], electrospinning [114, 115], and one-step spraying methods of perfluorinated-silane multi-walled carbon nanotubes PLA solutions on textiles [116], which were successfully used to impart hydrophobic surface properties. These techniques tend to hold less precision on the final morphology and its uniformity compared to patterned methods. Different types of PLA morphology using different preparation methods to obtain porous material are seen in Figure 2.23.a). Among the four methods, phase separation methods are a vast category of methods to tune PLA properties.

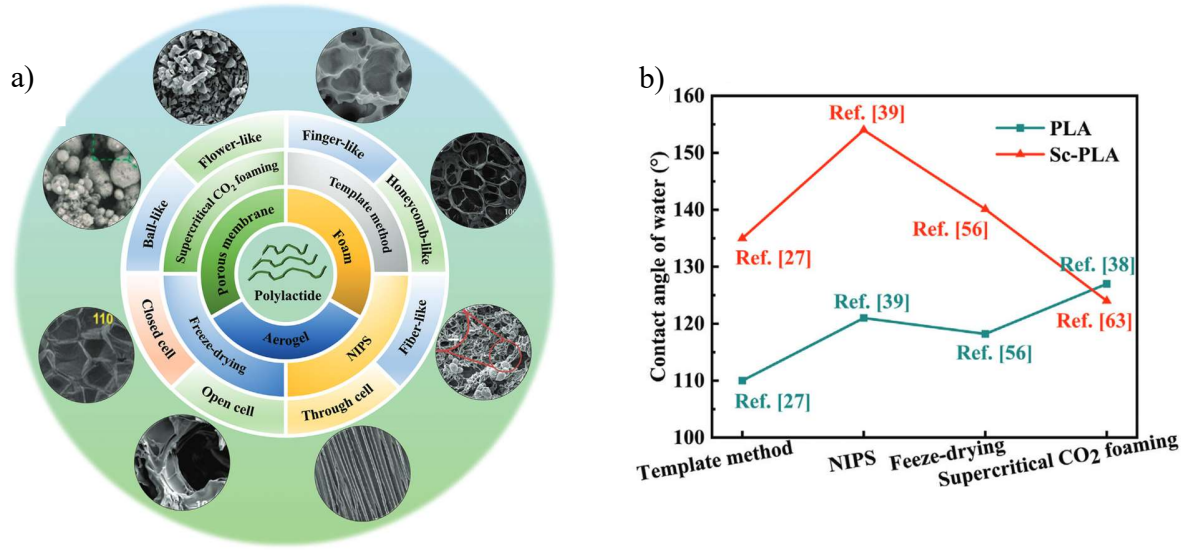

Figure 2.23: a) Image of PLA morphology depending on initial material state and preparation method. b) Water contact angle obtained for the different methods in some publications. Figures extracted with permission from Hou et al. review [117]

As can be seen in Figure 2.23.b), in some cases using these different methods the contact angle obtained seems to hardly reach 130° for PLA. Phase separation and freeze-drying methods can take time, are costly, and might be more suited for biomedical applications than for agricultural purposes where large-scale fabrication is required. Similarly, the previous methods mentioned either face some upscaling difficulties or are using fluorinated and/or silane compounds that are noxious for the environment, which is not the goal if a viable alternative to pesticides is sought.

Solvent-induced recrystallization process

Our research team developed a simple two-step solvent-induced recrystallization protocol, called dip-dip-dry (DDD), to modify the wettability of lab-scale and commercially available PLA for outdoor applications [118], imparting over- or superhydrophobicity. Amorphous PLA discs are dipped over 10 min in a solvent such as acetone to slightly dissolve the polymer and drive texturation. Mobile chains remaining on the surface will shrivel when dipped in a coagulant bath (such as deionized water) for an additional 10 min. During this phase, recrystallization occurs as the chains contract due to water acting as a nonsolvent for PLA. This causes formation of a water-

repellent microstructured surface. The DDD-treated samples are then dried for 48 h under vacuum. Knoch et al. showed the morphology obtained with this technique to be dependent on the initial crystallinity of the material and its shaping history. When repeating treatment on a crystalline mesh, acetone would leave crazes instead of flower-like structures on the surface, as seen in Figure 2.24. Crystallinity reduces swelling, which is the phenomenon responsible for freeing some chains at the surface of PLA. As such, crystallinity reduces solvent action in the DDD protocol. The solvent is deemed to have more effects on the amorphous zones. The final drawing stage in the production of the fibers orients the crystals in the direction of the fiber's axis, which would also imply an orientation of the amorphous zone. As such, propagation of the solvent into the material is deemed to follow the path of easy-swelling zones, which are aligned with the fiber's direction. Consequently, crazes observed when using DDD on a crystalline mesh align with the direction of the fibers. Heating the acetone increases the number of crazes and decreases the final mechanical properties of the treated part [92].

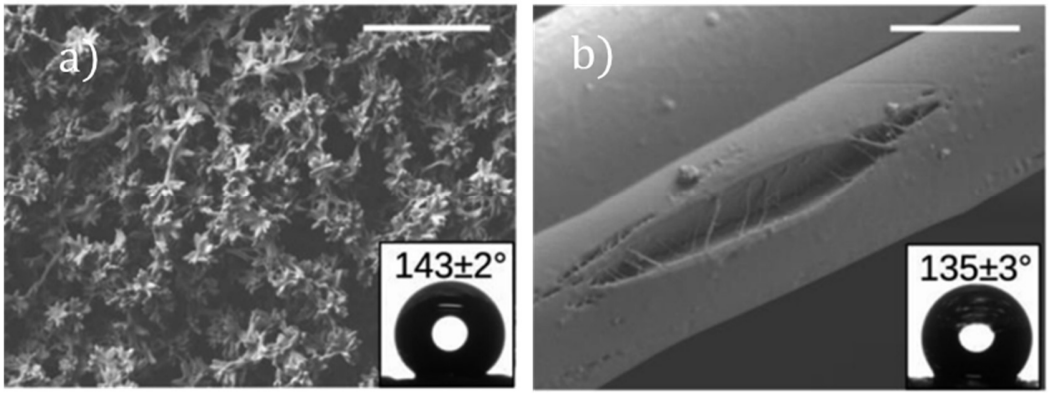

Figure 2.24: SEM images of DDD-treated a) amorphous PLA 3D-printed net (flower-like morphology) and b) crystalline PLA net commercially available (crazes). Extracted from Knoch et al. [37] under license CC BY-NC-ND 4.0Treatments on amorphous discs and meshes have consistently shown a flower-like morphology, whereas applying the same treatment to crystalline PLA materials presents challenges. Karthikeyan et al. conducted follow-up work on commercially available PLA nets, revealing that adding a preheating step immediately before the DDD treatment enhances chain mobility near the surface, promoting swelling and the formation of a textured surface. To avoid dissolution or degradation associated with heated

acetone, a non-solvent for PLA was selected for the preheating bath. Ethylene glycol (EG) was chosen due to its lack of affinity with PLA and its high boiling point (195-198 °C). However, as a non-solvent, EG encourages PLA chains to minimize contact by contracting, ultimately forming a sphere to reduce interfacial tension, particularly at higher temperatures as seen in Figure 2.25 showing the visual aspect of the treated nets under different preheating temperatures.

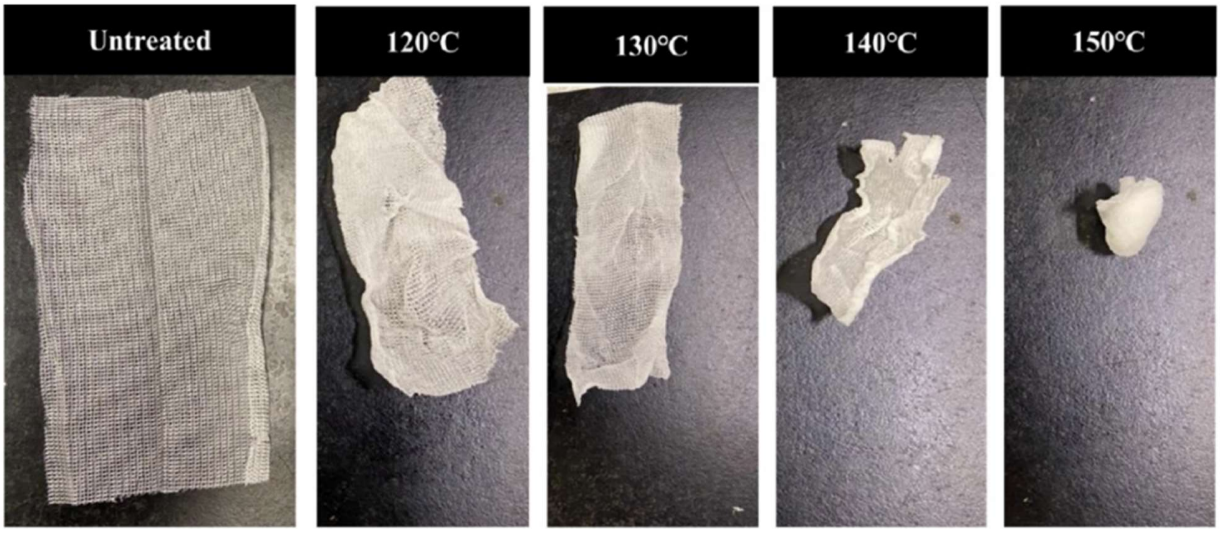

Figure 2.25: Image of nets before and after DDD treatment with a EG preheating step at different temperatures. Reprinted with permission from Karthikeyan, A., et al., Surface Modification of Commercially Available PLA Polymer Mesh. Industrial & Engineering Chemistry Research, 2022. 61(47): p. 17297-17305. Copyright 2022 American Chemical Society. [92]

This study identified a critical preheating temperature necessary for effective treatment. For example, with the multifilament PLA commercial grade Filbio® from MDB Texinov®, no surface modification was observed at temperatures below 120 °C. Between 120 and 130 °C, the treatment produced non-homogeneous and subtle surface textures on the nets. Above 130 °C, more uniform surface texture emerged due to enhanced chain mobility and solvent action. The shrinkage of the nets serves as an indicator of polymer chain mobility and potential recrystallization.

This initial work by Karthikeyan et al. serves as a first demonstration of transposing the DDD protocol onto commercially available substrates, showing that treated meshes develop a

recrystallized-textured surface with hydrophobic properties and enhanced mechanical performance. However, several key questions remain unanswered:

- **Defining the Critical Temperature:**
    - This critical temperature lies above the glass transition temperature of PLA (~60 °C) and cold crystallization temperature (~110 °C) but well below the melting point (160-180 °C, varying with PLA grade, molecular weight, and crystal type). This study focuses on PLA with low D-isomer content (<2%), mainly encountering α and α' crystals.
- **Effect of Restricting Chain Mobility:**
    - What happens when chain mobility is restricted by forces such as tension on the fibers? Would the thermal pretreatment still be sufficient for surface texturing, or would the critical temperature need to be increased?
- **Relationship between Temperature, Shrinkage, and Treatment:**
    - Increasing temperature induces shrinkage and enhances chain mobility, which allows the treatment to take effect. However, the critical temperature for this effect needs clearer definition in the context of chain mobility and recrystallization.
- **Impact of Shrinkage on Mechanical Properties:**
    - Does shrinkage enhance the mechanical properties of individual fibers or merely increase the number of yarns per width which will result in higher mechanical properties when studying nets based on specific width as per ISO 13934-1:2013 standards?
    - How do mechanical properties change due to shrinkage and reorientation of polymer chains?
- **Balancing Shrinkage and Surface Modification:**
    - How can shrinkage be limited to achieve surface modification and desired wettability without excessive material loss?

- Is the additional material from shrinkage necessary for forming surface microstructures alongside chain mobility?

2.2.3 Surface treatment and chain mobility

As an initial exploration of the relationship between polymer chain states and surface treatment, some insights into the questions raised in the previous section can be found in existing literature. Studies have investigated the effects of various parameters, such as tension and drawing ratios in roll-to-roll systems, on surface treatment across different fields. These findings provide a foundational understanding of how chain mobility and processing conditions influence the effectiveness of treatments, guiding the adaptation of these techniques for industrial applications.

Tension

Numerous parallels can be drawn between DDD treatment and mercerization, an alkaline process using sodium hydroxide (NaOH) to remove hemicellulose, lignin, and impurities from natural fibers. This treatment increases the cellulose content, enhancing the strength and stiffness of the fibers. Like DDD, alkali treatment induces biopolymer chain swelling by diffusing into the polymer structure and breaking hydroxyl groups, which increases chain mobility and allows for structural rearrangement. However, mercerization differs from DDD in several key aspects: when NaOH contacts cellulose, it penetrates intracrystalline spaces and breaks some crystals through depolymerization reactions [119, 120]. This leads to a crystallinity drop and consequently an increase in the percentage of amorphous zones [121]. In contrast, DDD treatment does not attack crystalline structures; swelling occurs in the amorphous zones, and after washing and drying, surface recrystallization occurs. During mercerization, washing also significantly impacts the fibers, producing a new cellulose structure that alters the surface morphology [122].

Shrinkage is a notable effect observed in both treatments. For mercerization, shrinkage is driven by a chemical mechanism [123]. During mercerization, hydroxyl groups are replaced by sodium-cellulose complex during treatment. These complexes are removed during washing, which leads to lower osmotic pressure and subsequently fiber shrinkage. In the case of DDD treatment, longitudinal shrinkage occurs primarily due to temperature effects, leading to radial expansion of

the fibers. This suggests a potential change in osmotic pressure as the solvent dissolves surface PLA chains.

Goda et al. found that applying tension could enhance the mechanical properties of mercerized ramie fibers when a washing step with a water-acetic acid solution was performed immediately after treatment. This step removes residual sodium hydroxide, preventing further degradation. Swelling induced by surface treatment can alter the orientation of fiber chains, reducing tensile strength if no tension is applied, as unidirectional chains exhibit greater strength when aligned with the load direction compared to unoriented fibers. Similarly, in DDD-treated fibers, preheating previously stretched fibers may cause misalignment and negatively impact mechanical properties. Swelling and reorientation increase the yarn diameter compared to fibers treated under tension. Depending on treatment duration and washing conditions, mercerized fibers can become even larger than untreated fibers, with tensile strength reductions ranging from 30% to 80%.

However, DDD treatment promotes surface recrystallization, which may positively influence mechanical properties. Studying the mechanical behavior of DDD-treated monofilament yarns will clarify the predominant effects of presence of tension or not. This is supported by Goda et al., who found that applying appropriate tension during treatment improved tensile strength and could double or triple fracture strain compared to untreated fibers and led to a 4% increase compared to fibers treated without tension. However, excessive tension reduced yarn diameter and could negatively affect mechanical properties if over-applied.

Similar findings were reported by Kim and Netravali [124], who conducted mercerization on sisal fibers. In their study, tension was applied using a suspended weight attached to the end of the yarn, as illustrated in Figure 2.26. The effectiveness of tension in enhancing fracture stress and Young's modulus showed a threshold at 50 g per fiber; beyond this point, further increases in load led to a decline in mechanical properties. Treating loose yarn samples (called "under slack condition") produced intermediate values for mechanical properties such as fracture stress and strain, Young's modulus, and toughness. After treatment, fracture strain and toughness decreased compared to untreated samples, but the reduction was less pronounced when treatment was performed under slack. These findings were consistent when testing the composite materials made with the various fibers (untreated, treated under slack, and treated under tension).

These conclusions for treatment under tension are consistent with Sharma et al. observation of mercerization on flax fibers under tension [123]. They noted that tension reduced swelling, with the fiber diameter remaining relatively unchanged, and surface texturing was minimal. In contrast, when treated under slack, swelling was more pronounced, leading to more defined ridges and grooves. Thus, treatment under tension inhibits swelling and crimping, reducing surface modification. Roughness directly influences the wettability properties. Consequently, the key insight from this study is the potential existence of a tension threshold that ensures sufficient swelling and, subsequently, adequate surface texturing required to achieve superhydrophobic properties.

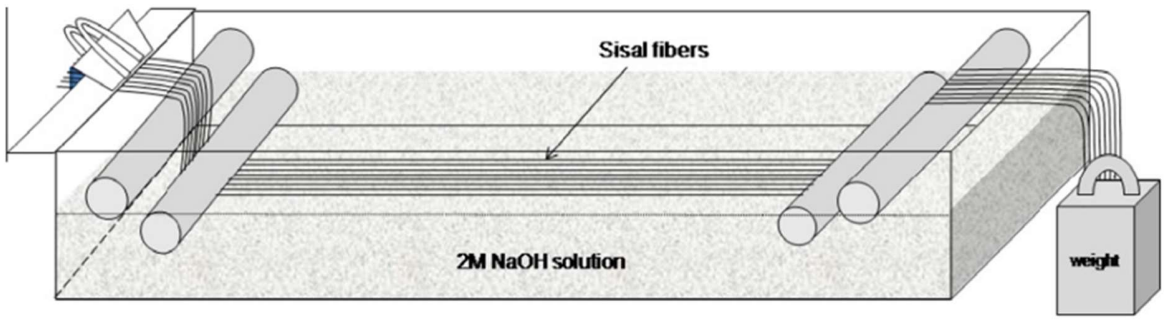

Figure 2.26: Set-up used by Kim and Netravali to fix yarn tension during treatment. Image extracted with permission from [124]

Overall, mercerization is strongly dependent on treatment parameters such as temperature, concentration of the chemical agent, and time of treatment [122]. As shown by Karthikeyan et al., and discussed later in the present work, this is to some extent also true for DDD. It is also very important to keep in mind that mercerization occurs by removing matter whereas surface modification by DDD occurs by rearranging remaining polymer chains at the surface. As such, specific tension effects might differ, but from this study it seems relevant to research the different ways to measure tension.

Measuring tension and slack:

At first sight, tension seems to be easily measurable. Numerous tension measuring devices are commercially available. They are generally based on deflecting the course of the yarn by making

it pass on pulleys linked to force sensors or other sensitive instruments. Several configurations are identified by Brunnschweiler and Parikh [125]. Depending on tension, the yarn will provide a natural push force to resist again deflection. This force is deemed as a representative measurement of yarn tension. Nevertheless, it is well known that this assumption is based on neglecting the increase in tension coming from the deflection of the yarn. As this is the predominantly used method to measure tension, it would be more precise to say that yarn tension measurement includes this slight perturbation in the tension range during quality control. Other more sophisticated methods involve sending pressurized air on the yarn to induce vibrations and measure oscillation frequency using an IR photodetector. The amplitude and frequency of the oscillations can be correlated to yarn tension. Apparatuses based on waves analysis are called non-contact tension meters [126, 127]. This introduction to tension in the textile industry gives a pretty good idea of what can be used to upscale the DDD treatment and formulate industrial guidelines. As supplementary information, it should be kept in mind that tension will depend on the different point of friction between yarn and rolling elements, which will also depend on their speed. In this case also, some systems have been developed to measure dynamically friction coefficient [128]. Dynamic measurements are particularly sought for industrialization, as automated roll-to-roll processes represent the main technique to upscale textile processes.

Roll-to-roll processes:

In roll-to-roll processes, a complete spool unwinds a yarn, which will be pulled from a winding spool to run the yarn through different baths, or heating and cooling devices, depending on the desired treatment. Some studies based on roll-to-roll processes have also highlighted the role of tension in continuous operation [129]. These will be studied in more detail in Chapter 5.

2.3 PLA, wettability and degradability

2.3.1 Polylactic acid (PLA)

There are numerous reasons for the choice of PLA among biopolymers. It is formally a polymer derived from renewable resources, and for simplicity, the term biopolymer will be used in the text. PLA tends to have among the highest mechanical properties of biobased compostable polymers.

This is particularly seen in the widespread use of PLA as a matrix in biocomposites like PLA/flax, where its usage and research have increased since the pioneering work of Oksman et al. in 2003. [130] This work showcased PLA/flax composite having similar to 66% better Young modulus and about 50% better in maximum stress than polypropylene PP/flax composite. Sadasivuni et al. [131] reviewed different advances in mechanical properties for multiple biopolymers. PLA composites displayed the highest elongation at break and very high tensile modulus compared to other reinforced biopolymers. Mechanical properties are necessary to ensure nets do not break from slight deformation during laying and fixing process on the tree for example. Finally, to address issue of cost, it is deemed that PLA is 10 times less expensive than its major, PHA (polyhydroxyalkanoate) [132]. PLA is already one of the least expensive options for biobased compostable polymer and this comes from the way it is produced. PLA is derived from the polymerization of lactic acid (LA) monomers, which can be either chemically synthetized from petroleum-sources by lactonitrile hydrolysis or can be produced from microbial fermentation. The latter method accounts for 90% of the world LA production. This technique is the leading choice in industrial applications because of its low energy consumption and reliance on renewable resources. Lactic acid can be produced via different types of fermentation: homo or hetero fermentation with each category having subcategories characterized by different chemical reactions leading to production of different byproducts. For more information on which bacteria is associated with which fermentation, the reader is kindly directed to the very visual and thorough review of Swetha et al. [133]. From the monomers, several polymerization routes exist to produce PLA from lactic acid. Three to four polymerization types can be identified: azeotropic dehydration, ring opening polymerization (ROP), polycondensation and finally enzymatic polymerization which is a combination of the two previous ones [133-135]. Each method is appropriated to produce PLA of different molecular weight. PLA obtained with polycondensation hardly reaches 5000 g/mol but is the less expensive. Using ROP and azeotropic dehydration, molecular weights up to 100 000 and 300 000 g/mol can be reached, respectively. Depending on the final mechanical properties and price desired, different processes will be used. A schema of the polymerization mechanisms and the PLA chemical structure are given in Figure 2.27.

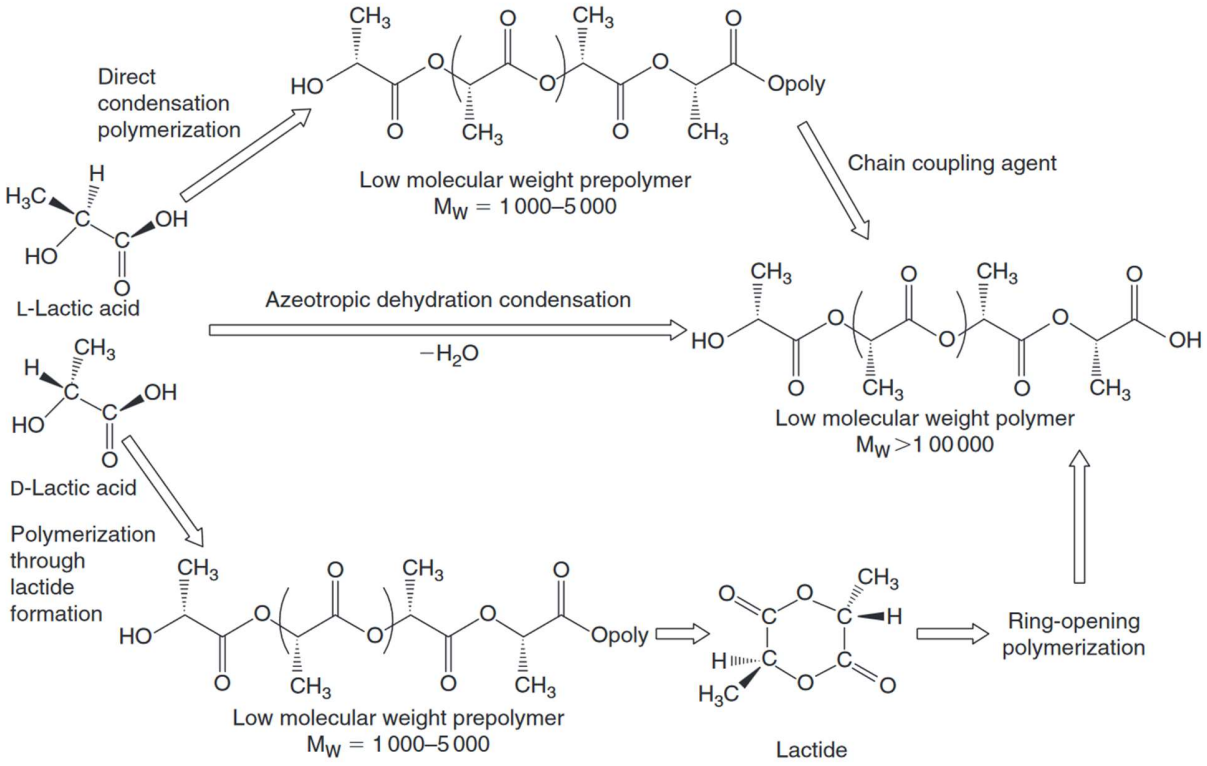

Figure 2.27: Schema of PLA polymerization mechanisms. Extracted with permission from L. Avérous [136]

2.3.2 PLA end-of-life

As shown earlier, depending on the polymerization technique used, PLA can exhibit a wide range of molecular weights, which directly affect its properties. Higher molecular weights result in longer polymer chains with more entanglements, contributing to improved mechanical strength. The thermal properties are also influenced, as longer chains generate stronger intermolecular forces. More energy will be needed to break the additional intermolecular forces and give mobility to the chains, resulting in increased glass transition and melting temperatures as molecular weight rises [137].

From large spectrum of properties achievable with PLA, numerous field of application can be reached such as packaging, agriculture, textile, electronic ware, transportation, and other fields such as biomedical fields, where PLA biocompatibility makes it a well-suited candidate [138]. In

Ranakoti et al. review [139], agriculture is deemed to be the second most important application, accounting for 16% of PLA applications just after the packaging industry taking 49% share of the PLA industry. Trends to use biobased compostable materials are pushing these bioplastics to be used more frequently. In the same review, it was forecasted that PLA market would more than double in the period 2022 – 2030 to reach 2.5 billion US dollars. Nevertheless, several researchers have shown that this transition needs further prevision in regard of predicting the end-of-life of this increasing amount of compostable materials, who have a non-negligible environmental impact. For example, under the hypothesis of full carbon sequestration (process of capturing and storing carbon dioxide) for HDPE, LDPE (low density polyethylene) and Bio-PE, Benavides et al. [140] found that the greenhouse gases (GHG) emissions of partly biodegradable PLA will be greater than biosourced or petroleum-based PE (Figure 2.28). PLA biodegradation rate and percentage depends on numerous parameters such as molecular weight, crystallinity, thermal behavior and by environmental factors such as humidity, temperature, and microorganism species present. To calculate emissions, Benavides et al. compared scenario where PLA would be not biodegradable (0%) or partly biodegradable (60%). Emissions are significantly more important in the case of partly biodegradable that ends-up landfilled due to favorizing methane CH_4 formation during anaerobic decomposition (landfill conditions) instead of increasing CO_2 release during aerobic decomposition (composting conditions). Methane can be used as a biogas if production and storage is well-controlled such as in biomethanation end-of-life. Nevertheless, in landfills, uncontrolled methane release in the atmosphere has a disastrous impact because its global warming power is 25 times greater than carbon dioxide. In the case of composting, less than 5% of the degraded carbon is deemed to transform into methane whereas in the case of landfill this figure is deemed to go up to 58% [140]. Designing the end-of-life of PLA waste is then very important, taking into account the projected increase in production and waste in the coming years.

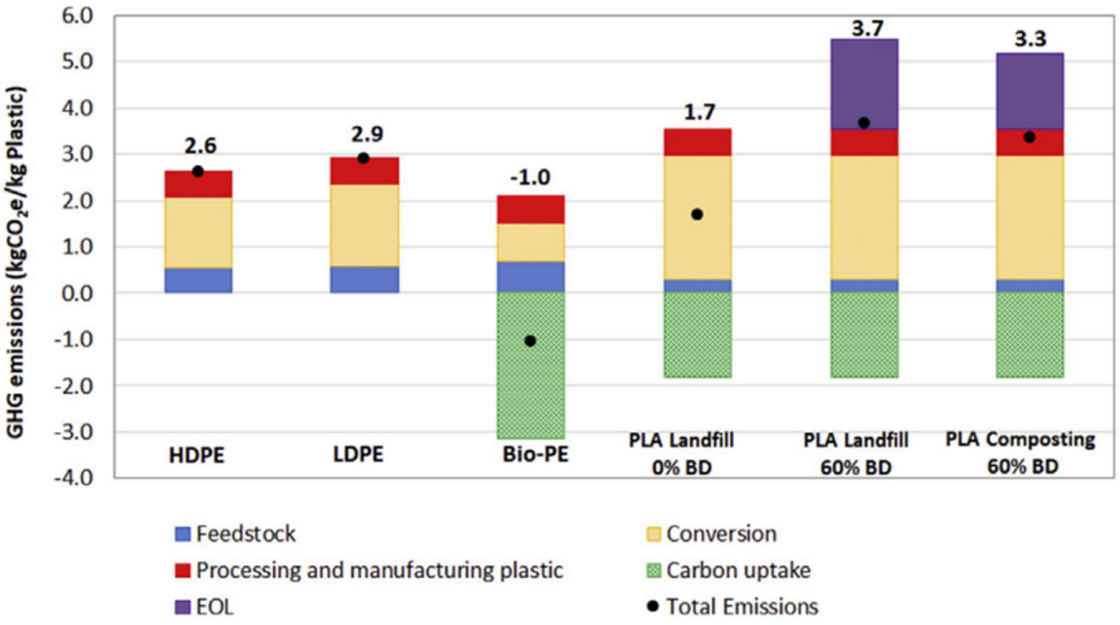

Figure 2.28: GHG emissions throughout life cycle of HDPE, LDPE, bio-PE and PLA, including different EOL scenarios for PLA. Extracted with permission from [140]

PLA end-of-life possibilities are numerous: mechanical recycling, chemical recycling, industrial composting, methanation, thermal valorization including direct fuel substitution and incineration, and landfill. In the book chapter from Bher et al [141], these options are compared according to global warming score. As seen in Figure 2.29, industrial composting seems to be a choice to avoid in regard to global warming score. Nevertheless, as shown earlier, depending on the hypothesis and environmental impact studied, the conclusion changes. The most commonly done end-of-life are mechanical recycling, industrial composting and landfill. Mechanical recycling implies collecting PLA at end-of-life and a sorting system to be in place, which is only viable for large quantities of plastics such as polyethylene or polypropylene. In regard to other indicators and public opinion, landfill seems to be the last resort but should not be the default option. Progress in making PLA a low-carbon materials has already been researched. According to Morão and de Bie [142], improving the raw materials source and the production process could reduce by 909 $kgCO_2eq$/ton PLA the carbon dioxide emissions related to the use of PLA. Ranakoti et al. have

also highlighted that the conversion of PLA would need to be optimized to make PLA a low carbon material.

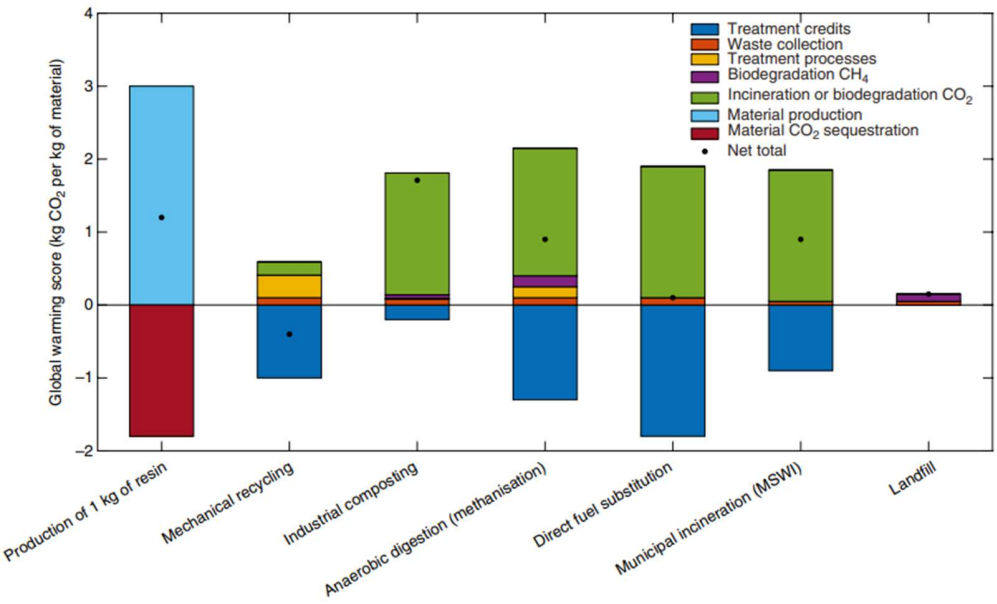

Figure 2.29: PLA environmental impact depending on various end-of-life. Extracted with permission from [141]

Towards the general inclination to compostability and a cradle-to-cradle approach, completed by ways to reduce drastically PLA environmental impact, this study aimed to develop processes so that compostability of the material is still valid after hydrophobic treatment which might indirectly alter degradation mechanisms as microbial attachment reduces on superhydrophobic surfaces [38]. The link between hydrophobicity and degradability will be explained in more detail in Chapter 4. As a summary, inducing degradation or imparting factors such as hydrophilicity with a surface treatment can result in facilitating biomethanation or compostability. This represents a viable way to deal with hydrophobic PLA products.

2.3.3 Surface modification to impart hydrophilicity

Mechanisms of degradation of a polymer are well-known and are closely related to conditions of a material failure such as chemical attack, thermal degradation, mechanical failure (stress cracking,

crazing, rupture, dynamic fatigue, etc.) or environmental specific conditions such as radiations. Yasin et al. [143] wrote a review explaining how these chemical and physical mechanisms can be used to enhance the degradation of plastic using a pretreatment. Chemical pretreatments are based on exposure to alkaline solutions to enhance hydrolysis happening at the first stages of biomethanation process. Decomposing more matter will eventually allow higher yields of methane to be used as biogas at the end of the process. Acid solutions can also be used to stabilize a neutral pH, which is deemed to be ideal for biomethanation. Nevertheless, compared to PHB and in general, PLA is not considered as an acceptable input for biomethanation sites [144, 145]. Physical treatments can be separated into thermal and non-thermal processes. Thermal processes will enhance the rate of biodegradation by reducing polymer molecular weight by chain scission. A drop in molecular weight also leads to a decrease in material properties, such as tensile strength.

Physical non-thermal methods regroup more categories such as mechanical pretreatments and advanced oxidation processes (AOP) such as plasma, ultrasounds, UV or more generally exposure to radiation. Mechanical pretreatment is defined by the application of a force on the material to increase surface area by reducing size of the polymer fragments, which is basically grinding. Size reduction alongside rotary screens for separating grinded materials based on size and fraction of liquid is already a step done in sorting facilities. AOP has a less advanced technology readiness level (TRL), but extensive research is being conducted to diversify their uses. In the work of Kalogirou et al. [146] comparing plasma, UVA and ultrasounds, plasma showcased better performance in increasing PLA surface hydrophilicity. In less than 5s, a 20° drop in contact angle can be noticed. Nevertheless, increasing the treatment time to 60 seconds did not vary the contact angle. Inversely, in Ren et al. article [147], dielectric barrier discharge (DBD) was also used and the longer the treatment time, the greater the surface roughness and the better the hydrophilicity until reaching a water spreading surface after 90s of plasma treatment. Discharge settings were different between the two articles, especially the frequency applied to the electrode. Among AOP, exposure to UVC has also been shown to increase wettability while taking a significant amount of time as can be seen in Hyun Jeong Jeon et al. article [148] where a 24h exposure translated in a 10.6° decrease in contact angle. Time consumption is deemed in Yasin et al. review [143] as one if not the major barrier to UVC pretreatment upscaling. A part of this work will then be dedicated

to test and finding efficient pretreatment for enhancing degradation and/or switching back the DDD-treated PLA nets to hydrophilic.

The impact of UV exposure on PLA will be discussed in more detail in Chapter IV. This MSc work introduces new information regarding wettability switch from hydrophobic to hydrophilic on a textured surface using UVC exposure (Chapter IV). Once viability is confirmed, guidelines on upscaling to industrial modification will be addressed. This report seems to be the first to introduce chain mobility quantification from a viewpoint of additional matter (slack) rather than tension, and its effect on desired surface properties such as wettability and mechanical properties (Chapter V).

CHAPTER 3 OBJECTIVES, METHODOLOGY AND GENERAL STRUCTURE

3.1 Specific objectives (SO)

This work will focus on exploring the relationships between chain mobility, additional length, and treatment by examining shrinkage as a function of slack and temperature. Understanding these parameters is essential for determining how the DDD treatment can be industrialized or automated. Additionally, adapting the DDD treatment to practical applications is critical. Exclusion nets are specifically designed with mesh sizes that allow or block certain insects based on their dimensions, while still permitting sufficient sunlight to reach the plants. However, the preheating step in the treatment causes shrinkage, altering the mesh size – a change that is undesirable. Therefore, a key aspect of this research involved developing and evaluating methods to impart quasi-superhydrophobicity to PLA nets while maintaining the original mesh size. This approach aligns with the overall goal of designing industrially producible, hydrophobic, biobased exclusion nets for sustainable agriculture and finding ways to revert their wettability at the end of life to facilitate compostability. Logically derived, the specific objectives of this work are:

- **SO1. To revert the wettability of DDD-treated materials using UV radiation, ensuring that the material retains its compostability similar to its initial state.** This objective primarily validates the surface treatment for sustainable product design, taking into account the entire life cycle of the material (cradle-to-grave or cradle-to-cradle approach).
- **SO2. To replicate batch-processed DDD treatments through an industrially scalable technique, with a focus on developing an automated process suited for the exclusion nets industry requirements and large-scale products.** This objective ensures that the research is adaptable for industrial application, facilitating a seamless transition into the industry.

These specific objectives collectively aim to support the commercialization of biobased hydrophobic exclusion nets that are compostable under appropriate conditions, advancing sustainable practices in agriculture.

3.2 Thesis structure

Thesis structure is presented in Figure 3.1.

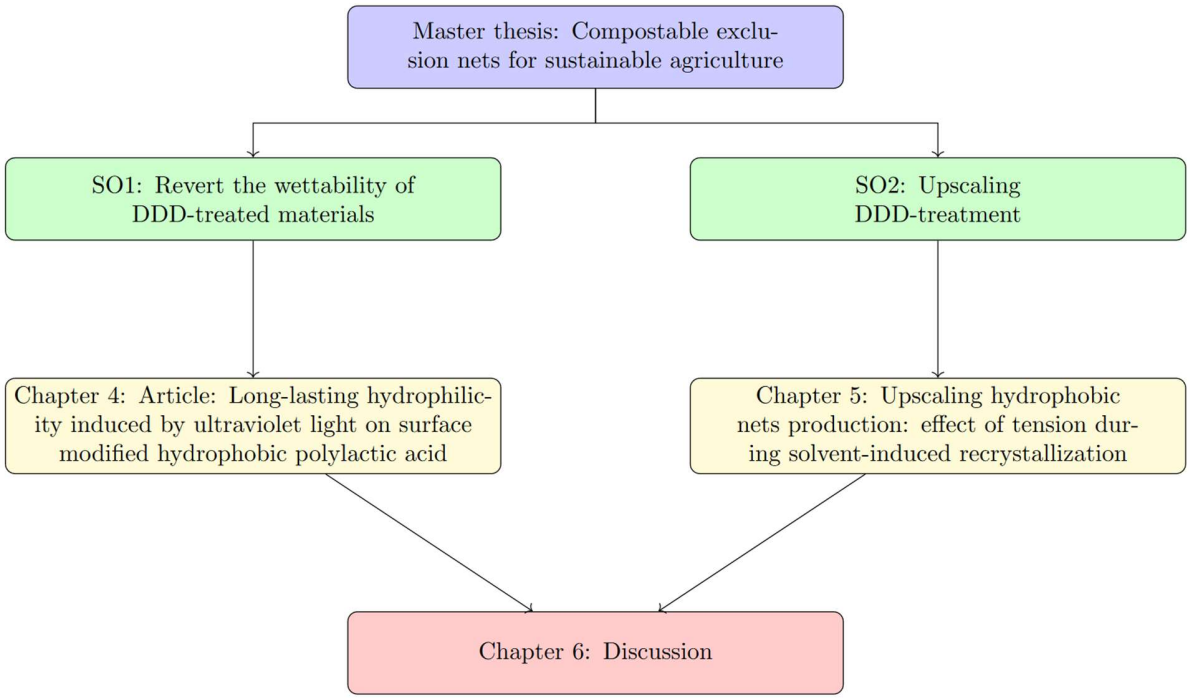

Figure 3.1: Overview of the research conducted and structure of the thesis

CHAPTER 4 ARTICLE 1 : LONG-LASTING HYDROPHILICITY INDUCED BY ULTRAVIOLET LIGHT ON SURFACE MODIFIED HYDROPHOBIC POLYLACTIC ACID

William Simon[a], Darius Klassen[a], Marie Mottoul[b], Simon Ponton[a], David Brassard[a], Adya Karthikeyan[c], Marie-Josée Dumont[b], Jason Robert Tavares[a]

[a]CREPEC, Department of Chemical Engineering, Polytechnique Montréal, Montréal, Canada,

[b]CREPEC, Department of Chemical Engineering, Université Laval, Québec, Canada,

[c]Department of Chemical and Biological Engineering, University of Ottawa, Ontario, Canada

Submitted to Journal of Applied Polymer Science, 23/10/2024.

4.1 Abstract

Surface treatments are used to tailor the wettability of compostable or biodegradable polymers, to suit specific applications such as outdoor products. However, imparting hydrophobicity can have direct and indirect consequences on the polymer's degradation. In this research a solvent-treated hydrophobic (water contact angle of 147.2 ± 0.6°) polylactic acid (PLA) substrate could be altered significantly to a wicking sample after water contact angle stabilize shortly at 22.5 ± 3.1° with a single 2-hour ultraviolet-C (UVC) exposure from a low-pressure Hg discharge lamp. Wicking behavior remains consistent even one year post-exposure implying permanent change to the polymer surface. UVC irradiation induced chain scission near the surface, reducing considerably M_n and M_w, respectively, the number and weight average molecular weight. For pressed PLA, M_w could go down to $6.06 * 10^4\ g.mol^{-1}$ for the first 20 µm of the UV-exposed solvent-treated surface, starting with pellets having molecular weight of $1.4 * 10^5\ g.mol^{-1}$. Reduction in molecular weight impacts properties, including lower glass transition, melting and degradation temperatures. No chemical change could be detected with X-rays Photoelectron Spectroscopy and no change in crystallinity or morphology was identified. The increased presence of polar bonds on the surface after UV-exposure may be the result of chain scission or simply orientation of polar oxygen bonds towards the surface are responsible for the wettability change.

Keywords: PLA, Surface modification, UVC exposure, Chain scission, Degradability

4.2 Introduction

As of 2022, the world's plastic production had grown to over 400 million metric tons annually, and forecasts suggest that this number could soar to nearly 1 billion metric tons by 2050 [149, 150]. Currently, waste management systems do not have the capacity to handle this quantity of plastic wastes and the ever increasing fraction of mixed polymer products, which results in the landfilling or ocean-dumping of massive quantities of plastic wastes [151, 152]. Since the most-used plastics are not biodegradable, they accumulate in the environment, not only in the form of visible products such as macroplastics but also as microplastics. These tiny particles have been found everywhere, from alpine glaciers [153] to the invertebrates of Antarctica [154], posing significant threats to both fauna and flora [155-157]. To help address this ever-growing issue, biodegradable and compostable materials have been under intensive and increasing research over the last 20 years (Supplementary Material Section 1). The idea of using biopolymers or bioplastics is not new. As a matter of fact, bio-based plastics were known well before petroleum-based plastics were discovered [158], but their cost of production was too high when compared to other options at industrial scale. Now that mass production technologies are well-developed and plastic pollution has become a major concern due to accumulation of plastic in the environment, compostable materials are gaining renewed interest as a potential solution to manage residual waste, in parallel with reduction efforts.

Among the conditions required for a plastic to be classified as compostable according to ASTM Standards D6400-21, at least 90% of the remaining polymeric material should reach a size smaller than 2.0 mm after 12 weeks of composting [159]. Compostable plastic bags and straws are examples of ASTM certified products. Polylactic acid (PLA) is a bio-based and, under appropriate conditions, bio-degradable polymer that can meet this requirement. It is a polymer derived from renewable resources, the term bioplastic will subsequently be used in the text to describe synthetic polymers that are biobased and/or biodegradable. Drumright et al. have demonstrated the complete degradation of PLA in a 60 °C composting environment over a span of 40 days [160]. Concurrently, Karamanlioglu et al.'s review [36] confirms that PLA degradation in composting conditions at 50-60 °C typically took 45 to 60 days. These same researchers specified however that the rate of PLA decomposition in compost depends on the PLA product geometry: 30 days for bottles, 20 days for

sheets, and 40 days for fabrics. This can be explained by the fact that degradation is influenced by material parameters such as molecular weight, crystallinity, thermal behavior, surface/volume ratio and by environmental factors such as humidity, temperature, and microorganism species present in the compost. This explains why some articles mentioned longer degradation times, sometimes above 6 months [35, 161]. Although industrially compostable polymers such as PLA hold promise for better waste management system, some applications remain hard to reach for bioplastics.

PLA is generally produced from corn, sugar beet, maize, potato, and sugarcane. PLA has ester functional groups in its polymer-chain backbone, with hydroxyl and carboxyl groups at the end of the chain. These polar groups facilitate intermolecular interactions with water, namely through hydrogen bonding. Retained by the resulting hydrophilicity, water stagnating on a surface can promote bacterial and fungal growth. This might cause a durability issue for outdoors applications, as it has been well documented since 1997 [34] that aerobic micro-organisms such as bacteria and fungi can degrade PLA [35, 36].

As such, the susceptibility of bioplastics towards biodegradation in humid conditions limits their usage in outdoor applications and brings about the requirement for controlled humidity during bulk storage in warehouses. Tuning the surface properties from wetting (hydrophilic) to non-wetting (hydrophobic) could optimize the behavior of bioplastics such as PLA for different periods of its life cycle i.e. hydrophobic during use and storage to prevent degradation, hydrophilic at the end of life to promote microbial attachment and thus compostability. The benefits of hydrophobicity can vary significantly depending on the application. For instance, making agricultural nets hydrophobic can reduce humidity levels, which in turn inhibits fungal and bacterial growth. This reduction in microbial growth can lead to a decreased need for fungicide usage [37]. In the case of PLA, several surface engineering methods have been explored, such as PICVD (photo-initiated chemical vapor deposition) [37, 91], inductively coupled plasma with fluorocarbon-based coatings [113], electrospinning [114, 115, 162], and one-step spraying methods [116], which were successfully used to impart hydrophobic surface properties. Our research team developed a two-step solvent induced recrystallization protocol, called dip-dip-dry (DDD), to modify the wettability of lab-scale and commercially available PLA for outdoor applications [37, 92, 118], imparting hydrophobicity. During usage, hydrophobicity is desirable but as shown earlier, at the end of life, micro-organism

attachment to the surface depends on surface wettability [38]. Hydrophobicity can be conferred either through surface morphology (roughness) or chemical composition change (non-polar groups) – in both cases, this prevents water from reaching the material surface efficiently, or even penetrating inside the material, thus hindering degradation. Thus, surface-treated compostable bioplastics are more likely to last longer in the environment and accumulate, since degradation is hindered by hydrophobicity.

As such, it is necessary to restore a bioplastic's hydrophilicity to allow it to become compostable anew after the intended use in outdoor settings. UV irradiation is a potential path to switch the wettability of a material by photodegradation causing oxidation [146]. Under exposure to radiation, chain scission occurs reducing the molecular weight and leading to formation of oxidized end groups that are polar which contributes to increasing the wettability. For example, exposing glass substrates to Hg-discharge lamps (emitting the 200-300 nm UVC range) has been shown to increase surface wettability [163]. Hyun Jeong Jeon et al. [148] reported water contact angle decreased moderately from 84.5° to 73.9° on PLA following a 24h exposure to UVC lamps emitting at 185 and 254 nm, with irradiance at $6.41 * 10^{-3}\ mW.cm^{-2}$ and $3.22\ mW.cm^{-2}$, respectively for each wavelength. Similarly, via an energetic dose of $63.6\ J.cm^{-2}$, Koo and Jang [164] found an increase in PLA hydrophilicity with water contact angle decreasing from 61.4° to 39.2° after UVC-Mercury irradiation. Herein, this research demonstrates that, a solvent-treated hydrophobic PLA substrate can be reverted well below its original wettability, all the way down to capillary wicking behaviour, with a very similar UV energetic dose and short treatment time (2 h). This treatment does permanent change to the surface as the durability of this change was tested for one year. The reason for this significant change is determined by studying surface chemistry and morphology alterations.

4.3 Experimental

4.3.1 Materials

Commercial grade PLA 6202D with average molecular weight of 140 kDa and a 2 wt.% D-isomer content (NatureWorks LLC, USA) was pressed to form amorphous PLA discs as described in our group's earlier publications [118, 165]. Prior to pressing, PLA pellets were dried over 24 h at 80

°C under vacuum (19-22 mmHg). PLA pellets were then put in a mold between two PTFE sheets and sandwiched between metal plates. The whole structure was then pressed in a heating press (model 3912, Carver Inc., US) set at 180 °C under air atmosphere. During the first 4 min, no pressure was exerted, until the desired plate temperature was reached. Then, pressure was increased to 4.45 to 5.34 MPa and held for 2 min. Finally, the pressure was released, and the samples were quenched in cold water. Discs were then trimmed, washed and finally dried in the fume hood for at least 24h. The same protocol was done for microtomed samples, where PLA rods were pressed instead of PLA discs.

Alternatively, these same PLA pellets were ground with a Daigger-WAR700S mill after dipping in liquid nitrogen to make PLA powder. Powders are useful when studying a surface treatment due to their high surface area. Acetone (ACS grade 99.5% anhydrous) and diiodomethane (Thermo Scientific Chemicals, 99%, stabilized) were purchased from Fisher Scientific, and deionized water (DIW) with a conductivity of 1 $\mu S \cdot cm^{-1}$ was provided by the university infrastructures.

4.3.2 DDD-treating discs

DDD is a two-step solvent induced recrystallization protocol [118]. In a solvent bath (acetone), polymer chains at the surface of the amorphous PLA discs are slightly dissolved over 10 min. Mobile chains remaining on the surface will shrivel when dipped in a coagulant bath (DIW) for an additional 10 min. During this phase, recrystallization occurs as the chains contract due to water acting as a nonsolvent for PLA. This causes formation of a water-repellent microstructured surface. The DDD-treated samples are then dried for 48 h in the fume hood.

4.3.3 Exposure to UV

PLA discs (diameter 2.5 cm, thickness 1.0 mm) were placed 3.5 cm below a UVC low pressure Hg discharge lamp (Cole-Parmer, VL-230.G) with a primary emission peak at 253.7 nm and secondary emission peak at 184.9 nm. The lamp was preheated for 30 min prior to sample treatment to ensure that irradiance was constant during the experimenting time (less than 1% change over 30 min). Average irradiance was 8.7 $mW.cm^{-2}$, measured by a ILT1700 Research Radiometer (International Light Technologies). Exposure times varied from 30 min (15.7 $J.cm^{-2}$) to 2 h (62.6 $J.cm^{-2}$.)

4.3.4 Characterization

Wettability change was assessed using the sessile drop method with an OCA-20 optical contact angle measuring and contour analysis system from Dataphysics. Static contact angles were measured 2 seconds after laying a 5 µL water droplet or 1 µL diiodomethane droplet on surface (3 measurements per disc, conducted in triplicate). In the case of UV-exposed DDD-treated discs, the time needed for droplet disappearance on the surface via adsorption and evaporation was also recorded.

Morphology was studied using scanning electron microscopy (SEM). A Hitachi, Model TM3030Plus Tabletop microscope was used for low magnification imaging with beam voltage at 5 kV, 5.0 mm working distance, combined with a sputter coater to apply a conductive 25 nm-chromium coating to PLA discs (model SC502, Fisons Instruments, U.K., 30 s, 40 mm sample target distance, 16 W). A Low Vacuum Scanning Electron Microscopy (LVSEM), Thermo Fischer Scientific Quatttro S, ETD detector, with beam voltage at 2 kV, current at 5.6 pA, working distance 5.6 mm, combined with same sputter coater model but applying a thin 5 nm conductive gold coating on the PLA discs, was used to observe fine morphology at higher magnification.

Chemical composition was assessed using Fourier Transform Infra-Red (FTIR) spectroscopy (Spectrum 65, Perkin Elmer, operated in attenuated total reflectance mode with a ZnSe crystal, analysis range of 4000-600 cm^{-1}, 64 scans, 0.5 resolution). Near-surface analysis was also conducted using X-ray Photoelectron Spectroscopy (XPS) with a VG ESCALAB 3 MKII apparatus. Monochromatic Al Kα radiation with an energy of 1486.68 eV was used. Residual gas pressure was below 10^{-7} Pa. The survey scan (pass energy 150 eV) was used to confirm atomic composition and high-resolution spectra (pass energy 20 eV) were used to quantify the distribution of chemical bonds. Smart background subtraction was applied using the Avantage software (version 6.6.0) to process the signal. Peak fitting and bond percentage quantification was done with the peak constraint method, allowing 0.1 eV and 0.1% variation in the peak's full width half maximum and Lorentzian / Gaussian (L/G) mix ratio (%) respectively for peaks of same spectrum.

Thermal behavior was assessed using differential scanning calorimetry (DSC) with a DSC Q2000 (TA Instruments). The cooling and heating rates were fixed at 10 °C/min from 25 to 200 °C (2

heating/cooling cycles, 5 mg sample). Thermogravimetric analysis (TGA) was conducted up to 800 °C with a Q500 TGA (heating rate at 10 °C/min, 15 mg sample). Thinner discs (diameter 3.2 cm, thickness 0.5 mm) prepared with same pressing protocol were used for DSC and TGA in order to minimize the effect of the bulk on the results. For both TGA and DSC, tests were performed under nitrogen atmosphere. Crystallinity changes were further measured using X-Ray Diffraction (XRD) with a D8 ADVANCE (Bruker), using a copper source ($K_\alpha = 1.54060$ Å), operated at 40 kV and 40 mA, in angle increments of 0.05°, from 5 to 50°. For XRD, bigger discs (diameter 3.8 cm, thickness 2.6 mm) were produced to fit the measurement range. Crystallinity was calculated by doing the integral method comparing area under baseline for amorphous percentage and area between baseline and curve for the crystallinity. Finally, gel permeation chromatography (GPC) was used to measure the effects of treatment on polymer chain length with an Agilent PL-GPC 120 when assessing powders or microtomed slices and with an Agilent HPLC 1260 Infinity II for discs. Shodex column KF-804 and refractive index (RI) detector were used. PLA samples were dissolved in THF at a concentration of 3 $mg.mL^{-1}$ and PS standards were used for calibration. Finally, PLA rods (length 13 mm, width 5 mm, thickness 0.3 mm) were cut using microtome with a Leica RM2165 equipped with an LN21 cooling system to observe morphology and mechanism of rupture few microns below surface. Every experiment was conducted in triplicate except TGA and GPC that were conducted in duplicate.

4.4 Results and discussion

4.4.1 Wettability

PLA samples treated by the DDD solvent-based process yielded hydrophobic substrates, as expected; the resulting contact angle of 147.2 ± 0.6° corresponds to the 0 min UVC exposure data in Table 1. The water contact angle on the untreated PLA is approximately 95° (initial test value near 100°, final test value near 90° after 35 days) as shown in **Figure 4.1**. Upon UVC exposure, a switch in wettability was observed: the contact angle dropped from 147.2° to 22.5° after 2 h exposure. These discs behave as capillary wicking substrates. The water droplet spreading on the surface and subsequent infiltration are shown in the Supplementary Material (video S1-a). Two phases are generally observed when studying the wettability of treated substrates using the sessile drop method: (1) the drop attempts to stabilize on the surface; (2) the droplet's contact points no

longer move, but the droplet continues spreading as in the capillary wicking regime until it disappears by evaporation and adsorption into the surface [46]. The time needed to reach the contact angle is identified as the stabilization time in **Table 4.1** and is recorded along with the time needed for droplet disappearance by evaporation or both adsorption and evaporation as a function of UVC exposure time. Wettability experiments were conducted on the same day at a constant room temperature of 24.0 °C and 10% ambient relative humidity (RH). For 30 min UVC exposure, very little change seems to have occurred. However, upon increasing exposure (45 min and 1h), a greater decrease to an hydrophilic state occurred and a large time for droplets stabilization is observed. Finally, increasing up to 2h greatly increased the wicking behavior, reducing droplet stabilization and disappearance time.

Table 4.1: Water contact angle (WCA), and dynamics of adsorption and evaporation of 5 µL droplet on DDD-treated PLA for different time of UVC exposure (0, 30, 60, and 120 min). Note: 0 min corresponds to unexposed DDD-treated PLA

UVC exposure time	**0 min**	**30 min**	**45 min**	**60 min**	**120 min**
Average WCA (°)	147.2 ± 0.6	140.1 ± 3.0	104.4* ± 22.1	46.6* ± 9.8	22.5* ± 3.1
Time for droplet stabilization (s)	≤2	≤2	1147 ± 351	642 ± 91	25 ± 5
Time for droplet disappearance (s)	2506 ± 126	2392 ± 41	2588 ± 90	942 ± 30	93 ± 3

**stabilizing angles*

The surface energy of the 0 min (unexposed), 30 min, 60 min, and 120 min exposure samples was assessed using Wu's harmonic mean method (in the SCA 20 software). Water was retained as the polar liquid for this test, with a dispersive energy of 22.60 $mN.m^{-1}$ and a polar component of 50.20 mN/m. The high-dispersive component liquid used for the calculations was diiodomethane, with a dispersive energy of 49.00 $mN.m^{-1}$ and a polar component of 1.80 $mN.m^{-1}$. As illustrated in Supplementary Material videos S2, the adsorption dynamics of diiodomethane in DDD-treated PLA are rapid for all exposure times tested. Furthermore, diiodomethane fully wets all DDD-

treated samples. Consequently, the diiodomethane contact angle on UVC-exposed and unexposed DDD surfaces was set to 0 for all samples studied. From the surface energy measurement data reported in **Table 4.2**, it is evident that the dispersive component of the UVC-exposed discs remains unaffected, whereas there is a significant increase in the polar component of surface energy after 1 h and 2 h of UVC exposure.

Table 4.2: Surface Energy (SE) table of DDD-treated PLA as a function of UVC exposure time (0, 30, 60, and 120 min)

Exposure time	**0 min**	**30 min**	**60 min**	**120 min**
Total SE $(mN.m^{-1})$	44.0±0.1	43.8 ± 0.1	67.7 ± 4.4	78.9 ± 0.9
Dispersive component $(mN.m^{-1})$	44.0±0.1	43.8 ± 0.1	46.1 ± 0.1	45.9 ± 0.1
Polar component $(mN.m^{-1})$	0	0	21.6 ± 4.5	32.4 ± 0.4

In agreement with previous literature, UV exposure can mildly affect the wettability of untreated PLA. However, UVC exposure (2 h) on DDD-treated PLA induces a complete switch in wettability. To further explore this, similar UVC exposure was performed on untreated (neat) PLA discs. As shown in Figure 4.1, no significant change in contact angle was observed between UVC-exposed and unexposed neat PLA discs. Water contact angle (WCA) measurements were repeated over time to assess potential long-term effects. Over a period of 28 days, no differences were noted between UVC-exposed and unexposed samples. The slight variation observed over time can be attributed to differences in relative humidity, which has been shown to influence WCA measurements and introduce experimental error [64].

These findings lead to two important conclusions. First, when comparing untreated and DDD-treated UV-exposed samples, it is evident that the roughness and porosity introduced by the DDD treatment significantly amplify the effects of UVC on PLA compared to untreated samples. Second, when comparing UVC-exposed and unexposed DDD-treated samples, it becomes clear that UVC exposure interacts with or modifies the DDD-treated surface. After 2 hours of UVC exposure,

DDD-treated discs exhibit capillary wicking behavior, a phenomenon that persists even one year after UV exposure (see Supplementary Material video S1-b). This underscores a permanent change in the surface morphology or chemistry.

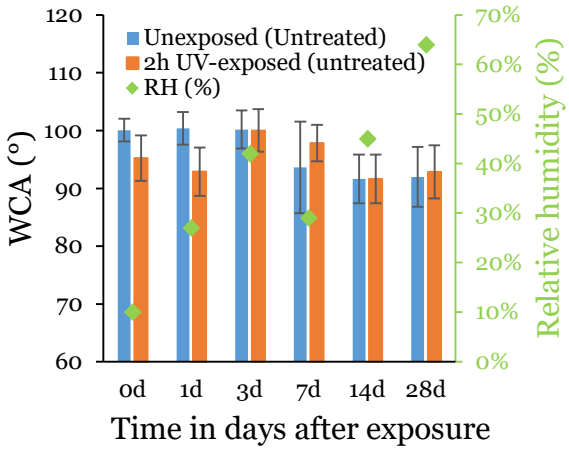

Figure 4.1: Water contact angles of 2h UVC exposed and unexposed untreated discs (neat PLA) as a function of time after the UVC exposure. Day 0 being the day of exposure to UVC

This permanent change was confirmed by GPC, showing that UVC exposure on DDD-treated PLA discs and powders caused chain scission: the number and weight average molecular weight of the polymer were significantly reduced (**Table 4.3**). This is consistent with UV effect on molecular weight noted in the literature [166-168]. However, the potential effects of cross-linking must be considered and are discussed in detail in Supplementary Material Section 2.

Table 4.3: Number and weight average molecular weight (respectively M_n and M_w) and polydispersity index (PDI) obtained by GPC of Untreated, DDD-treated and UV DDD-treated PLA powders, DDD-treated and UV DDD-treated PLA discs, average of two repetitions. Molecular weight distributions are presented in Supplementary Material Section 2.

	$M_n\ (g.mol^{-1})$	$M_w\ (g.mol^{-1})$	*PDI*
Untreated PLA powder	$7.30 * 10^4$	$1.27 * 10^5$	1.7
DDD-treated PLA powder	$6.96 * 10^4$	$1.29 * 10^5$	1.8

UV DDD-treated PLA powder	$2.54 * 10^4$	$6.89 * 10^4$	2.7
Untreated PLA disc	$8.69 * 10^4$	$1.26 * 10^5$	1.5
DDD-treated PLA disc	$8.92 * 10^4$	$1.41 * 10^5$	1.6
UV DDD-treated PLA disc	$4.18 * 10^4$	$8.52 * 10^4$	2.0

UVC radiation has sufficient energy to break bonds and causes chain scission (at 253.7 nm, the photons carry 4.88 eV, sufficient to break C-C and C-O bonds, at 3.7 and 3.5-4.3 eV, respectively [169]). This mechanism is often shown in literature to be associated with a surface oxidation.

4.4.2 Surface chemistry

UV interactions with polymers have been well documented [164, 166, 170-180]. In the case of PLA, the mechanisms identified in the literature are presented in **Figure 4.2**. Norrish type II reactions are the most common pathway for PLA under UV exposure, namely at wavelengths below 300 nm [181], such as excimer lasers (172 nm) [178], low pressure Hg discharge lamps (253.7 nm and 185 nm) [173, 179], and other lamps emitting some UVC radiation alongside visible radiation [166]. UVB radiation 280 – 315 nm range in the UV band) have also lead to Norrish type II reactions under direct sun exposure of PLA [176]. At wavelengths above 300 nm, β-scission leading to anhydride group formation is generally reported [174, 177]. Nevertheless, the degradation mechanisms based on wavelength can change depending on conditions: Zaidi et al.[176] showed that, when adding organoclay (organically modified clay obtained by replacing natural cations of the clay mineral with cationic organic surfactants) to PLA, the degradation mechanism shifted from Norrish type II to radical abstraction of the tertiary hydrogen of PLA, leading to peroxide formation followed by β-scission. Furthermore, in the case of UVC low pressure Hg discharge lamps (primary emission at 253.7 nm), α-cleavage of the ester linkage was the degradation mechanism reported when combined with ozone [164]. All degradation mechanisms mentioned above have been identified in most cases using FTIR.

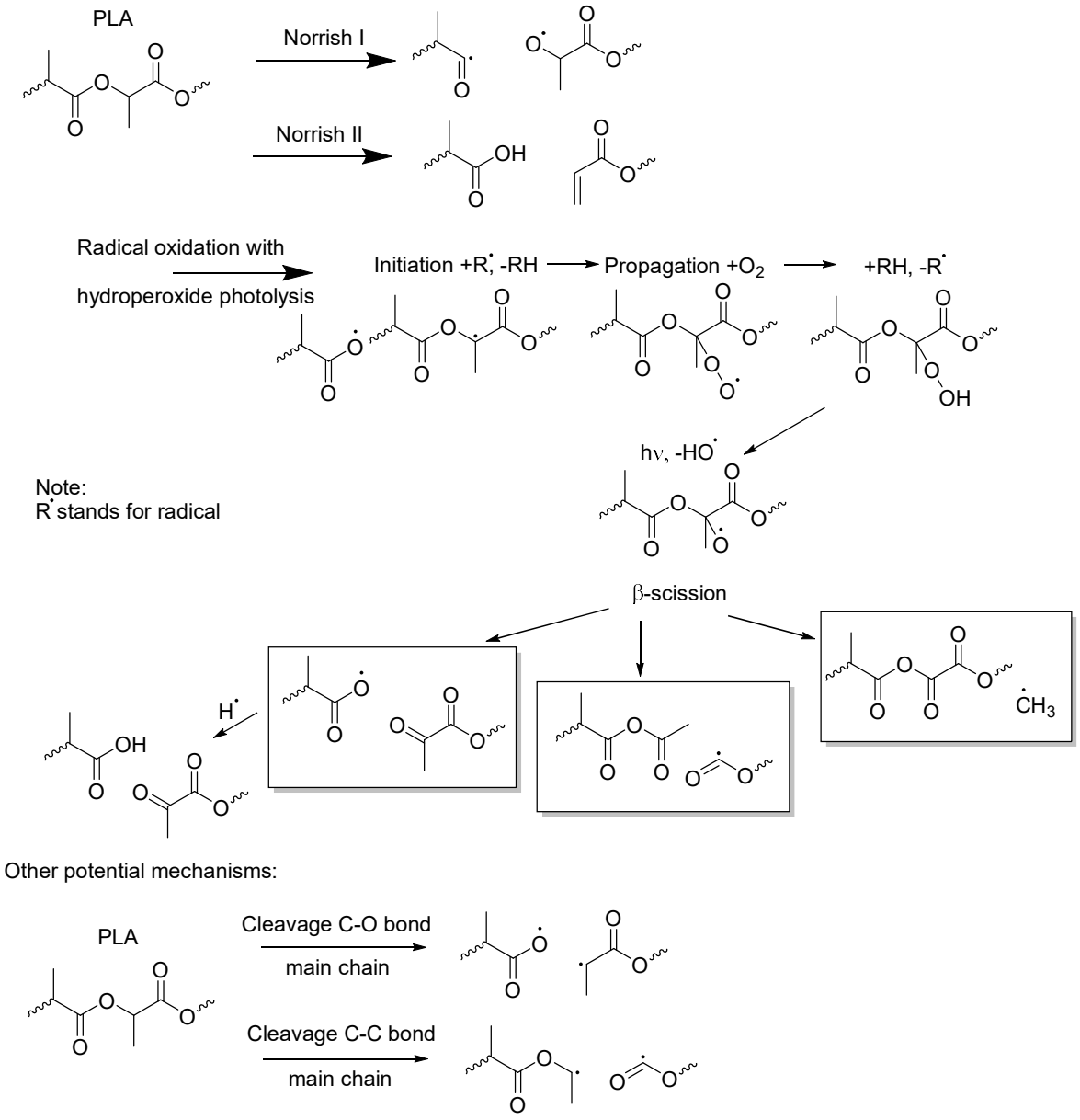

Figure 4.2: Schema of PLA degradation mechanisms commonly described in literature resulting from UV exposure

In the present case, no change that could explain this difference in wettability is observed using FTIR analysis (**Figure 4.3**). Specifically, no peaks corresponding to anhydride from β-scission (near 1845-1847 cm^{-1}) [173, 174], or no C=C bonds of Norrish type II reactions (near 1654 cm^{-1}) [176, 179] are observed. As shown by Smith [182], the alkene band in the range 1600 – 1680 cm^{-1} isn't totally reliable to detect the presence of alkene as these vibrations can be nonexistent

depending on substituents and arrangement around the double bond. To confirm the absence of alkene groups, the C-H stretching vibrations bands have to be investigated. As there was no appearance of a new C-H stretching peaks between 3100 and 3000 cm^{-1}, Norrish type II reactions can be excluded.

The only change of note is the appearance of sharp drop in the C-H asymmetrical and symmetrical (2850 cm^{-1} and 2921 cm^{-1}) stretching vibrations belonging to CH_2 groups [183]. Less significant changes are observed regarding C-H symmetrical (2945 cm^{-1}) and asymmetrical (2999 cm^{-1}) stretching vibrations belonging to CH_3 groups [164, 173]. This change has been found via repetitions to only be due to humidity absorption of PLA. There is similarly no change in the 3200-3500 cm^{-1} region, where peaks originating from -OH vibrations forming both inter and intrachain hydrogen-bonds would appear [184] via moisture adsorption.

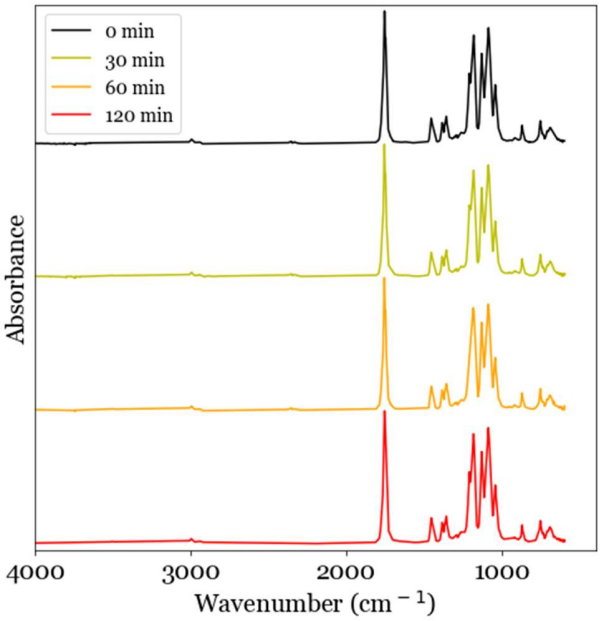

Figure 4.3: FTIR spectrum of DDD-treated PLA discs for different UVC exposure time (0, 30, 60, and 120 min). 0 min exposure referring to unexposed DDD-treated PLA

Stacking curves together, the only peak that moderately increased as a function of UVC exposure corresponds to carbonyl groups (1723 cm^{-1}) [164, 178], which could be generated through α-cleavage. Further quantification closer to the surface of the different atoms and bonds are needed.

The absence of relevant changes may be because FTIR is not a surface-sensitive technique. XPS is better suited at characterizing surface bonds, as it is generally accepted that around 95% of the electrons reaching the detector will come from the first 10 nm of the substrate [185], which makes it a more surface sensitive technique than ATR-FTIR [186], whose depth of penetration is in the order of 1 µm [187]. XPS is thus effective to quantify the increase of oxygen content on a surface due to oxidation. This can be directly correlated with increases in the polar component and wettability changes as shown by Li et al. [188]. They employed O_2 plasma to transform a superhydrophobic coating laid on various surfaces into a hydrophilic, water spreading surface, directly correlated with an increase in the surface oxygen content. Along similar lines, Ren et al. showed a relative increase in oxygen content using XPS on plasma treated PLA to improve wettability and change contact angle from 120° to a wicking surface in less than 100s exposure [189].

XPS analysis showed no significant changes in the carbon and oxygen content between unexposed and UVC exposed PLA substrates, nor in the chemical bonds when analyzing the C1s spectra (**Figure 4.4**).

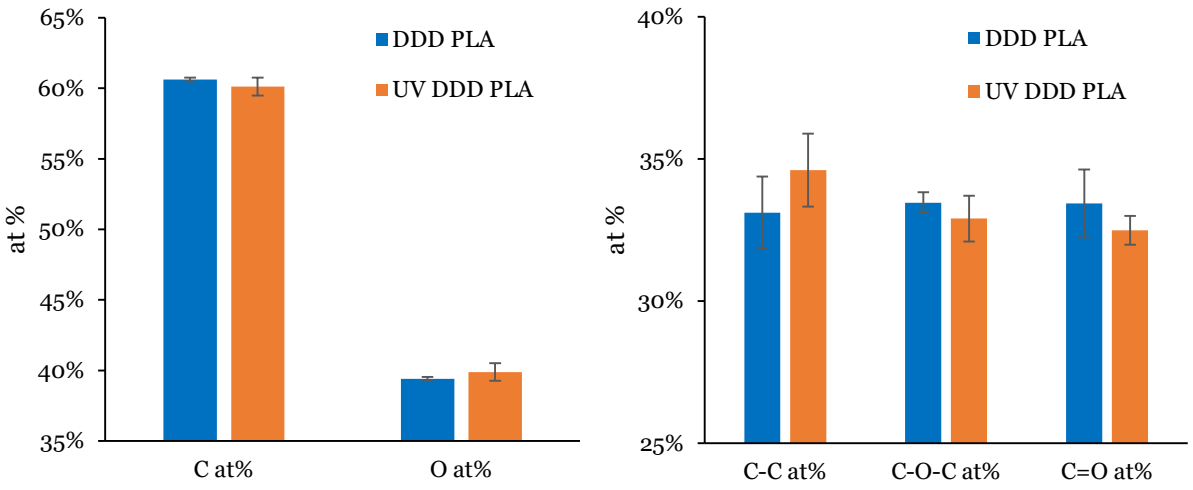

Figure 4.4: XPS results on chemical composition and atomic percentage of chemical bonds comparing 2h UVC exposed and unexposed DDD-treated PLA discs

The only significant change that could be detected is in the peak shapes. Peaks of the UVC exposed samples are much more defined (**Figure 4.5**), which relates to a better ordered surface and a

potential change in either surface morphology or crystallinity (section 3.3), or in the polymer chain's capacity to rearrange due to lower molecular weight which has consequences on thermal properties (section 3.4).

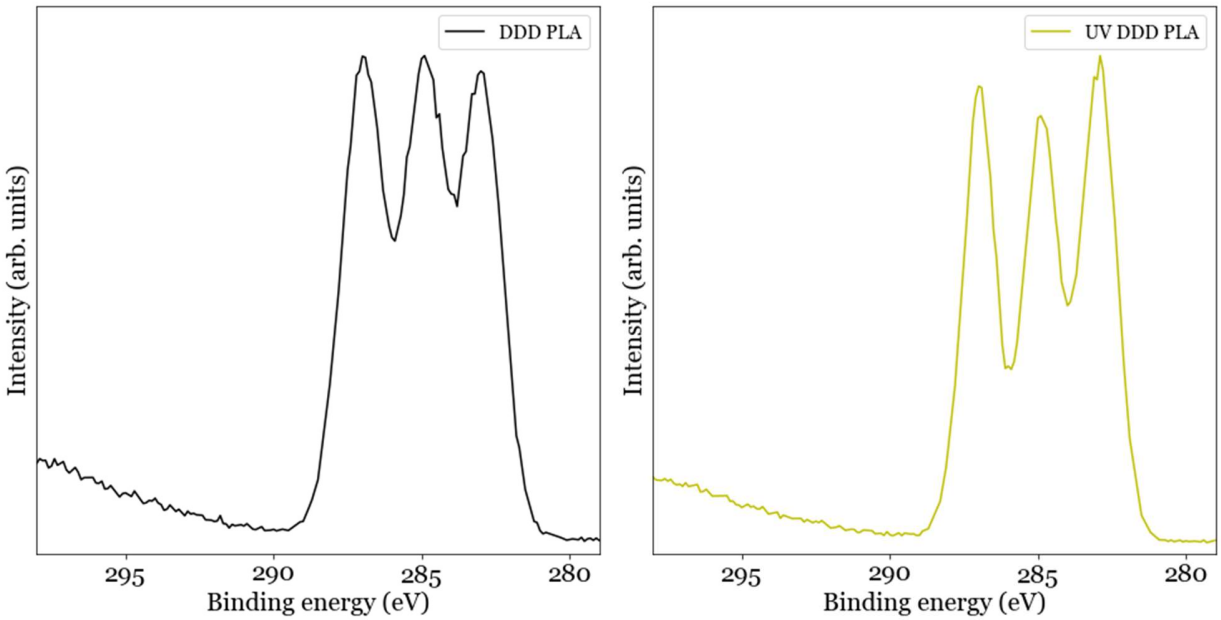

Figure 4.5: XPS C1s spectrum of a typical repetition of A) DDD-treated PLA samples B) 2h UVC exposed DDD-treated PLA samples

As no significant change in surface chemistry can explain the wettability switch occurring with UV exposure, surface morphology and crystallinity were investigated.

3.3 Surface morphology and crystallinity

As can be seen on SEM micrographs (**Figure 4.6**), there are no significant differences in the fine and coarse morphology between unexposed and UVC exposed samples that could explain the wettability change.

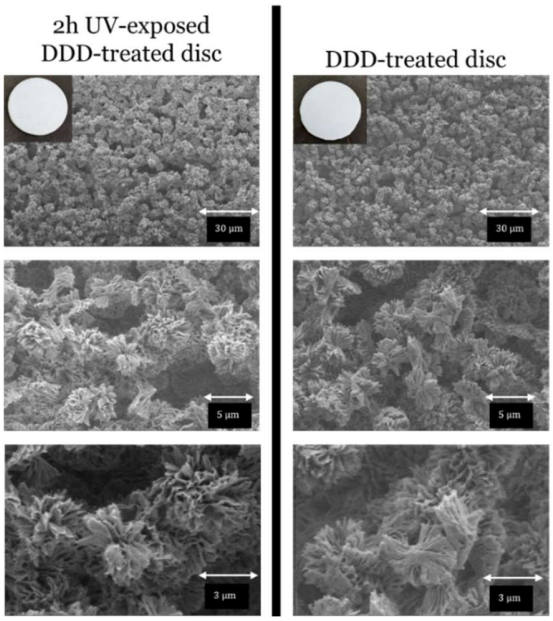

Figure 4.6: LVSEM pictures of 2h UVC exposed and unexposed DDD-treated discs

As shown in **Figure 4.7** and **Table 4.4**, no significant changes in the crystal types and degree of crystallinity χ_c are observed using XRD. Both 2h UVC exposed and unexposed DDD-treated samples are composed of α-crystals.

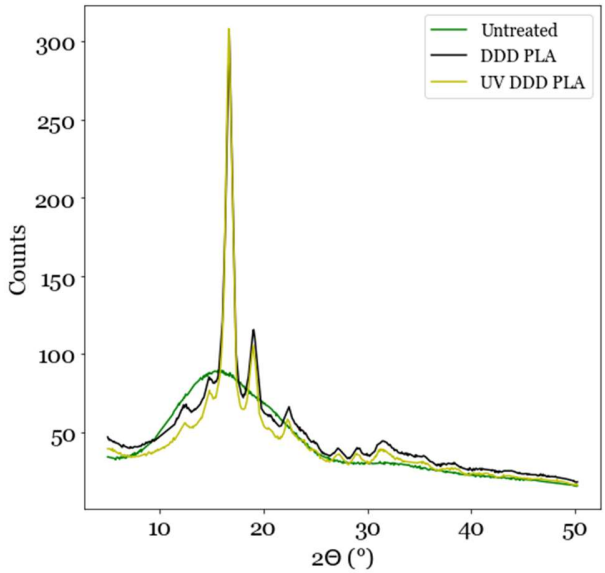

Figure 4.7: XRD on Untreated, DDD-treated, and 2h UVC exposed DDD-treated PLA discs

Table 4.4: Crystallinity values (obtained by XRD) of DDD-treated and 2h UVC exposed DDD-treated PLA based on the integration method

Samples	**Untreated PLA**	**DDD PLA**	**UV DDD PLA**
χ_c (%)	7.2 (±1.2)	34.6 (±0.9)	34.7 (±0.6)

As such, one necessarily expects to see changes in the polymer chain capacity to rearrange at a very small scale with significant impact on properties such as wettability.

3.4 Thermal properties

TGA results showed that for DDD-treated samples and 2h UVC DDD treated samples, weight change from solvent evaporation appeared at lower temperatures compared to untreated PLA (**Figure 4.8**). Following the derivative weight change (DTG), a degradation peak near 155 °C for both unexposed and UV-exposed samples can be seen in Supplementary Material Section 3.

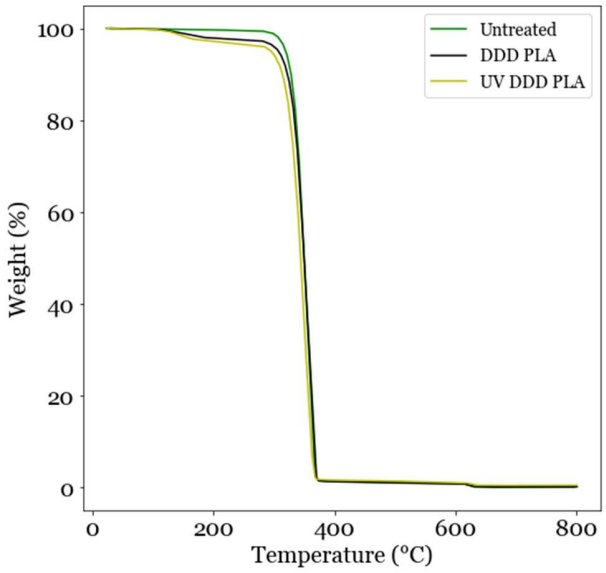

Figure 4.8: TGA curves for untreated, DDD-treated and 2h UVC treated PLA

As shown in previous works developing the DDD technique [118], there is residual solvent trapped in the material even after drying in vacuum for 48 h or more. After 48 h, Knoch et al. showed that

around 1.5% of residual solvent was trapped in the material – this corresponds to peak seen here at 155 °C, also corresponding to a roughly 1.5% weight change. In the case of UV-exposed samples, a slightly larger weight change is observed for each temperature below main degradation temperature. This may point to the fact that UV has already degraded the low molecular weight compounds and caused some changes. This effect is a consequence of lower molecular weight rather than thermal degradation as temperature of the exposed surface reaches 45 °C after 2h exposure. Thermal properties were further assessed using DSC. The first cycle of heating during DSC was deeply influenced by the presence of residual solvent trapped in crystals from the solvent-induced recrystallization process. As such, PLA thermal properties were extracted from the second cycle of the DSC tests. 2h UVC-exposed DDD-treated discs held significant recrystallization ability and a lower melting temperature as can be seen in **Figure 4.9** and **Table 4.5** due to their reduced molecular weight [137]. This was also confirmed to be true for powder as shown in Supplementary Material Section 4.

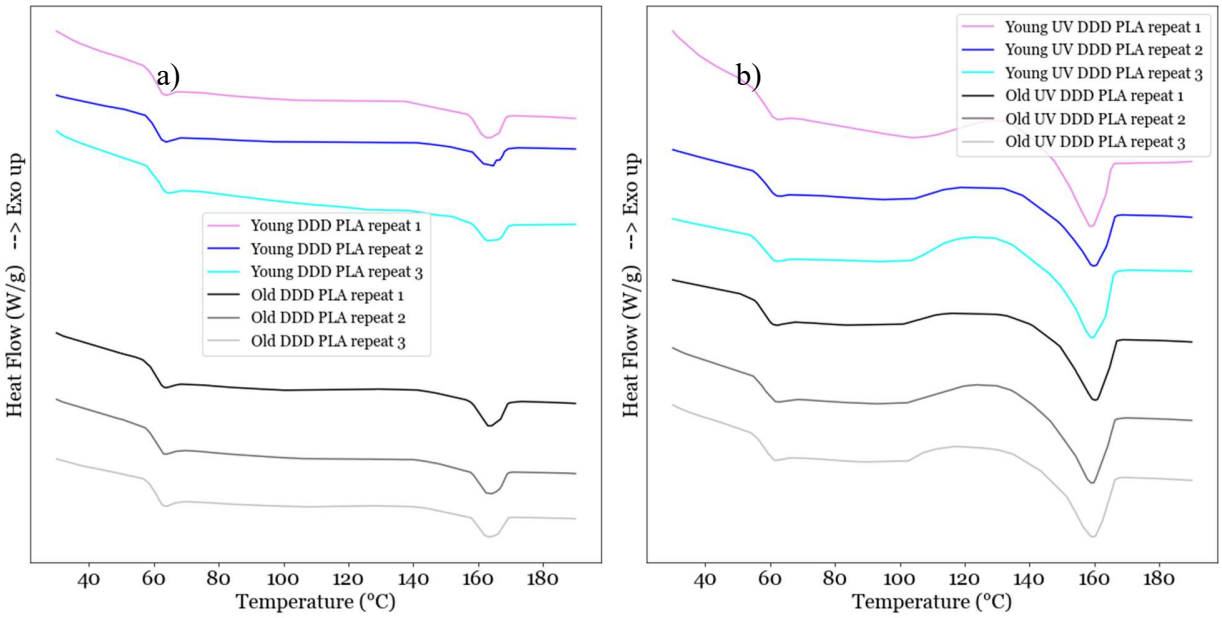

Figure 4.9: DSC results comparing young (2 days after DDD-treatment) and old (3 months after DDD-treatment) a) DDD-treated discs b) 2h UVC exposed DDD-treated discs

Table 4.5: Melting temperature (T_m), glass transition temperature (T_g) and percentage of recrystallization (%) during second heating cycle of DDD and 2h UVC exposed DDD-treated PLA. Heat of fusion of 100% crystalline PLA was considered to be 93 J/g [190]

Samples	**DDD**	**UV DDD PLA**
T_m DSC (°C)	164.1 ± 0.6	160.1 ± 0.3
T_g DSC (°C)	61.4 ± 0.5	58.9 ± 0.2
Recrystallization (%)	0.7 ± 0.2	7.5 ± 1.0

Thus, an increase in chain mobility can be inferred from the observed decrease in both glass transition temperature and melting temperature, due to the reduction in molecular weight. This increase in chain mobility is deemed to be sufficient to allow a change in polar bonds orientation on a textured surface.

3.5 Discussion

Given the various characterizations conducted, chain scission was retained to explain the observed increase in wettability following UVC exposure of DDD-treated PLA substrates. Chain scission results in the formation of oxidized groups at the newly created chain ends, which are likely to become polar due to reactions with surrounding oxygen species from the air reacting with UVC wavelengths as stated in Suzuki article et al [163]. During irradiation with Hg lamps, atomic oxygen is produced through a two-step process: first, oxygen molecules absorb 185 nm radiation, leading to the formation of ozone; then, 254 nm radiation decomposes the ozone, generating atomic oxygen. Chain ends are deemed to orient towards the surface to catch the atomic oxygen species and form new hydroxyl and carbonyl groups. As such, the increase in wettability and in polarity is attributed to the reorientation of polar oxygen bonds towards the surface. However, the increase in the number of polar groups is not detectable by FTIR or XPS measurements because the scission event only produces a slight rise in the number of chain ends compared to the high number of repetition units in a polymer. For a post-UVC exposure Mn equal to $4.18 * 10^4\ g.mol^{-1}$, and

considering a $72.1\ g.mol^{-1}$ molar mass for the lactic acid repeat unit, the new chains are approximately 580 repeat units long. Determining the exact number of chain scissions occurring per polymer chain is challenging. By induction from mechanism presented in **Figure 4.10**, it can be deduced that if p represents the number of chain scissions per polymer chain, then the number N of new groups per polymer chain before UVC exposure satisfies Equation 4.1.

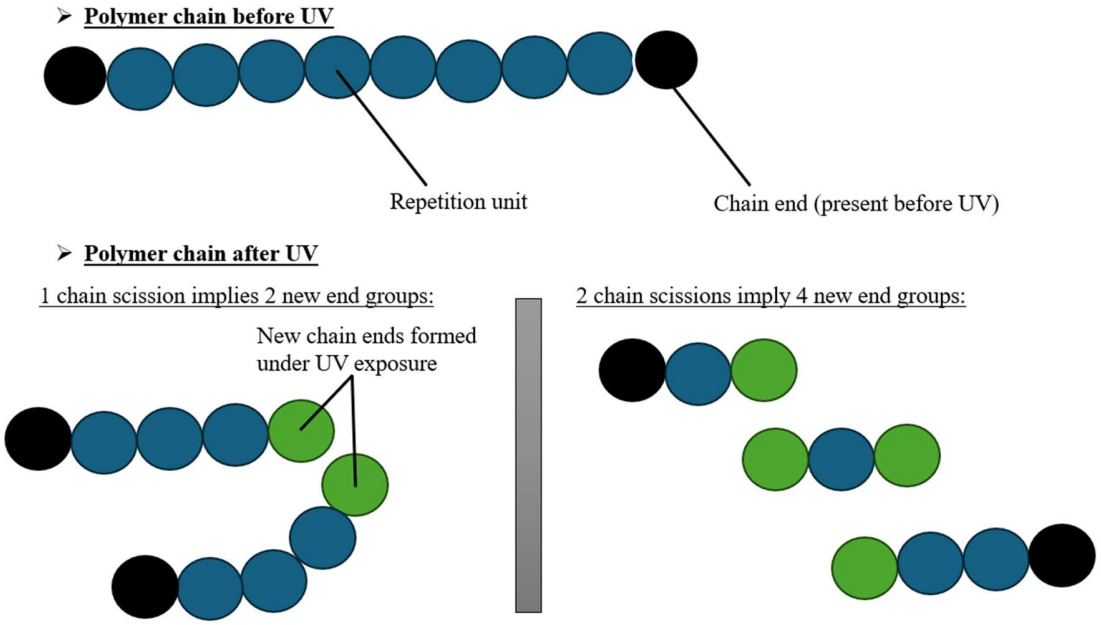

Figure 4.10: Schematic of number of chain ends depending on chain scission

$$N = \frac{2p}{p+1} = \frac{2}{1+\frac{1}{p}} \tag{4.1}$$

N is always lower than 2 for a linear polymer. Chain ends thus only represent less than ~ 0.3% of the total polymer. This means that there is an increase in the number of chains ends but compared to the large number of repetition units in the polymer chains these changes might not appear in chemical analysis. Nevertheless, it should be noted that this model considers the same intensity signal for all groups; it does not account for a higher density of chain ends near the surface from UV exposure, nor the presence of all the repetition units of the polymer backbone (out of the detection range of the apparatus). For example, XPS probes the first 5 nm of the material, which is considerably lower than the dimension of the polymer. Despite these shortcomings, this model

provides a first understanding of why the various spectroscopy techniques used were unable to distinguish the underlying mechanism of chain scission and the resulting reduced molecular weight.

Furthermore, the height of the microstructure might be affected by lower molecular weight. The topology of the substrate is created by the DDD treatment. Previous works by Kamegawa et al. [110] have shown that pillar height in patterned substrates can have a significant impact on wettability. Specifically, they found that in substrates such as the lotus leaf the pillars impacting wettability are on the order of 10 µm.

As shown in Supplementary Material video S3-a where a droplet was laid on the cross-section, wettability behavior change is mainly near the surface as the droplet is climbing up and spreading as it would be the case in a capillary wicking surface (Supplementary Material video S3-b). As such, penetration depths between 1 and 20 µm were studied by shaving off corresponding amount of matter from the top surface using microtome. From SEM observations on 20 µm microtomed rods (**Figure 4.11**), some unstable cracks [191] were seen due to the brittleness of the UVC exposed material compared to the unexposed DDD-treated PLA. Brittleness and potential effects of UVC exposure down to 20 µm were confirmed with GPC experiments where it was found that in the range 0-20 µm, the molecular weight was significantly lower than values given in Table 3 for discs and closer to powder due to surface specific effects. For 0 - 20 µm, number and weight average molecular weight were respectively $2.20 * 10^4\ g.mol^{-1}$ and $6.06 * 10^4\ g.mol^{-1}$ as an average of two repetitions (including 12 samples for each repetition). In other words, UVC exposure did not only change the wettability of the surface, but also the mechanical failure mechanism of the subsurface, increasing PLA's inherent brittleness.

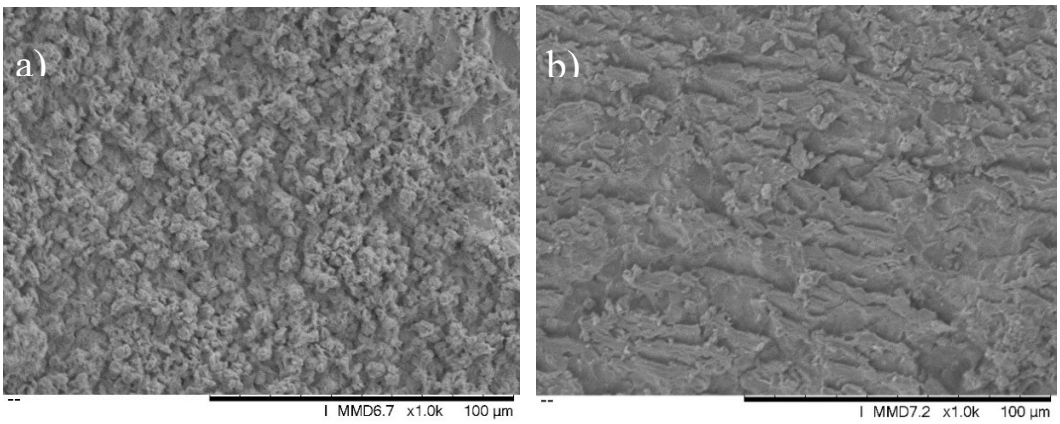

Figure 4.11: Image of 20 µm microtomed a) unexposed DDD-treated and b) 2h UVC DDD treated PLA rods at x1000 magnification. Image b) represents specific zones in the microtomed UV samples which were interesting to identify the rupture mechanism

4.5 Conclusions

This study introduced a complete wettability switch from almost superhydrophobic to capillary wicking in PLA that had been surface treated using solvent-induced recrystallization. This switch in wettability was triggered by UVC exposure, which caused chain scission, as confirmed by GPC, resulting in an increased number of polar chain ends. Despite this, no significant morphological changes were observed through SEM, and no alterations in chemical composition were detected by FTIR and XPS. Since UVC exposure had a pronounced effect on the solvent-induced recrystallized surface but not on the untreated amorphous PLA surface, it is inferred that the reduction in molecular weight involved the fragmentation of larger crystals into smaller ones, as suggested by changes in peak shape in XPS and decreased polymer characteristic temperatures (glass transition temperature and melting temperature) observed in DSC, as well as lower degradation temperature in TGA. This molecular rearrangement likely enhanced the mobility of the polymer chains, allowing reorientation of polar oxygen bonds towards the surface and thus impacting wettability. It was also shown that the mechanical failure mechanism was changed as demonstrated by the formation of unstable cracks. UVC exposure resulted also in surface brittleness. This UVC post-treatment approach paves the way towards facilitating biodegradation or composting of surface-treated polymer substrates.

4.6 Supporting Information

Cf. Supplementary Material (Appendix B).

4.7 Acknowledgements

The authors are grateful for financial support received from the Natural Sciences Engineering Research Council of Canada (NSERC Alliance grant), PRIMA Quebec, RQRAD scholarship support, CREPEC collaborative projects, MDB Texinov, and Dubois Agrinovation. The first author is thankful for academic support given from PhotoSEL Team, Josianne Lefebvre, CM^2 laboratory, Matthieu Gauthier, Claire Cerclé, Arthur Lassus, and Mary Hnatyshyn.

4.8 Authors contribution

William Simon (Protocol, Experiments, Analysis, Writing), Darius Klassen (Experiments, Analysis, Reviewing), Marie Mottoul (Experiments, Reviewing), Simon Ponton (Analysis), David Brassard (Analysis, Reviewing), Adya Karthikeyan (Protocol, Experiments, Analysis, Reviewing), Marie-Josée Dumont (Reviewing), Jason R. Tavares (Writing, Funding, Reviewing, Supervising). All authors have read and agreed to the published version of the manuscript.

4.9 Conflicts of interest

The authors declare no conflict of interest.

4.10 Table of Contents (ToC) text and figure

In light of increasing the applications of compostable materials, surface treatment on PLA to increase roughness and hydrophobicity has been investigated. However, modifying wettability might hinder degradation. UVC exposure has significant effects on the wettability of textured PLA substrates allowing complete wettability switch due to chain scission.

ToC (**Figure 4.12**):

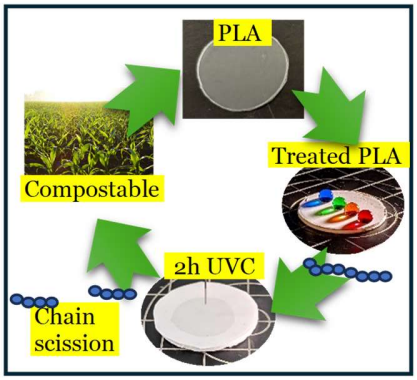

Figure 4.12: Graphical Table of Contents

CHAPTER 5 UPSCALING HYDROPHOBIC NETS PRODUCTION: EFFECT OF TENSION DURING SOLVENT-INDUCED RECRYSTALLIZATION

Upscaling is essential for adapting research to industrial applications. As discussed in the introduction, similar treatments are often implemented using roll-to-roll setups. These setups are favored due to their simplicity, automation, and ability to produce large quantities through near-continuous operation. There are two concurrent approaches to upscale treatment:

- Producing nets and modifying them directly in a roll-to-roll setup. This approach involves large baths and rolling elements to fit net size. A surface modified net is obtained.
- Modifying the yarns in a roll-to-roll setup and then knitting the yarns to form a net. A net made of surface-modified fibers is obtained.

This last approach is the most promising method for upscaling the treatment as yarns are already produced from a roll-to-roll setup after extrusion of polymer pellets and multiple cycles of heat stretching and relaxation, specific to the textile industry to reach higher mechanical properties by orienting the polymer chains in the fiber axis. Additionally, this method minimize space required.

As shown in Chapter 2, the impact of tension has already been investigated for different surface treatments such as mercerization. In the case of DDD treatment in a continuous process, where tension and strain-induced crystallization leads to the orientation of crystalline zones, challenges arise when solvent needs to free polymer chains at the surface to create texture through recrystallization. Introducing slack (additional matter provided to have a loose yarn) to increase chain mobility may therefore be necessary. However, to the author's knowledge, no data on the quantification of slack during surface treatment has been presented in the literature, or at least not in the manner presented in this report.

5.1 Materials and characterization

Acetone and DI water were as described in Chapter 4. Ethylene glycol (EG) was purchased from Sigma-Aldrich (≥99% purity, ReagentPlus®). In this chapter targeting upscaling treatment on exclusion nets, yarns and nets were used instead of discs. Monofilament and multifilament PLA yarns and nets were kindly provided by MDB Texinov®. Monofilament yarn has a diameter of $160\ \mu m$, whereas multifilament yarn are several fibers knitted, each with a diameter of $12\ \mu m$. Monofilament meshes are produced from knitting monofilament yarns withs a pore size of $0.8 \times 1.4\ mm$, whereas multifilament meshes are produced from multifilament yarns with a pore size of $0.85 \times 0.85\ mm$ (commercial name "Filbio", $34\ g.m^{-2}$).

SEM characterization techniques are identical to the description in Chapter 4. For cross-section observations, yarns were embedded in a PLA matrix to create a firm base for microtoming. This was necessary to ensure that the sharp glass knife of the microtome would cut through the yarn rather than deflecting it. Incorporation of yarns in the PLA matrix was done by melting PLA pellets, waiting for the polymer to come to a glassy state (near 80 °C) and then sticking the yarns in it. This support also ensured that the yarns remained vertically straight during SEM observation. The mechanical properties of the yarns were assessed using a dynamometer (Eisco newton force meter spring scale) with 10 N capacity to measure maximum load at rupture. The motors and their support (Compact Square DC Gearmotor, 12 V DC, 8 rpm) used in the continuous setup were purchased via McMaster-Carr alongside pulleys, and tubes. Aluminum containers were used to contain the liquids.

5.2 Treatment on PLA yarn

As a summary of the previous chapters, Figure 5.1 illustrates the Dip-Dip-Dry treatment applied to an amorphous material. For crystalline materials, an additional preheating step in EG is included to increase surface chain mobility, as per recommendations by [92].

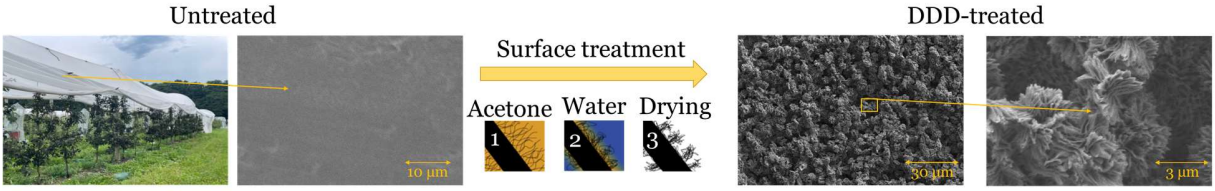

Figure 5.1: Illustration of the DDD treatment

5.2.1 Roll-to-roll processes and first steps on continuous operation

The treatment involves sequentially dipping the material into hot EG, acetone, and water, followed by drying. The primary method to upscale this treatment is to guide the yarn through these baths using a roll-to-roll process, as illustrated in Figure 5.2 below. This process is ideal for automation, with a winding spool at the end pulling the yarn through the setup. The pulling force, which can be assisted by an additional motor at the entry, unwinds the yarn from a spool feeding into the system. This setup is suited for yarns when rolling elements are pulleys but can be adapted for meshes / nets by using rolling tubes.

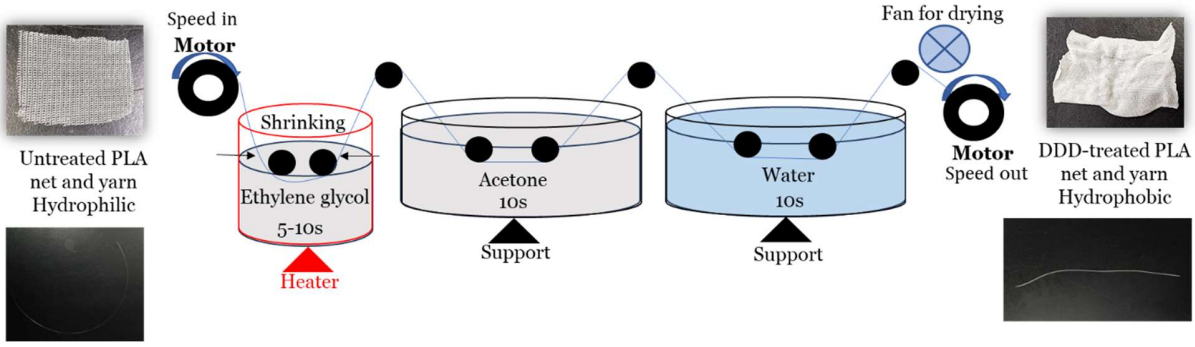

Figure 5.2: Illustration of the continuous process implementing DDD on a roll-to-roll setup

Tests under tension with movement driven solely from the pulling force:

Tests conducted under tension with movement driven solely by pulling force (without an entry motor) revealed significant differences in the appearance of the treatment, as shown in the SEM micrographs (Figure 5.3). On the left, the fiber bundle and texturing of the yarn are visible when a multifilament yarn is manually dipped in 130 °C ethylene glycol for 5 s, followed by 10 s in acetone and 10 s in water. On the right, when these parameters were applied to the continuous setup, no

fiber bundles were observed, and no significant surface modification appeared (with the exception of minimal surface ripping).

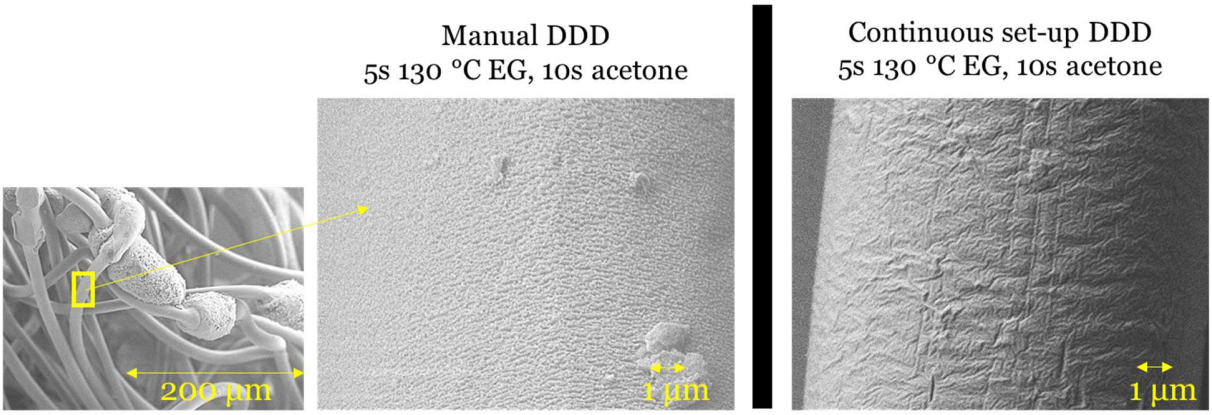

Figure 5.3: SEM images of multifilament yarn treated with same parameters manually and with continuous setup

In the continuous setup, additional parameters need to be considered, including the tension on the yarn, friction from contact with rolling elements, yarn speed and movement, and the transition time between each bath. The transition time between EG and acetone was first study. Reducing the transition time from 40 seconds to 22 seconds showed no effect, at temperatures up to 135 °C (Figure 5.4). Given the polymer's weak mechanical strength in the rubbery state above its glass transition temperature, excessive temperature or friction can cause the yarn to break. Temperatures above 135 °C led to frequent breakages, and thus, were generally not explored further.

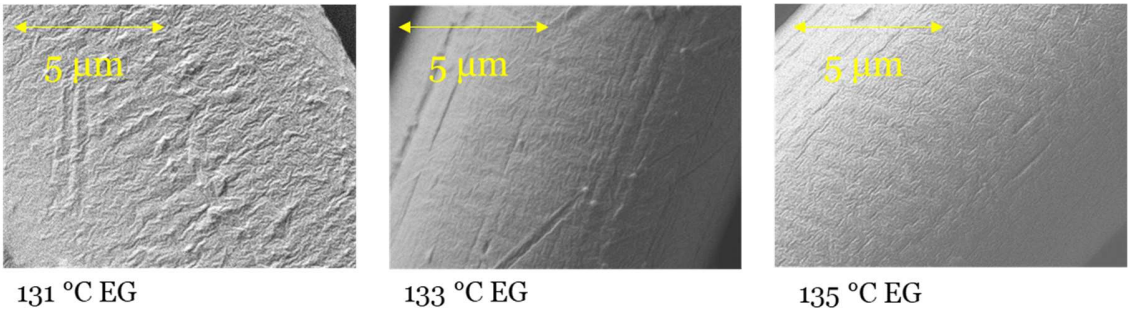

Figure 5.4: SEM images of multifilament yarn treated with the continuous setup with 22s transition time between EG and acetone. Different EG temperatures were tested: 131, 133, 135 °C

As shown in Figure 5.5, the transition time appears to have no effect even during manual treatment.

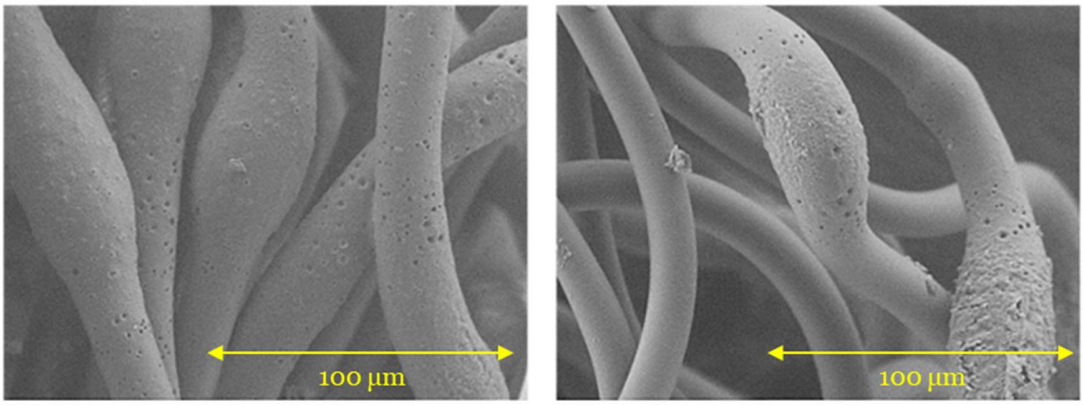

Figure 5.5: Manual treatment a) with 40s and b) without transition time between EG at 131 °C and acetone

Treated yarns exhibit a noticeable visual indicator: due to surface recrystallization, treated yarns or meshes appear brightly white, as the crystals reflect visible light wavelengths (Figures 5.2 and 5.9). No change in color was observed when the yarn was under tension in continuous operation, even with increased EG temperatures and extended residence times in both the EG and acetone baths. However, when extra length was manually introduced by adjusting the unwinding spool and allowing additional length to enter the EG bath, shrinkage occurred along with surface texturing, which became visible to the naked eye. Understanding the effects of tension and material dynamics during treatment is crucial to reveal the underlying mechanisms.

Reducing tension without adding additional matter:

Tension can be reduced by adding an additional container immediately after the unwinding spool, allowing the yarn to hang loosely and significantly decrease tension in the setup, as shown in the illustration below in purple (Figure 5.6). This container was filled with water to keep the loose yarn in contact with a surface and prevent it from being drawn into the fume hood. Accurately determining the exact amount of slack during operation was challenging since the yarn did not shrink in the EG bath, so ranges of slack were used instead. The samples appeared homogeneous,

and no treatment effects were observed under SEM (Figure 5.7), even with substantial amounts of extra length in the setup ranging from 10 cm to 30 cm for a 0.7 cm/s speed out.

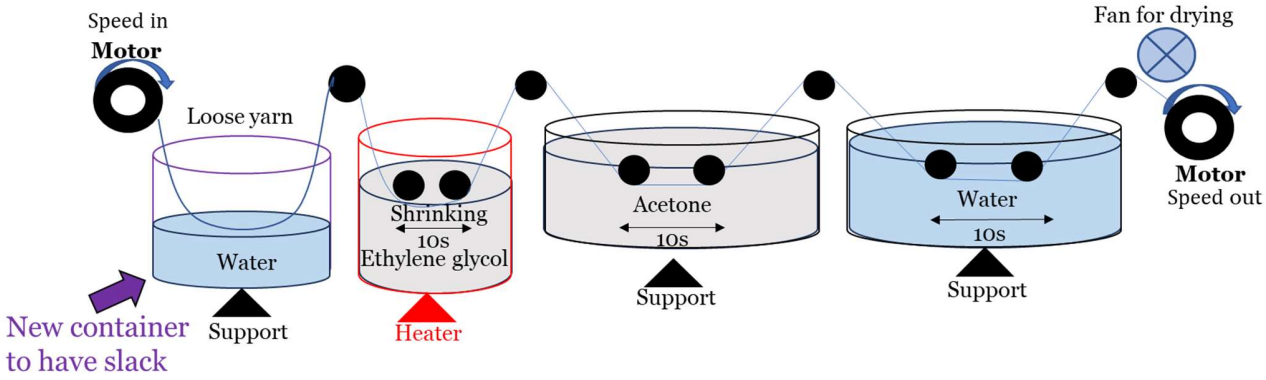

Figure 5.6: Schematic of continuous setup with loose yarn

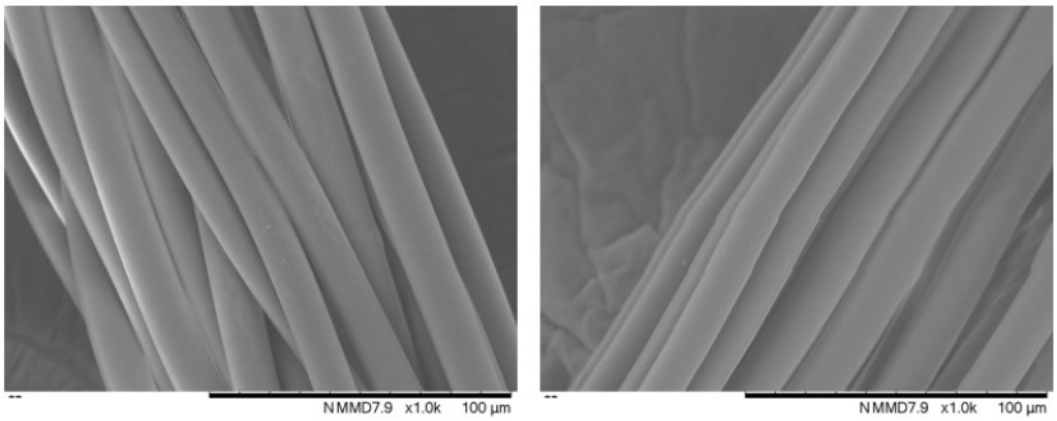

Figure 5.7: SEM images of yarn treated using the continuous setup with loose yarn for different range of extra length 10-20 cm (left) and 20-30 cm (right), followed by 10s in 130 °C EG, 10s acetone, and 10s water

From this experiment, it can be concluded that having a loose yarn to reduce tension is not sufficient to produce DDD microstructures. However, it is important to note that tension occurs in a roll-to-roll setup whenever the material comes to a stop. For instance, as the yarn is pulled, any friction point between the yarn and a rolling element after the EG bath generates instantaneous tension, diminishing the effect of extra length outside the setup.

5.2.2 Studying parameters in a process using a U-bar

A manual process was developed to study the effects of tension and additional length during treatment. A U-bar was used to secure a defined length of yarn between two fixed points on metal bars. The distance between these metal bars, referred to as the length of tension (LoT), is 12.2 cm for the U-bar shown in Figure 5.8.

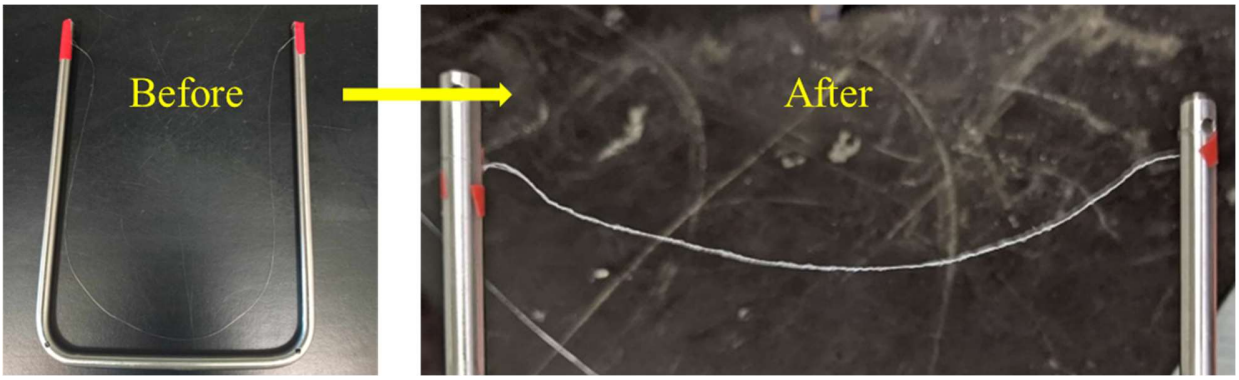

Figure 5.8: Images of multifilament yarn attached to the U-bar, before and after DDD treatment

To assess the influence of the extra length introduced in the EG bath, a ratio called *slack* was defined to quantify the additional length relative to the length of tension (LoT) (distance between the metal bars). Shrinkage is calculated as the ratio of the yarn length before and after treatment. If the shrinkage value equals the slack, it indicates that the yarn has shrunk precisely by the amount of extra length provided. This is explicitly shown in Figure 5.9 where samples with a slack value of 2 have shrunk to the point of being under tension, whereas at slack values of 2.25 and 2.5, the shrinkage did not equal the slack as some remaining curvature can be observed in the yarns. Shrinkage cannot exceed the slack; otherwise, it would indicate that the yarn has broken. This relationship is illustrated in the figure below with a red dotted line.

$$Slack = \frac{Length\ before\ treatment}{LoT} \tag{5.1}$$

$$Shrinkage = \frac{Length\ before\ treatment}{Length\ after\ treatment} \tag{5.2}$$

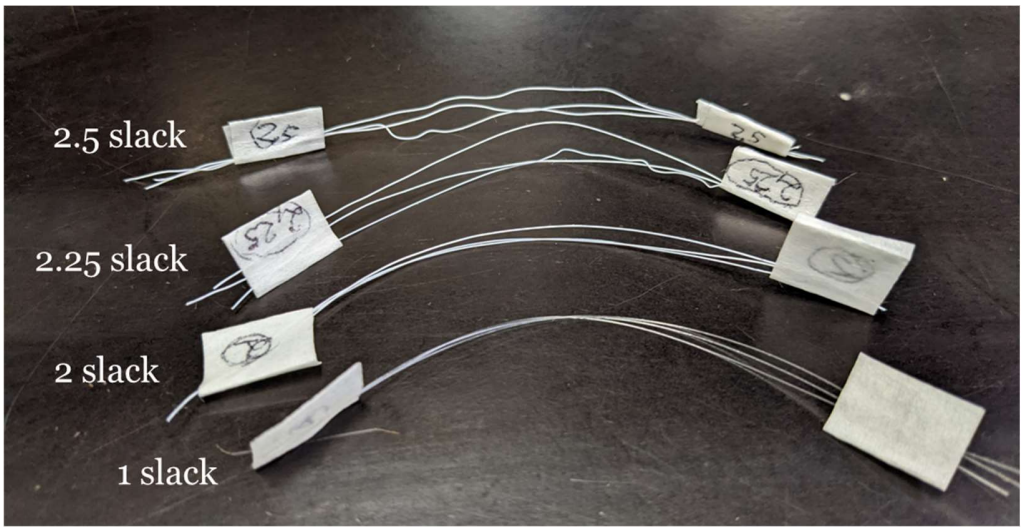

Figure 5.9: DDD-treated monofilament yarn with different slack values: 1, 2, 2.25, 2.5 using a U-bar process.

Data about shrinkage and slack were collected for different temperatures and for both multifilament and monofilament yarns.

Multifilament yarns

SEM images of multifilament yarns clearly demonstrate the importance of providing extra length in the form of slack (Figure 5.10). In Figure 5.10.a, it is evident that, under a slack value of 1, the individual filaments of the multifilament yarns remain untreated, as the surface roughness is similar to that of untreated fibers. In Figure 5.10.b, a slack ratio of 2 reveals the formation of surface texturing and micropores on the yarn. This effect is even more pronounced in Figure 5.10.c, where a slack ratio of 2.5 results in increased surface texturing and yarn enlargement. These observations indicate that slack plays a crucial role in allowing surface modification.

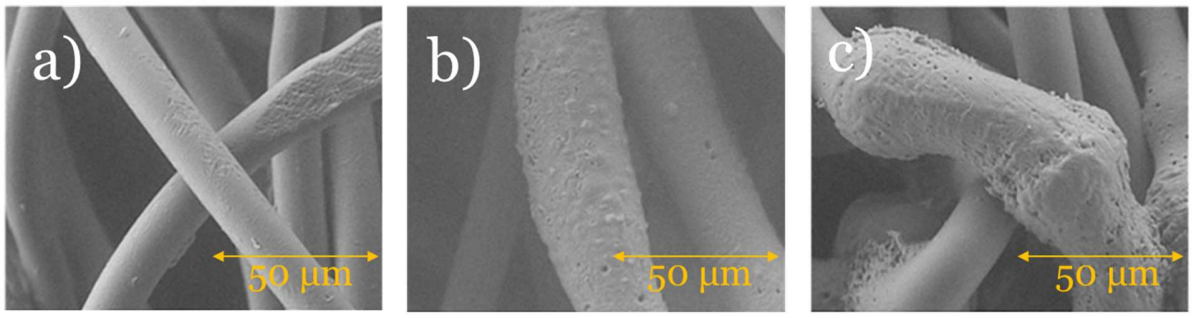

Figure 5.10: SEM Multifilament yarn, 5s in 130 °C EG. a) No slack b) 2 slack c) 2.5 slack

Shrinkage was calculated after treatment (10s in each bath) at various EG temperatures and slack values. As shown in Figure 5.11, yarns appear nearly stretched on the U-bar after treatment in EG at 126 °C for multifilament yarns, with shrinkage nearly matching the slack. Above this temperature, tension either inhibits further shrinkage when there is no additional length, or the yarn breaks.

The graph provides a first indication of the surface treatment mechanism: at temperatures insufficient to lead to surface treatment (e.g., 120 °C data points), the yarn primarily shrinks axially, leading to radial enlargement. This axial shrinkage is consistent across each mesoscopic section of the yarn, and increasing slack does not affect the shrinkage value, resulting in a constant shrinkage ratio at 120 °C. For higher temperatures, such as 125 °C or 126 °C, increasing slack correlates with increased shrinkage. This is due to additional chain movements contributing to shrinkage, specifically the development of surface roughness, which grows with the extra material provided. For these temperatures, the shrinkage behavior appears to follow a roughly linear trend.

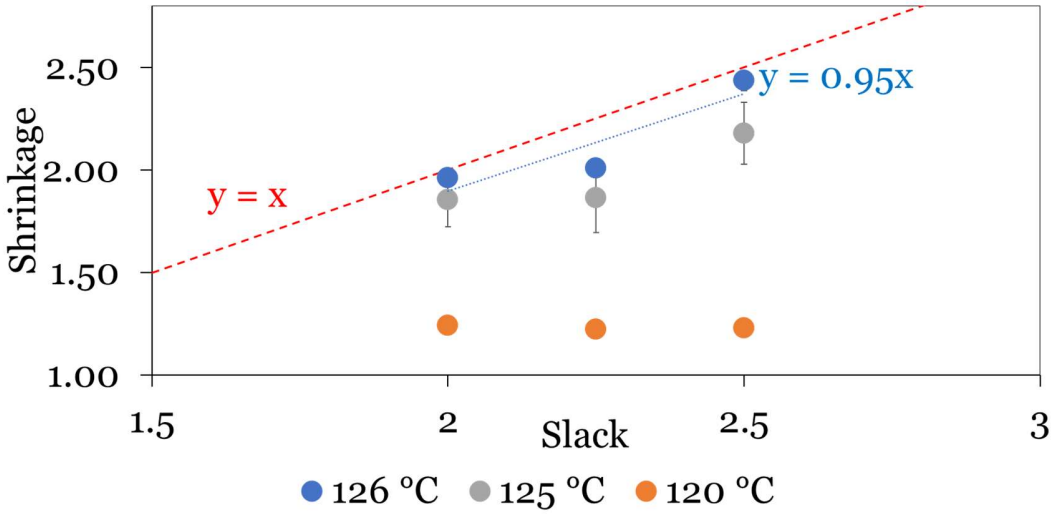

Figure 5.11: Shrinkage as a function of slack for different EG temperatures, multifilament PLA

Overall, uncertainties in shrinkage measurements and potential interactions between filaments could impact the results. Therefore, shrinkage characterization as a function of slack was also conducted using monofilament yarns.

Monofilament yarns

The previous conclusions were confirmed by repeating tests with monofilament yarns. The monofilament yarns have a larger diameter than the multifilament yarns and are significantly thicker than the individual filaments in the multifilament yarns. The critical temperature for the onset of treatment was higher for the monofilament compared to the multifilament systems. This difference is likely due to the heated liquid diffusing more effectively between the smaller filaments of the multifilament, resulting in greater swelling compared to a single, larger monofilament. Aside from this variation, the same conclusions were drawn. Below a critical temperature (e.g., 130 °C in the case of monofilament yarns), slack remains constant (Figure 5.12), and no surface treatment is observed in SEM images (Figure 5.13). At higher temperatures (e.g., 140 °C), shrinkage is linearly dependent on slack, with increased slack leading to greater surface roughness (Figure 5.12 and 5.14). In Figure 5.14.a, an initial layer of surface texturing with a flower petal-like morphology is present and more clearly visible in images given in Appendix C. Figure 5.14.b shows nucleation

of an additional surface layer, which in Figure 5.14.c, becomes complete, significantly enhancing roughness and increasing porosity between the flower-like structures.

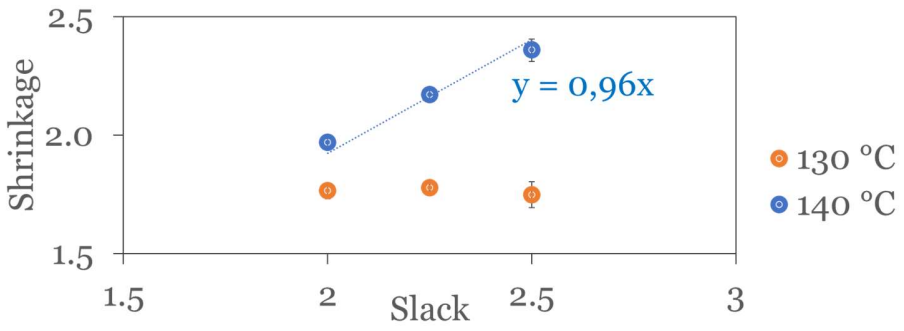

Figure 5.12: Shrinkage as a function of slack for different EG temperatures, monofilament PLA

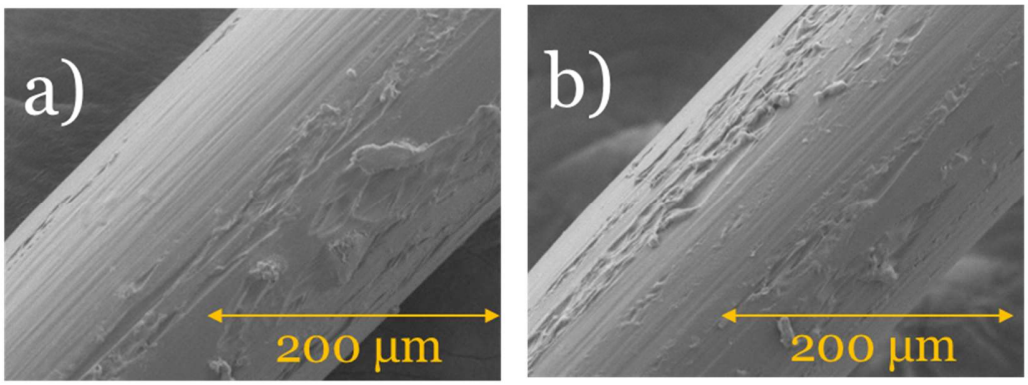

Figure 5.13: SEM Monofilament yarn, 10s in 130 °C EG. a) 2 slack b) 2.5 slack

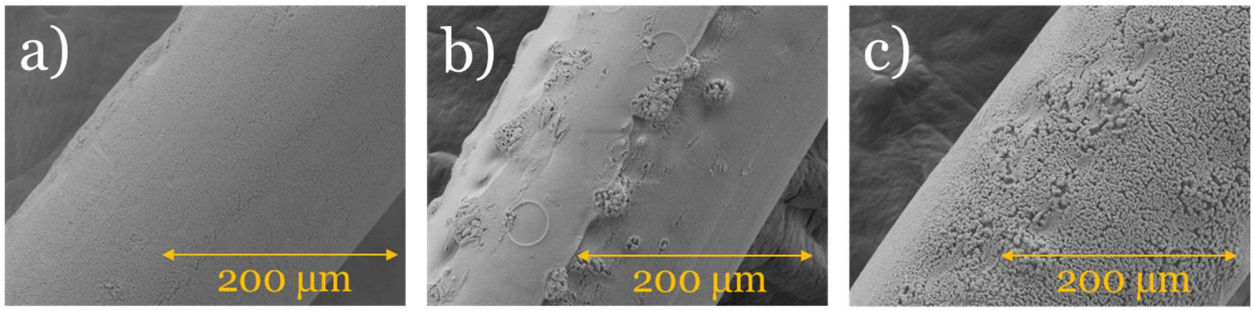

Figure 5.14: SEM Monofilament yarn, 10s in 140 °C EG. a) 2 slack b) 2.25 slack c) 2.5 slack

The mechanical properties of the treated yarns were assessed and compared to untreated yarns using a dynamometer. As seen in Figure 5.15, it seems that untreated yarns and yarns treated under slack value of 1 have similar mechanical properties. No significant differences in mechanical properties were observed among yarns treated with slack ratios of 2, 2.25, and 2.5. A slight decrease in the maximum force at break was noted for yarns treated with slack compared to those treated under tension. This aligns with the findings discussed in the literature review, where mechanical properties are influenced by the orientation of crystalline and amorphous zones, which are disrupted when the yarn is treated under slack. Overall, the mechanical properties are not drastically compromised due to surface recrystallization, which helps maintain the high mechanical performance of the treated yarns.

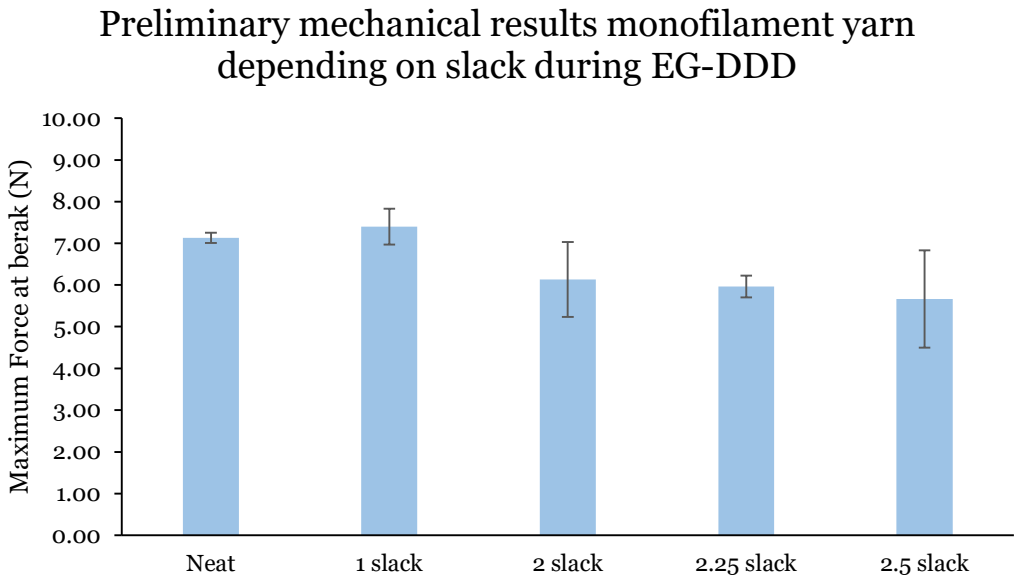

Figure 5.15: Preliminary mechanical properties of EG DDD-treated monofilament yarn for different slack

Finally, the cross-section was studied by microtoming DDD-treated yarn to study the depth of penetration and yarn diameter as a function of slack (Figure 5.16). There is a net increase in yarn diameter as a function of slack. From the preliminary study in Figure 5.16, it seems that above slack values of 2, increasing slack does not increase penetration depth.

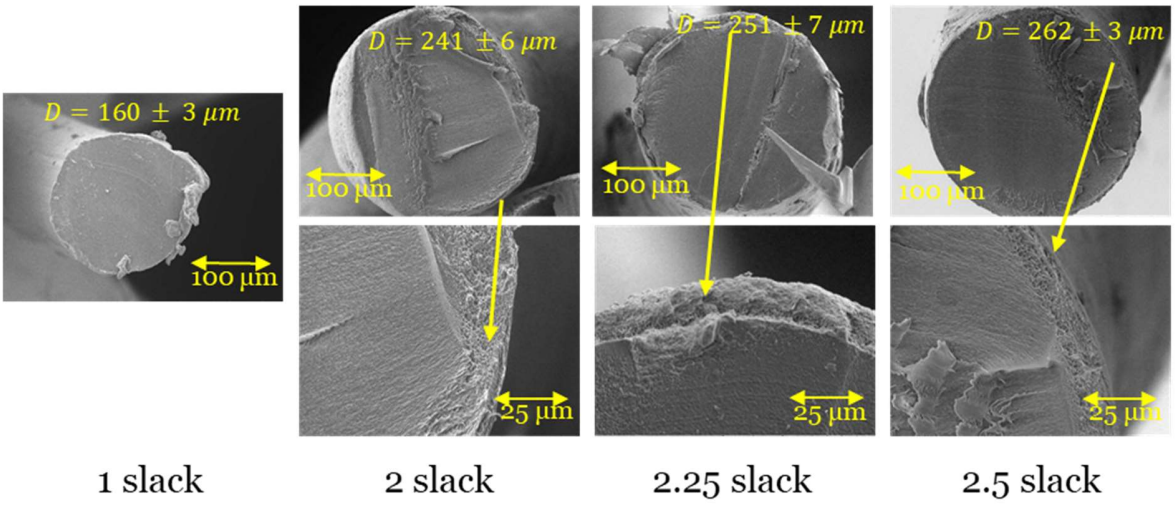

Figure 5.16: Images of microtomed yarns as a function of slack to get final yarn diameter D and penetration depth of treatment as a function of slack

Consequently, the final diameter of the yarn was also studied and compared to a traditional mass balance. A simple model consists of calculating the final diameter of a cylindrical yarn based on initial length, initial diameter, and final length under the hypothesis of neglecting porosity and density changes. As such, the final diameter should obey the following equation:

$$D_{f,th} = \sqrt{s * {D_i}^2} \tag{5.3}$$

s being the shrinkage (ratio of initial length compared to final length), $D_{f,th}$ the final theoretical diameter and D_i the initial diameter of 0.16 µm.

As seen in Figure 5.17, the gap between reality and the simple model is due to porosity and seems to be conserved between the different amount of slack as seen in the model taking into account mass conservation and porosity increase which fits very well the experimental increase in diameter during treatment when slack is increased. The simple model considers the initial diameter D_i as the diameter of the untreated yarn, while the model accounting for porosity is obtained by applying Equation (5.3) with an initial diameter D_i equal to the average diameter measured after treatment with a slack value of 2. This conclusion also fits the results regarding penetration depth, which is

also the depth in which porosity is created. This means that there is no significant increase in porosity above slack value of 2.

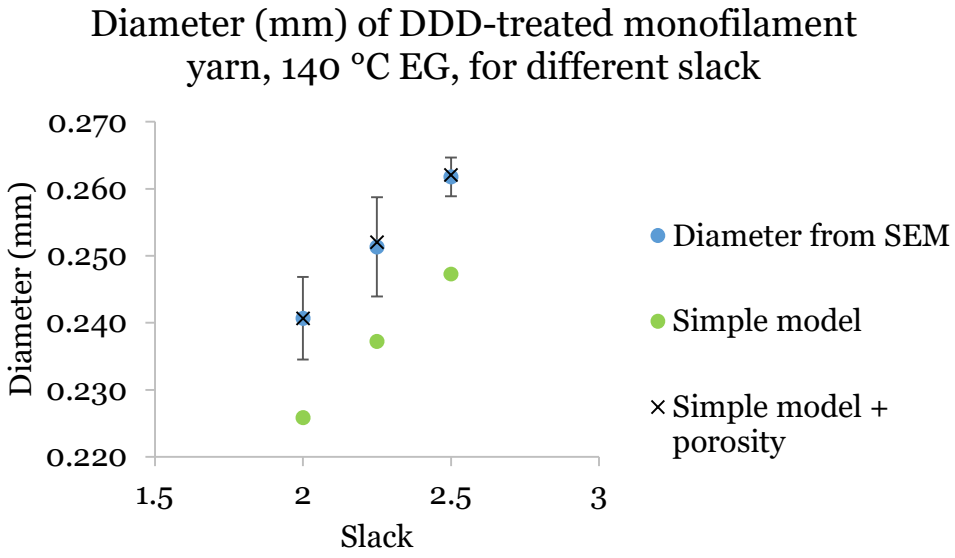

Figure 5.17: Diameter of DDD-treated monofilament yarn, 140 °C EG, 10s in each bath, with different amounts of slack comparing results from SEM and simple model

The wettability of treated yarns as a function of slack was also investigated. However, as mentioned in the literature review, it is very difficult to investigate wettability for fibers near and below 200 µm in diameter without specific force tensiometers. Using the Wilhelmy method and relying solely on visual inspection, the advancing contact angle could not be obtained. As the samples were hydrophobic, a liquid meniscus could not be properly seen due to diffraction. A review of these tests is presented in Appendix D. The only test that provided qualitative information on treated yarn wettability was fixing multifilament yarns in parallel, spaced 1 mm from one another. These yarns were stuck onto a glass plate as shown in Figure 5.18 below, with a slack value of 2. For untreated yarns and those treated at 120 °C, the yarns were not sufficiently hydrophobic to repel droplets, leading to spreading on the glass sheet. For higher temperatures of EG preheating, hydrophobic forces were sufficient to repel water and prevent spreading on the glass sheet. A water-yarn contact angle could be extracted to qualitatively compare the treated yarns at 125 and 130 °C

EG temperature. As seen in Figure 5.18, overhydrophobicity was achieved in both cases with increasing repellency with EG temperature.

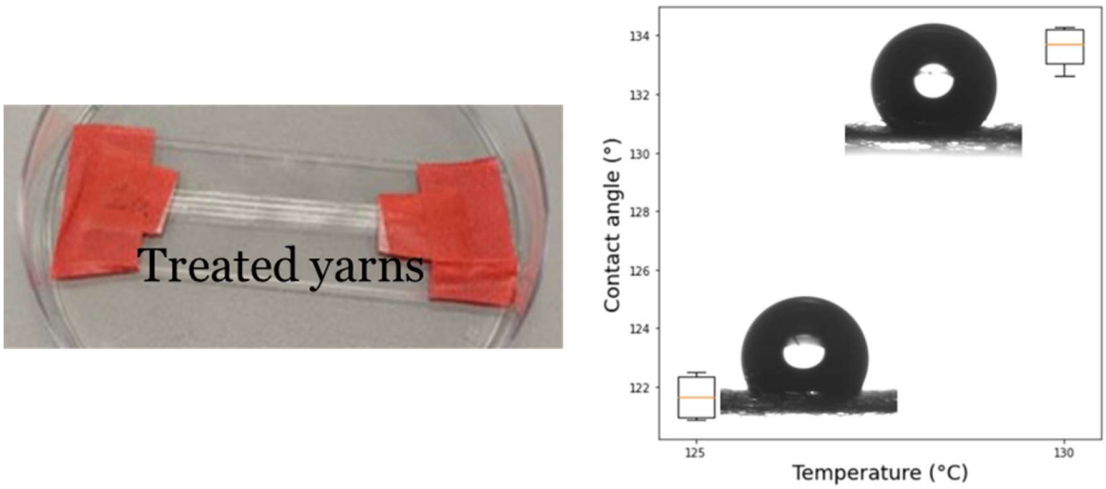

Figure 5.18: Qualitative wettability assessment of parallel fibers spaced 1 mm apart, treated at different ethylene glycol (EG) temperatures: 125°C and 130°C

5.2.3 From U-bar process to continuous operation

Based on the U-bar results, a slack value of 2 was selected due to observable surface recrystallization, wettability properties and reduced material loss, with lower shrinkage compared to 2.25 and 2.5 slack. These parameters were implemented in a continuous setup using multifilament PLA yarns, which aligns with the industrial partner's interests.

For a given slack, final morphology obtained with the setup might be different than the one obtained with the U-bar process. As shown in Figure 5.19, some differences can be seen from presence of tension during drawing process in the continuous setup. The amount of yarn given inside the EG bath was selected using the unwinding motor at different speeds: 48%, 67%, 76%, and 100% of the regulator, with the winding motor fixed at 38%. Slack conserves its meaning but equation (5.1) needs to be adapted to equation (5.4) to fit continuous operation parameters:

$$Slack = \frac{Speed\ unwinding\ spool\ (entry)}{Speed\ winding\ spool\ (exit)} \tag{5.4}$$

Subsequently, the unwinding speeds mentioned above correspond respectively to slack values of 1.25, 1.75, 2, and 2.63.

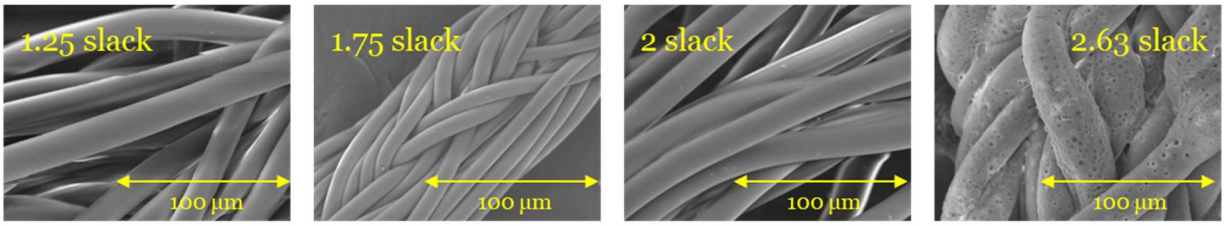

Figure 5.19: SEM images of EG DDD-treated multifilament yarn with 10s in 130°C EG, 10s acetone, 10s in water, and a winding speed with regulator at 38%. Tests were done for multiple values of slack: 1.25, 1.75, 2, and 2.63.

As shown in Figure 5.19, a slack value of 2 is not sufficient in the continuous setup as very little zones were modified (one zone on every repetition of the 0.8 cm - SEM samples). As can be seen in Figure 5.20, tension was both inhibiting treatment on majority of filaments and was sufficiently high to break the weakened treated zone. The point introduced earlier regarding instantaneous tension caused by friction on rolling elements introducing resistance to movement is also applicable in this case.

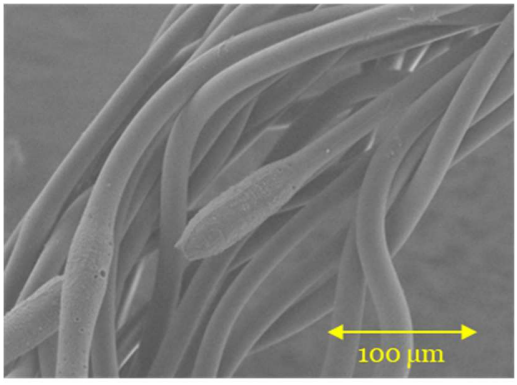

Figure 5.20: Illustration of a rupture in a DDD-treated zone on samples treated with the continuous setup with a slack value of 2

The setup was successfully operated once over 1h30 and without accumulation of yarn, even while raising the speed of the unwinding spool from 38% to 100% of the regulator (approximate feed

rates of 0.7 cm/s and 1.9 cm/s, respectively). The speed of the winding spool was kept constant with a regulator percentage set at 38%. The shrinkage of the yarn in EG to the exact amount given (the slack) allows no accumulation of yarn in the setup and as such continuous operation. Nevertheless, as the yarn is more fragile at some points (after being heated up or after partial dissolution in acetone), breakage can occur. Causes of breakage in the setup need to be addressed and will be discussed in more detail in Chapter 6.

CHAPTER 6 DISCUSSION

6.1 Potential upscaling issues

6.1.1 Maintaining hydrophobicity under exposure to different wavelengths

Effect of solar exposure on textured PLA wettability

As shown in Chapter 4, a 2h UVC exposure switches the wettability of the surface to capillary wicking. The energetic dose corresponding to 2h UVC low-pressure Hg discharge lamp at 3.5 cm under the lamp is 62.6 J/cm². Given that UVC affects the substrate, it became pertinent to test the durability of the treated surface when exposed to UVA and UVB from the sun, using a solar simulator. Exposing untreated and DDD-treated PLA substrates to the same energetic dose ($62.6\, J.cm^{-2}$) produced no change with the solar simulator (Figure 6.1).

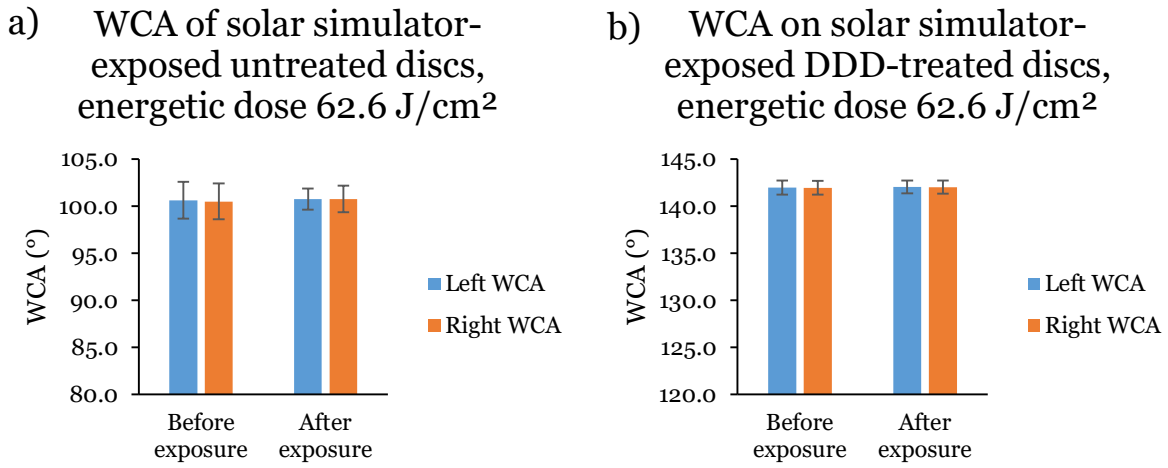

Figure 6.1: Water contact angle (WCA) before and after exposure to solar simulator on a) untreated and b) DDD-treated discs

This highlights a potential specific effect of UVC compared to UVA and UVB. Nevertheless, the viability of the treated nets under outdoor conditions was still data of interest. As such, tests were repeated, and exposure time was increased. The results below demonstrate the viability of the DDD-treated surfaces in the field, as hydrophobicity was maintained for the equivalent (eq) energetic dose from May to August, based on Mont Saint-Bruno data (the location of our field-testing laboratory partner IRDA, 45°32'37.2"N 73°20'28.5"W). A slight drop in wettability can be

seen over time. Out of a total of 9 measurements (3 measurements/disc on 3 different discs), the average contact angle of DDD-treated surfaces reduced from 142.9±2.3° to 136.6 ±1.2° whereas the average contact angle of untreated substrates reduced from 94.4±3.3° to 88.5±4.4°. In both cases, the average contact angle drop from May to August equivalent solar exposure represents approximately 6° (Figure 6.2).

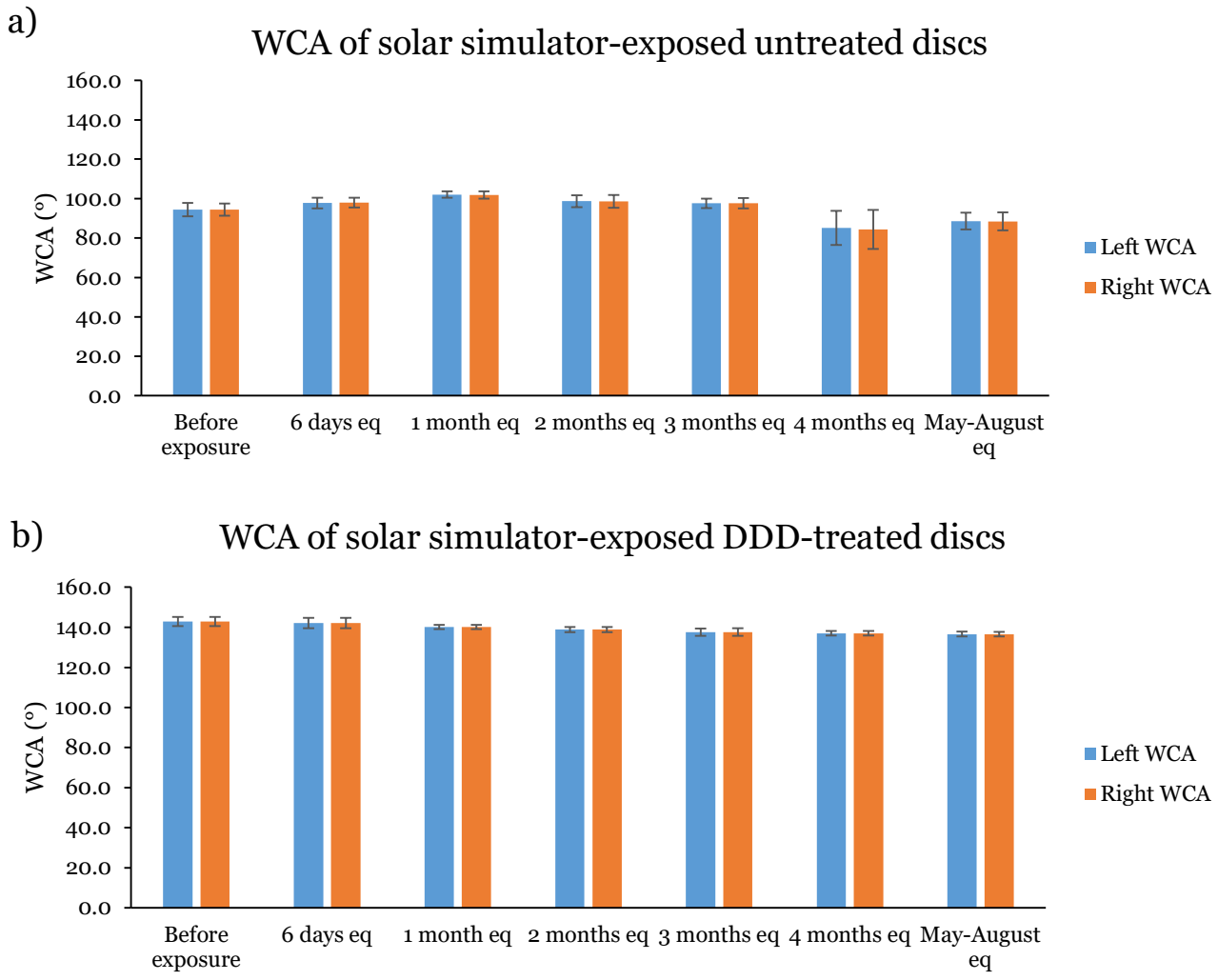

Figure 6.2: Water contact angle (WCA) before and after exposure to solar simulator on a) untreated and b) DDD-treated discs. Exposure time was set to reach May-August equivalent energetic dose.

Distinction between 4 months and May-August period is specified in Appendix E alongside details of calculation of the equivalent time between solar simulator and outside exposure.

For each time of exposure, the masses of the untreated and DDD-treated samples were recorded. The results suggest no or very low mass change (Figure 6.3), which correlates well to the limited change in contact angle and minor photodegradation during the summer period.

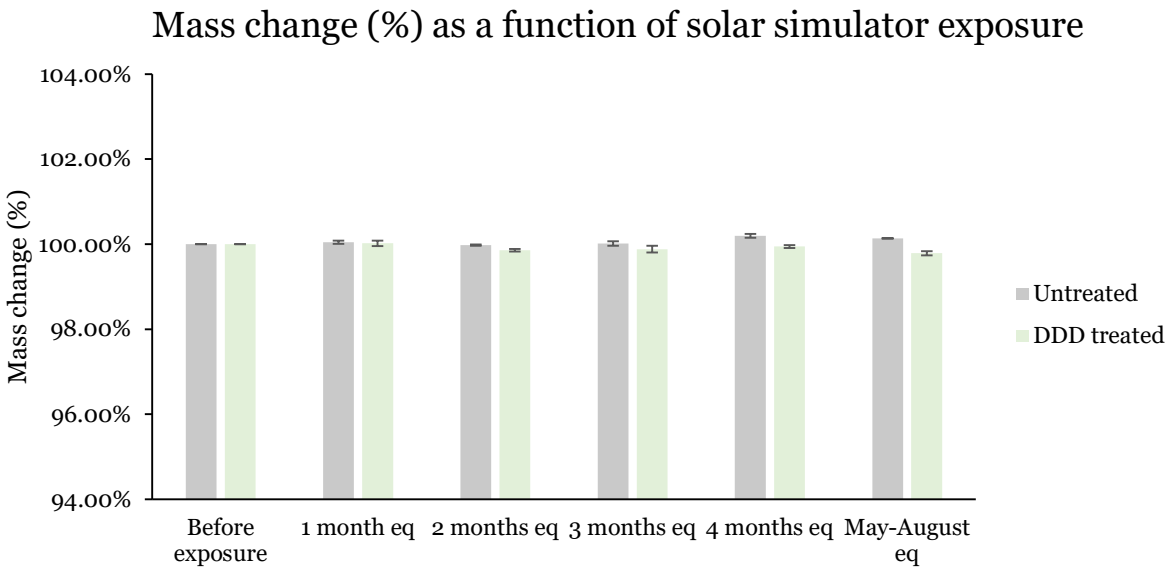

Figure 6.3: Mass change (%) as a function of solar simulator exposure for untreated and DDD-treated PLA discs

Specific effect of UVC Mercury Lamp

The same experiment was done with UVC LEDs with a principal emission peak at 275 nm (distribution 260-290 nm from the manufacturer's data). These results also indicate no drop in wettability, as seen in Figure 6.4. Nevertheless, possible LED photo-polymerization may have occurred as the contact angle slightly increases after 20h exposure (though error bars overlap).

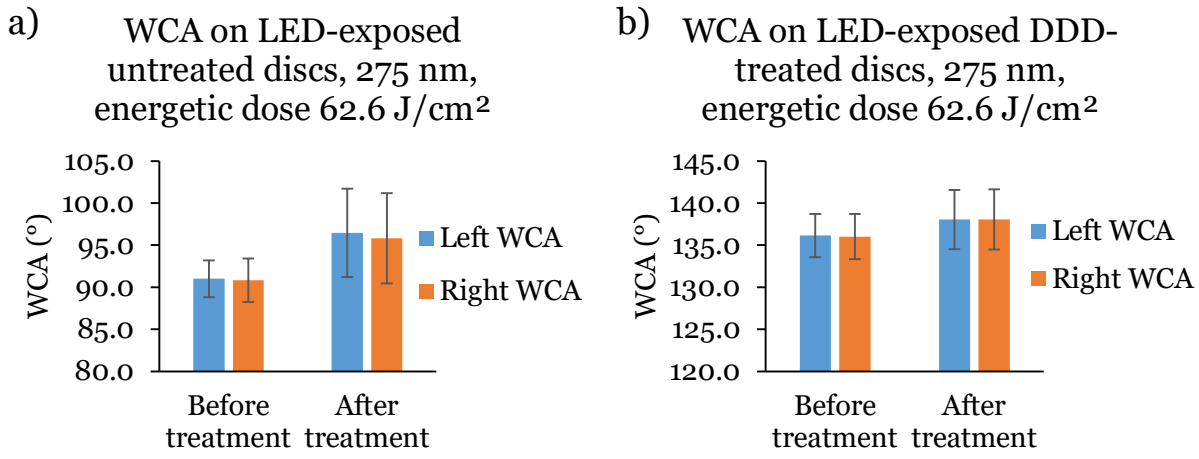

Figure 6.4: Water contact angle (WCA) before and after exposure to LED 275nm on a) untreated and b) DDD-treated discs

Subsequently, work on figuring out which wavelengths cause the switch in wettability is pursued with tests to filter out and distinguish the effect of both wavelength (184.9 nm and 253.7 nm) from the UVC lamp. It has to be said that depending on the glass material covering the UV discharge tubes, the vacuum ultraviolet (VUV) wavelengths - from 100 to 200 nm - are already cut. This comes from transmission spectrum having a cut-off at low wavelength. Borosilicate or quartz tend to be used as glass for UVC Mercury lamps, whose adsorption spectrum tends to present a natural barrier to transmitting VUV. Depending on impurities, thickness and glass formulation, the transmission spectrum could be affected. Ozone was detected after lamp usage for a prolonged period of time, which is considered an indicator of the presence of the 184.9 nm wavelength. Methods to detect the presence of VUV wavelengths use expensive tools such as diamond sensors or specific spectrometers. As such, another approach was used.

A common method to distinguish the effect of both wavelengths is preventing one wavelength from reaching the sample. This can be done using a filter. However, no commercially available filter was found to prevent 184.9 nm from reaching sample while not interrupting 253.7 nm wavelengths. Natural filters were then tested. The idea was to use materials with appropriate transmittance spectrum to erase or attenuate the signal from one of the two wavelengths. Pyrex® is sometimes used to block 184.9 nm but using ILT radiometer, it has also been shown to block 253.7 nm. In

Dever et al. article [192], it has been shown FEP (Fluorinated Ethylene Propylene) films of greater thickness than 127 microns could block the 184 nm while only attenuating from 50% the 250 nm wavelength. UV-Vis spectrum of 150 µm FEP films is presented below (Figure 6.5) and presents the opposite conclusion. Accumulating one to three layers of 150 µm did not change the transmittance spectrum, where the 250 nm was largely attenuated compared to the lower wavelengths. Main difference in the measurement is deemed to come from crystallinity differences. Dever et al. did not specify the crystallinity of the material used whereas amorphous FEP films were used in this study.

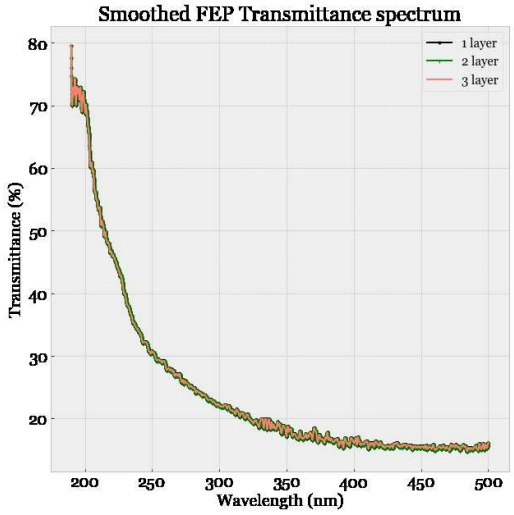

Figure 6.5: FEP transmittance spectrum from UV-Vis spectroscopy

Scanning the VUV wavelengths in UV-Vis is as difficult or expensive as detecting them. As one does not know the percentage of attenuation for the 184.9 nm wavelength it is difficult to conclude on the role of the wavelength based on wettability test results from FEP-covered and uncovered PLA discs. Explanation was taken from literature where Suzuki et al. [163] described that ozone was produced when oxygen molecules absorb 185 nm radiation. Then, the 254 nm radiation decomposes the ozone to form atomic oxygen which can react with the surface and lead to oxidation or orientation of polar ponds.

To add additional information to the effect of UVC Mercury on untreated PLA,UVC exposure has an effect on wettability after a considerable time of exposure. In our case a 54° drop in the contact

angle of untreated PLA was seen after 20h (Figure 6.6). Roughness and surface recrystallization is deemed to accelerate this effect as UVC breaks crystals into smaller crystals by chain scission mechanisms.

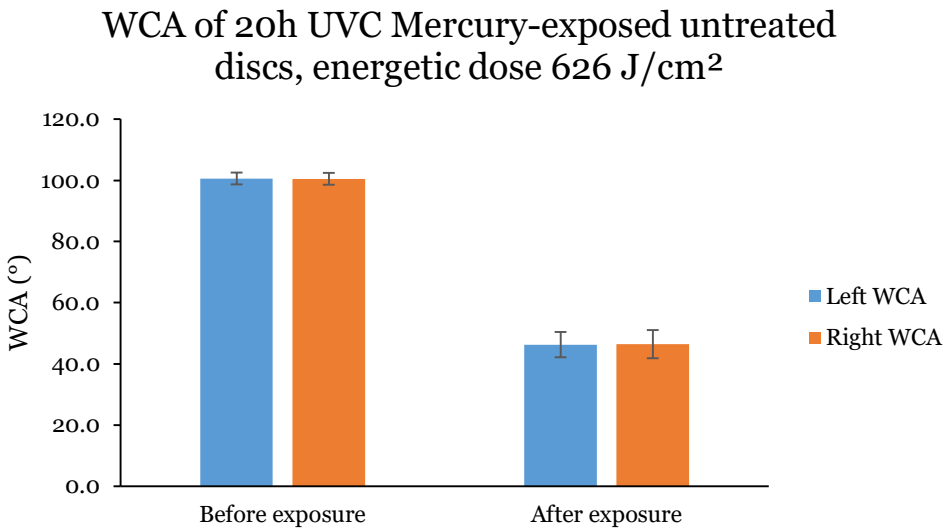

Figure 6.6: Water contact angle (WCA) on untreated discs before and after 20h exposure to UVC Mercury lamp

6.1.2 Mechanical properties after exposure to the solar simulator

After UVC exposure, DDD-treated PLA meshes became fragile, likely due to chain scission on the treated net surface, making them prone to breakage even with light handling. While this enhances compostability, caution is needed regarding the impact of sun exposure on the nets' mechanical properties. Consequently, mechanical tests were conducted on DDD-treated nets exposed to an equivalent May-August solar energy dose, as well as on unexposed DDD-treated samples (Figure 6.7). Since the unexposed samples came from the same batch as the exposed ones, they were 4 months old at the time of testing. To account for potential ageing effects, freshly DDD-treated samples (1 week old) were also tested.

Error bars were high due to the limited number of samples available for testing. Overall, mechanical properties appeared to be largely conserved, with a slight (but not statistically significant) potential decrease observed in the 4-month-old, solar simulator-exposed DDD-treated

nets, possibly due to photodegradation, ageing, test variability, or non-uniformity in treatment among samples and batches.

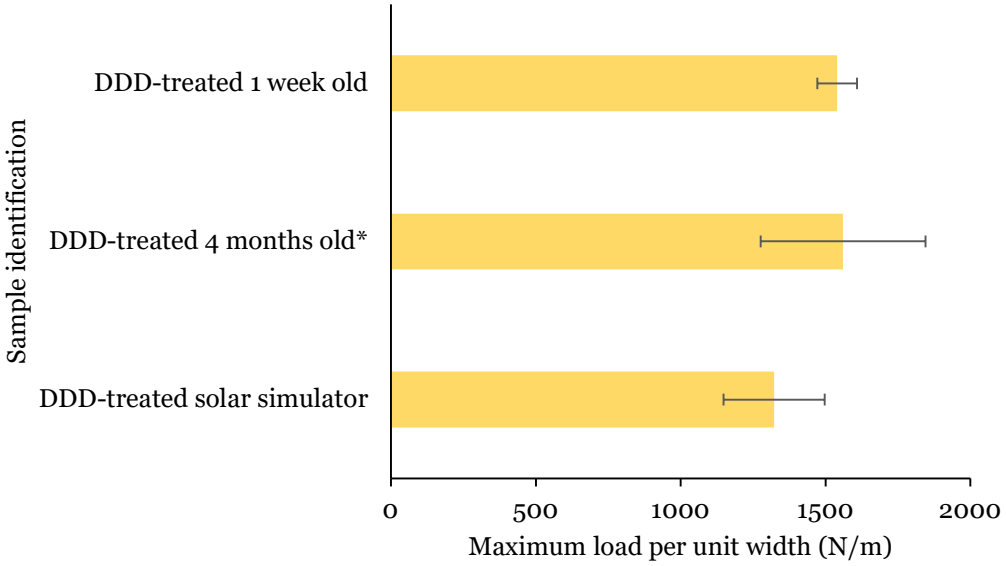

Figure 6.7: Mechanical testing of unexposed and solar simulator exposed DDD-treated nets

*Nets from the same batch of the ones that went in the solar simulator. Every rupture test was considered.

6.1.3 Nets viability

From previous sections, it can be said that overall, there are minor differences in wettability and mechanical properties for nets with an exposure equivalent to May-August energetic dose and unexposed nets.

Notwithstanding, from a toxicology perspective, biodegradation assays would be pertinent, especially in regard to recent controversial conclusions in the literature, whereby the toxicological profiles of petroleum and biobased plastics did not show significant differences [132, 193]. The similarity in toxicological impact comes from the additives used in a polymer product (polymerization catalysts, plasticizers, antioxidants, antistatic agents, processing agents, lubricants, colorants, flame retardants, etc.). As introduced in Chapter 1, additives can be significantly more

noxious than the product or polymer itself. As additives change from one formulation to another, some have reported no difference in soil micro-organisms activity before and after the degradation of bioplastics such as PLA, poly (butylene succinate) (PBS) and PBS-starch [194]. However, in the same study, it was also reported that a change in micro-organism diversity might occur as fungal and bacterial biomass have seen some slight variation over a 28-day period. Results were completed with a 2-year biodegradation study where overall soil bacterial biomass and diversity were not influenced by the degradation of the bioplastics studied, which is an encouraging result regarding the upscaling and increasing use of PLA.

6.2 Towards the industrial scale

6.2.1 Preventing breakages in continuous processing

As introduced in Chapter 5, yarns might undergo rupture during treatment if the temperature of the EG is too high. At 128 °C and above, breakages were seen in the U-bar process using multifilament yarns. If yarns broke, two types of breakage appeared: breakage during shrinkage in the EG, or when withdrawing the yarns from the EG (likely due to surface tension effects and yarns weakening due to heating above the glass transition temperature). In the first case, a very simple model was created to lay the basis for the development of the theory regarding rupture.

Shrinkage has a speed V_r that depends on the temperature of the hot liquid it is put in. There is thus a kinetic energy E_k associated to the shrinkage, corresponding to a force that can potentially break the yarn. This appears if the kinetic energy is greater than the cohesive energy W, which is equal to 2 times the surface free energy γ. This comes from equation (2.24) $W_{ij} = \gamma_i + \gamma_j - \gamma_{ij}$ where the two phases represented by index i and j are the same ($\gamma_i = \gamma_j$ and $\gamma_{ij} = 0$ as there is no interface) [195]. Breakage criterion is then represented by equation (6.1).

$$E_k = \frac{1}{2}\rho S L_0 * {V_r}^2 > W = 2\gamma \tag{6.1}$$

The speed V_r of the shrinkage s verifies leads to equation (6.2), with L_0 being the initial length of the yarn.

$$V_r = \frac{Initial\ length - final\ length}{time} = \frac{L_0 - \frac{L_0}{S}}{t} = \frac{slack * LoT - \frac{slack * LoT}{S}}{t} \tag{6.2}$$

Subsequently, the criterion to predict breakage (maximum shrinkage) based on slack and time of shrinkage t can be plotted for a given U-bar (Figure 6.8). Simulations were done with monofilament yarns having a diameter of approximately 160 μm according to SEM measurement. As can be seen in Figure 6.8, for a shrinkage time near 0.001 s, rupture resulting simply from kinetic energy dissipation is possible. If the temperature increases, shrinkage time decreases, which will contribute to an increasing chance of rupture at lower shrinkage.

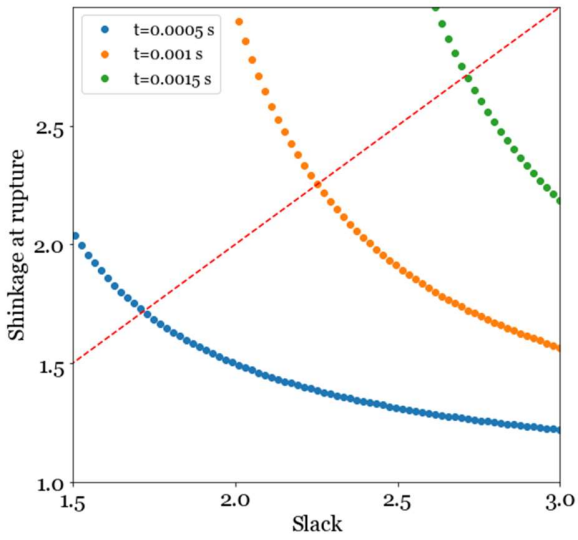

Figure 6.8: Shrinkage at rupture as a function of slack based on simple model for monofilament PLA for different shrinking time. Red dotted line represents the shrinkage = slack function.

Shrinkage time is dependent on temperature and could be quantified with a high-resolution camera. However, the purpose of this model was to understand one of the potential causes of breakage in the U-bar process. This model is oversimplified because it does not take into account the yarn tension, liquid viscosity or interfacial tension. Additionally, the change in diameter of the yarn during experiments is not considered in the model.

In the continuous setup, rupture can be more frequent as movement and friction contribute to increasing strain imposed on the yarn, and because higher EG temperatures are needed for treatment because of tension effects. Consequently, tight control of parameters (temperature, slack, shrinkage and tension) is even more important. Overall, this method is deemed to be the most promising method in regard to upscaling. Nevertheless, the final morphology of DDD-treated

multifilament yarns seems different: for a slack value of 2.63 (Figure 5.19), significantly more micropores were seen and no flower-like morphology was obtained compared to manual treatment. Roughness and wettability of the meshes formed with treated yarns using the continuous setup will need to be assessed before usage.

6.2.2 Treatment on meshes at larger scales

The most straightforward method for treating large nets would involve using large baths and substantial amounts of liquid. However, this approach presents several challenges, including ergonomics and practical implementation. Large tanks are not only costly but also make it difficult to achieve uniform temperatures throughout the ethylene glycol (EG) bath. For instance, to produce a 1 m × 1 m treated net, a bath of at least 4 m × 3 m would be required to account for shrinkage, necessitating an even larger EG bath. Shrinkage values for different sample shapes are presented in the table below.

Table 6.1: Shrinkage as a function of sample size and shape

Sample size (warp * weft)	**10 cm * 10 cm**	**10 cm * 20 cm**	**20 cm * 10 cm**
Shrinkage warp direction	3.78 (±0.29)	3.84 (±0.30)	4.15 (±0.37)
Shrinkage weft direction	2.30 (±0.14)	2.72 (±0.16)	2.62 (±0.16)

As shown in Table 6, shrinkage varies significantly between the weft and warp directions, which is critical as this directly affects mesh size: the holes in exclusion nets are specifically designed to block certain larger insects while allowing sufficient sunlight to pass through. In the order of magnitude, mesh sizes of 1.0×1.0 mm are used. Dimensions are adapted depending on the insects to exclude. For example, commercial nets found in Québec for berry crop protection against *D. suzukii* have a mesh size of 0.85×1.4 mm [27]. However, it is possible to start with nets that have larger mesh holes, allowing them to shrink to the desired size after treatment. Nevertheless, this is not always desirable in terms of production standards.

6.2.3 Other alternatives to upscale treatment

Other methods to upscale treatment were investigated. 3D printing of amorphous PLA nets is also possible. As shown by Knoch et al. [37], DDD texturation can be achieved using only acetone and water (standard DDD) on amorphous printed nets. This method is particularly advantageous for achieving precise mesh size control, but poses significant challenges when it comes to scaling up. Most 3D printers are designed to produce parts with a maximum width of around 30 cm, which is limited by the size of the printing platform. While length can be accommodated with dynamic platforms that enable continuous printing, larger widths require 3D printers with bigger platforms. Due to their high cost, these larger printers are typically reserved for advanced applications, such as in the aerospace industry.

CHAPTER 7 CONCLUSIONS AND RECOMMENDATIONS

7.1 Conclusions of the study

This project addresses the upscaling of hydrophobic treatment on polylactic acid (PLA) exclusion nets as an alternative to pesticides and fungicides in agriculture. Exclusion nets have proven highly effective in protecting crops from pests and maintaining high yields. However, most exclusion nets on the market are made of high-density polyethylene (HDPE), a petroleum-based plastic that often ends up in landfills due to a lack of recycling facilities. Consequently, there has been growing interest in developing biobased exclusion nets. Despite this, biobased plastics are not widely used in outdoor applications because they readily interact with water. Hydrophilicity can lead to direct degradation (e.g., hydrolysis) or indirect degradation when water adheres to the surface of compostable or biodegradable polymers, promoting bacterial growth. This is particularly true for PLA, an industrially compostable polymer that degrades under the action of microorganisms such as bacteria and fungi. Therefore, water remaining on the nets can be detrimental not only to the nets themselves but also to crops, as water on fruits and leaves can promote the growth of molds and diseases. Additionally, the weight of wetted nets could potentially hinder plant growth, as the increased weight would be transferred to the plants if no net support infrastructure is in place.

Surface treatment techniques have been developed to tailor surface wettability. Our lab developed a two-step process called Dip-Dip-Dry (DDD) to render PLA hydrophobic. This treatment is based on solvent-induced crystallization, where PLA is dipped into a solvent bath to induce swelling and free some polymer chains, which subsequently shrivel when immersed in a coagulant bath. After drying, the resulting rough surface imparts hydrophobic and water-repellent properties. However, modifying the interaction between the nets and water to prevent stagnation on nets or leaves may alter net compostability, as water no longer serves as a growth medium for microorganisms during the initial stages of decomposition. Additionally, the DDD treatment leads to recrystallization at the surface, and it is known that crystalline materials degrade more slowly than their amorphous counterparts.

This research demonstrated that the wettability of a solvent-treated hydrophobic PLA substrate could be fully reverted to capillary-wicking through a single 2-hour UVC exposure using a low-

pressure mercury discharge lamp. The effect of UVC exposure was particularly pronounced on DDD-treated PLA. Mechanisms were studied in detail. As shown by gel permeation chromatography (GPC), UVC irradiation induced polymer chain scission, reducing the average molecular weight by half. This permanent change was further evidenced by the consistent wicking behavior observed one-year post-exposure. Chain scission also affected other properties, including a decrease in degradation temperature (TGA), a lower melting point, and increased recrystallization (DSC). Although no significant chemical composition changes were detected at the surface by FTIR and XPS, a minor increase in carbonyl groups suggested slight oxidation following chain scission. With no changes in crystallinity (XRD) or fine morphology (SEM), this minor oxidation is the primary explanation for the observed hydrophilicity. Hence the potential issues of composting related to the hydrophobicity of treated PLA nets post-use have been resolved, thus allowing upscaling work to extend to PLA yarns and meshes.

During the upscaling of the treatment on yarn, it was found that restricting chain mobility by applying tension prevented the formation of surface texture due to polymer chain stretching and alignment. Since the treatment relies on crystallization, chain mobility is essential for developing surface roughness. Various strategies were explored to increase mobility. Raising the treatment temperature was ineffective for yarn, often leading to increased breakage and failed treatments in continuous roll-to-roll processes. To enhance chain mobility and reduce tension significantly, slack was introduced into the setup, enabling the polymer chains to move and reorganize, as observed through yarn shrinkage. The treatment was found to be influenced by both temperature and extra length given: below a critical temperature, no treatment occurred, and shrinkage was independent of the additional length; above this threshold, shrinkage increased linearly, correlating with improved surface treatment. This critical temperature lies between PLA recrystallization and melting temperature. Mechanical and wettability properties of treated yarns were investigated as a function of slack, with guidelines for upscaling outlined in the conclusion. Other ways to upscale treatment were discussed such as direct treatment on meshes, 3D printing and using a coating containing treated PLA powder.

7.2 Main discoveries

The major highlights of this work are, first, the practical link between hydrophobic treatment based on recrystallization and chain mobility, demonstrating that quantifying slack yields valuable insights without significantly compromising mechanical properties. Secondly, the considerable wettability switch occurring when exposing overhydrophobic textured PLA to UVC for a short time (2h) holds a different mechanism based on chain scission and reorientation of polar bonds to the surface.

7.3 Recommendations for future work

A degradation study would have been relevant and will be the focus of future work in this broader project on biobased, compostable exclusion nets. This research will aim to ensure that composting PLA exclusion nets has a minimal toxicological impact, especially considering that additives in the plastic can significantly affect soil quality. Furthermore, PLA is industrially-compostable, and some enzymes can be added to make it domestically compostable [196]. However, enzymes can be expensive. With the use of UV pretreatment, mechanical properties are significantly reduced; thus, the mesh can be fragmented more easily, which might help to increase PLA compostability.

Finally, variations of the DDD treatment can be used for specific purposes such as preventing solvent evaporation to the atmosphere or using natural solvents. First instead of using volatile liquid such as acetone bath, near which the concentration will have to be compared to the tolerated values of exposure regarding health safety, solvent vapor can be used and cycled in a closed setup. This would also prevent air pollution. For replacement of acetone, other solvents can also be used with specific characteristics such as greater vapor pressure to limit evaporation or using natural solvents such as natural deep eutectic solvents (NADES), which have already been successfully used in literature to increase hydrophobicity and increase dying ability of PLA fabric [197]. Similarly, ionic liquids can also be investigated as potential solvents.

In the case of EG, to prevent its evaporation caused by heating, it would be possible to change the mechanisms of freeing chains at the surface. For example, as seen in the introduction with mercerization some surface treatments might allow to slightly depolymerize the surface, which would make it easier for acetone to diffuse throughout all PLA surface and recrystallized when

dipped in a nonsolvent. Alternatively, to avoid modifying the net, which has been shown to have specific requirements such as mesh size control, a coating containing superhydrophobic particles can be used. For example, one can create hydrophobic particles by using DDD treatment on PLA powder and then use this powder on a coating that would be sprayed on the material.

REFERENCES

1. Grocholl, L. *Pesticides History and Food Safety*. MilliporeSigma, Sigma-Aldrich; Available from: https://www.sigmaaldrich.com/CA/en/technical-documents/technical-article/food-and-beverage-testing-and-manufacturing/flavor-and-fragrance-formulation/pesticides-and-residuals-history-and-food-safety.
2. *The Evolution of Chemical Pesticides*. Lab Reporter 2016; Available from: https://www.fishersci.ca/ca/en/publications/lab-reporter/2016/issue-4/the-evolution-chemical-pesticides.html.
3. Zeidler, O., *I. Verbindungen von Chloral mit Brom- und Chlorbenzol.* Berichte der Deutschen Chemischen Gesellschaft, 1874. **7**: p. 1180-1181.
4. Li, B.A., *Dichloro-Diphenyl-Trichloroethane (DDT): An Unforgettable and Powerful Pesticide.* Journal of High School Science, 2022. **6**(2).
5. Reddy, B.S. and P.K. Dubey, *The Rise, Fall and Re-emergence of DDT.* Resonance-Journal of Science Education, 2023. **28**(8): p. 1233-1243.
6. Carson, *Silent Spring*. 1962: Houghton Mifflin.
7. Kolaja, G.J. and D.E. Hinton, *Effects of Ddt on Eggshell Quality and Calcium Adenosine-Triphosphatase.* Journal of Toxicology and Environmental Health, 1977. **3**(4): p. 699-704.
8. *Osprey, Pandion haliaetus*. Available from: https://www.nj.gov/dep/fgw/ensp/pdf/end-thrtened/osprey.pdf.
9. *Alternatives to DDT*. Pollution and Health [cited 2024; Available from: https://www.unep.org/topics/chemicals-and-pollution-action/pollution-and-health/persistent-organic-pollutants-pops-0.
10. Langlois, V. *Vers une diminution majeure des pesticides au Canada?* in *3rd RQRAD Congress*. 2024. Centre des congrès de Québec.
11. Kaur, R., et al., *Pesticides: An alarming detrimental to health and environment.* Science of the Total Environment, 2024. **915**.
12. Gautam, R., et al., *Assessing the impact and mechanisms of environmental pollutants (heavy metals and pesticides) on the male reproductive system: a comprehensive review.* Journal of Environmental Science and Health Part C-Toxicology and Carcinogenesis, 2024. **42**(2): p. 126-153.
13. Leblanc, J., *Agriculture: l'industrie, reine de nos champs?*, in *Agriculture, Sciences*. 2024, Québec Science: Québec Science.
14. Labrie, G., et al., *Impacts of neonicotinoid seed treatments on soil-dwelling pest populations and agronomic parameters in corn and soybean in Quebec (Canada).* Plos One, 2020. **15**(2).
15. Muniz-Junior, G., et al., *Are lower pesticide doses better? An evolutionary perspective on integrated pest management.* Ecological Modelling, 2023. **482**.

16. *FAO, FIDA, OMS, PAM et UNICEF. 2023. L'État de la sécurité alimentaire et de la nutrition dans le monde 2023. Urbanisation, transformation des systèmes agroalimentaires et accès à une alimentation saine le long du continuum rural-urbain. Rome, FAO.* .

17. Holt-Giménez, E., et al., *We Already Grow Enough Food for 10 Billion People ... and Still Can't End Hunger.* Journal of Sustainable Agriculture, 2012. **36**(6): p. 595-598.

18. Gustavsson, J., Cederberg, C., Sonesson, U., van Otterdijk, R., and Meybeck, A., *"Global food losses and food waste: Extent, causes and prevention"*, F.a.A.O.o.t.U.N. (FAO), Editor. 2011.

19. Sharma, A., et al., *Worldwide pesticide usage and its impacts on ecosystem.* Sn Applied Sciences, 2019. **1**(11).

20. Kakutani, K., et al., *An Electrostatic Pest Exclusion Strategy for Greenhouse Tomato Cultivation.* Horticulturae, 2022. **8**(6).

21. Guo, D.M., et al., *Plasma-activated water production and its application in agriculture.* Journal of the Science of Food and Agriculture, 2021. **101**(12): p. 4891-4899.

22. Rizvi, S.A.H., et al., *Latest Developments in Insect Sex Pheromone Research and Its Application in Agricultural Pest Management.* Insects, 2021. **12**(6).

23. Matsuda, Y., et al., *An oppositely charged insect exclusion screen with gap-free multiple electric fields.* Journal of Applied Physics, 2012. **112**(11).

24. Matsuda, Y., et al., *Avoidance of an electric field by insects: Fundamental biological phenomenon for an electrostatic pest-exclusion strategy.* Electrostatics 2015, 2015. **646**.

25. Ndey Bassin Jobe, A.C., Brian H. Smith, Elies Molins, , Andreas Rose, Theodore P. Pavlic, Krijn P. Paaijmans, *Using electric felds to control insects: current applications and future directions.* Journal of Insect Science, 2024. **24**(8): p. 1-9.

26. Klassen, D., et al., *Dispensers for pheromonal pest control.* Journal of Environmental Management, 2023. **325**.

27. Chouinard, G., et al., *Insect netting: effect of mesh size and shape on exclusion of some fruit pests and natural enemies under laboratory and orchard conditions (10.1007/s10340-022-01582-5, 2022).* Journal of Pest Science, 2023. **96**(2): p. 871-873.

28. Chouinard, G., et al., *Impact of exclusion netting row covers on arthropod presence and crop damage to 'Honeycrisp' apple trees in North America: A five-year study.* Crop Protection, 2017. **98**: p. 248-254.

29. Chouinard, G., et al., *Impact of Exclusion Netting Row Covers on 'Honeycrisp' Apple Trees Grown under Northeastern North American Conditions: Effects on Photosynthesis and Fruit Quality.* Insects, 2019. **10**(7).

30. Mikaël Larose, G.C., Francine Pelletier, Zachary Bélisle (IRDA). *Produire des pommes sans pesticides : Est-ce une utopie?* in *3rd RQRAD Congress RQRAD,*. 2024. Centre des congrès de Québec.

31. Bouvier, J.C., T. Boivin, and C. Lavigne, *Single-row exclusion nets: an alternative pest control method with no detectable impact on breeding bird assemblages in orchards bordered by hedgerows.* Agronomy for Sustainable Development, 2022. **42**(2).

32. Taylor, R.A.J., et al., *Economic evaluation of insect-proof screens for preventing tomato yellow leaf curl virus of tomatoes in Israel.* Crop Protection, 2001. **20**(7): p. 561-569.

33. Mukherjee, A., et al., *Use of bio-based polymers in agricultural exclusion nets: A perspective.* Biosystems Engineering, 2019. **180**: p. 121-145.

34. Pranamuda, H., Y. Tokiwa, and H. Tanaka, *Polylactide degradation by an Amycolatopsis sp.* Applied and Environmental Microbiology, 1997. **63**(4): p. 1637-1640.

35. Qi, X., Y.W. Ren, and X.Z. Wang, *New advances in the biodegradation of Poly(lactic) acid.* International Biodeterioration & Biodegradation, 2017. **117**: p. 215-223.

36. Karamanlioglu, M., R. Preziosi, and G.D. Robson, *Abiotic and biotic environmental degradation of the bioplastic polymer poly(lactic acid): A review.* Polymer Degradation and Stability, 2017. **137**: p. 122-130.

37. Knoch, S., et al., *Surface modification of PLA nets intended for agricultural applications.* Colloids and Surfaces a-Physicochemical and Engineering Aspects, 2020. **598**.

38. Emelyanenko, A.M., et al., *Harnessing Extreme Wettability: Combatting Spread of Bacterial Infections in Healthcare.* Surface Innovations, 2024.

39. Gottfried, B.S. and K.J. Bell, *Film Bioling of Spheroidal Droplets.* Industrial & Engineering Chemistry Fundamentals, 1966. **5**(4): p. 561-+.

40. Barthlott, W. and C. Neinhuis, *Purity of the sacred lotus, or escape from contamination in biological surfaces.* Planta, 1997. **202**(1): p. 1-8.

41. Bruel, C., et al., *Experimental methods in chemical engineering: Contact angles.* Canadian Journal of Chemical Engineering, 2019. **97**(4): p. 832-842.

42. Young, T., *An Essay on the Cohesion of Fluids.* Philosophical Transactions of the Royal Society of London , 1805, Vol. 95 (1805), pp. 65-87.

43. Fernandez-Toledano, J.C., et al., *On the cohesion of fluids and their adhesion to solids: Young's equation at the atomic scale.* Advances in Colloid and Interface Science, 2017. **245**: p. 102-107.

44. Adam, N.K., *Use of the Term Youngs Equation for Contact Angles.* Nature, 1957. **180**(4590): p. 809-810.

45. Flores-Vivian, I., et al., *Self-Assembling Particle-Siloxane Coatings for Superhydrophobic Concrete.* Acs Applied Materials & Interfaces, 2013. **5**(24): p. 13284-13294.

46. Quéré, D., *Wetting and roughness.* Annual Review of Materials Research, 2008. **38**: p. 71-99.

47. *Shafrin EG, Zisman WA. 1964. Upper limits to the contact angles of liquids on solids. In Contact Angle,*

Wettability and Adhesion: Advances in Chemistry Series, Vol. 43, ed. RF Gould, pp. 145–57. Washington,

DC: Am. Chem. Soc.

48. Shibuichi, S., et al., *Super water-repellent surfaces resulting from fractal structure.* Journal of Physical Chemistry, 1996. **100**(50): p. 19512-19517.

49. Wenzel, R.N., *Resistance of solid surfaces to wetting by water.* Industrial and Engineering Chemistry, 1936. **28**: p. 988-994.

50. Cassie, A.B.D. and S. Baxter, *Wettability of porous surfaces.* Transactions of the Faraday Society, 1944. **40**: p. 0546-0550.

51. Cassie, A.B.D., *Contact Angles.* Discussions of the Faraday Society, 1948. **3**: p. 11-16.

52. Deng, Y.Y., et al., *Recent development of super -wettable materials and their applications in oil -water separation.* Journal of Cleaner Production, 2020. **266**.

53. Bico, J., C. Marzolin, and D. Quéré, *Pearl drops.* Europhysics Letters, 1999. **47**(2): p. 220-226.

54. Bormashenko, E., *Progress in understanding wetting transitions on rough surfaces.* Advances in Colloid and Interface Science, 2015. **222**: p. 92-103.

55. Marmur, A., *Wetting on hydrophobic rough surfaces: To be heterogeneous or not to be?* Langmuir, 2003. **19**(20): p. 8343-8348.

56. Gao, L.C. and T.J. McCarthy, *Reply to "Comment on How Wenzel and Cassie Were Wrong by Gao and McCarthy".* Langmuir, 2007. **23**(26): p. 13243-13243.

57. Gao, L.C. and T.J. McCarthy, *How Wenzel and Cassie were wrong.* Langmuir, 2007. **23**(7): p. 3762-3765.

58. Panchagnula, M.V. and S. Vedantam, *Comment on how Wenzel and Cassie were wrong by Gao and McCarthy.* Langmuir, 2007. **23**(26): p. 13242-13242.

59. McHale, G., *Cassie and Wenzel: Were they really so wrong?* Langmuir, 2007. **23**(15): p. 8200-8205.

60. Shardt, N. and J.A.W. Elliott, *Gibbsian Thermodynamics of Wenzel Wetting (Was Wenzel Wrong? Revisited).* Langmuir, 2020. **36**(1): p. 435-446.

61. Shardt, N. and J.A.W. Elliott, *Gibbsian Thermodynamics of Cassie-Baxter Wetting (Were Cassie and Baxter Wrong? Revisited).* Langmuir, 2018. **34**(40): p. 12191-12198.

62. Good, R.J. and M.N. Koo, *Effect of Drop Size on Contact-Angle.* Journal of Colloid and Interface Science, 1979. **71**(2): p. 283-292.

63. Shedid, S.A. and M.T. Ghannam, *Influences of droplet volume on contact angle of reservoir rocks.* Energy Sources, 2005. **27**(11): p. 1085-1097.

64. Perez-Diaz, J.L., et al., *On the Influence of Relative Humidity on the Contact Angle of a Water Droplet on a Silicon Wafer.* Proceedings of the Asme International Mechanical Engineering Congress and Exposition, 2013, Vol 7a, 2014.

65. Huh, C. and S.G. Mason, *Effects of Surface-Roughness on Wetting (Theoretical).* Journal of Colloid and Interface Science, 1977. **60**(1): p. 11-38.

66. Aslannezhad, M., et al., *A review of hydrogen/rock/brine interaction: Implications for Hydrogen Geo-storage.* Progress in Energy and Combustion Science, 2023. **95**.

67. Huhtamäki, T., et al., *Surface-wetting characterization using contact-angle measurements (vol 13, pg 1521, 2018).* Nature Protocols, 2019. **14**(7): p. 2259-2259.

68. Wood, M.J., et al., *Introducing a graphical user interface for dynamic contact angle determination.* Physics of Fluids, 2023. **35**(7).

69. Strobel, M. and C.S. Lyons, *An Essay on Contact Angle Measurements.* Plasma Processes and Polymers, 2011. **8**(1): p. 8-13.

70. Guo, Z.M., et al., *Effects of surface heterogeneities on wetting and contact line dynamics as observed with the captive bubble technique.* Colloids and Surfaces a-Physicochemical and Engineering Aspects, 2021. **615**.

71. Krasovitski, B. and A. Marmur, *Drops down the hill: Theoretical study of limiting contact angles and the hysteresis range on a tilted plate.* Langmuir, 2005. **21**(9): p. 3881-3885.

72. Extrand, C.W. and Y. Kumagai, *Liquid-Drops on an Inclined Plane - the Relation between Contact Angles, Drop Shape, and Retentive Force.* Journal of Colloid and Interface Science, 1995. **170**(2): p. 515-521.

73. ElSherbini, A. and A. Jacobi, *Retention forces and contact angles for critical liquid drops on non-horizontal surfaces.* Journal of Colloid and Interface Science, 2006. **299**(2): p. 841-849.

74. Extrand, C.W. and A.N. Gent, *Retention of Liquid-Drops by Solid-Surfaces.* Journal of Colloid and Interface Science, 1990. **138**(2): p. 431-442.

75. Pierce, E., F.J. Carmona, and A. Amirfazli, *Understanding of sliding and contact angle results in tilted plate experiments.* Colloids and Surfaces a-Physicochemical and Engineering Aspects, 2008. **323**(1-3): p. 73-82.

76. Harkins, W.D. and H.F. Jordan, *Surface tension by the ring method.* Science, 1930. **72**: p. 73-75.

77. du Noüy, P.L., *An interfacial tensiometer for universal use.* Journal of General Physiology, 1925. **7**(5): p. 625-U53.

78. Anastasiadis, S.H., I. Gancarz, and J.T. Koberstein, *Interfacial-Tension of Immiscible Polymer Blends - Temperature and Molecular-Weight Dependence.* Macromolecules, 1988. **21**(10): p. 2980-2987.

79. *Wu, S. (1982). Polymer Interface and Adhesion (1st ed.). Routledge.* .

80. Palmer, G. and N.R. Demarquette, *New procedure to increase the accuracy of interfacial tension measurements obtained by breaking thread method.* Polymer, 2003. **44**(10): p. 3045-3052.

81. Elemans, P.H.M., J.M.H. Janssen, and H.E.H. Meijer, *The Measurement of Interfacial-Tension in Polymer-Polymer Systems - the Breaking Thread Method.* Journal of Rheology, 1990. **34**(8): p. 1311-1325.

82. Drelich, J.W., et al., *Contact angles: history of over 200 years of open questions.* Surface Innovations, 2020. **8**(1-2): p. 3-27.

83. Suryadi, G.S., et al., *Surface free energy analysis of oil palm empty fruit bunches fiber reinforced biocomposites.* International Conference on Biomass: Technology, Application, and Sustainable Development, 2016, 2017. **65**.

84. Yuan, J., et al., *Study on oil-water separation of selective-wettability meshes with different Micro/Nano structures.* Colloids and Surfaces a-Physicochemical and Engineering Aspects, 2020. **584**.

85. Gao, H.P., et al., *Switchable Wettability Surface with Chemical Stability and Antifouling Properties for Controllable Oil-Water Separation.* Langmuir, 2019. **35**(13): p. 4498-4508.

86. Liu, Z.A., et al., *Fabrication of Wettability Mesh with Quasi-Rectangular-Restraining Capacity to Water.* Langmuir, 2019. **35**(28): p. 9177-9183.

87. Yang, H., et al., *Functional silica film on stainless steel mesh with tunable wettability.* Surface & Coatings Technology, 2011. **205**(23-24): p. 5387-5393.

88. Xu, C.L., *Surface modification to fabricate dual superlyophobic mesh for efficient oil/water separation (vol 273, 122872, 2020).* Journal of Cleaner Production, 2021. **295**.

89. Voniatis, C., et al., *Fabrication and characterisation of electrospun Polycaprolactone/Polysuccinimide composite meshes.* Journal of Molecular Liquids, 2021. **323**.

90. Catsoulis, S., et al., *Droplet impact on a wettability-patterned woven mesh.* Droplet, 2023. **2**(3): p. e53.

91. Bérard, A., et al., *Photo Initiated Chemical Vapour Deposition To Increase Polymer Hydrophobicity.* Scientific Reports, 2016. **6**.

92. Karthikeyan, A., et al., *Surface Modification of Commercially Available PLA Polymer Mesh.* Industrial & Engineering Chemistry Research, 2022. **61**(47): p. 17297-17305.

93. Carroll, B.J., *Accurate Measurement of Contact-Angle, Phase Contact Areas, Drop Volume, and Laplace Excess Pressure in Drop-on-Fiber Systems.* Journal of Colloid and Interface Science, 1976. **57**(3): p. 488-495.

94. Yamaki, J.I. and Y. Katayama, *New Method of Determining Contact Angle between Monofilament and Liquid.* Journal of Applied Polymer Science, 1975. **19**(10): p. 2897-2909.

95. KRÜSS. *Meniscus method*. [cited 2024; Available from: https://www.kruss-scientific.com/en.

96. Mason, S.G. and A. Okagawa, *Capillarography, a New Surface Probe.* Abstracts of Papers of the American Chemical Society, 1977. **173**(Mar20): p. 118-118.

97. Garat, W., et al., *Surface energy determination of fibres for Liquid Composite Moulding processes: Method to estimate equilibrium contact angles from static and quasi-static data.* Colloids and Surfaces a-Physicochemical and Engineering Aspects, 2021. **611**.

98. Bedarkar, A., X.F. Wu, and A. Vaynberg, *Wetting of liquid droplets on two parallel filaments.* Applied Surface Science, 2010. **256**(23): p. 7260-7264.

99. Wu, X.F., A. Bedarkar, and K.A. Vaynberg, *Droplets wetting on filament rails: Surface energy and morphology transition.* Journal of Colloid and Interface Science, 2010. **341**(2): p. 326-332.

100. Yoon, R.H., D.H. Flinn, and Y.I. Rabinovich, *Hydrophobic interactions between dissimilar surfaces.* Journal of Colloid and Interface Science, 1997. **185**(2): p. 363-370.

101. Berg, J.M., et al., *3-Component Langmuir-Blodgett-Films with a Controllable Degree of Polarity.* Langmuir, 1994. **10**(4): p. 1225-1234.

102. Vogler, E.A., *Structure and reactivity of water at biomaterial surfaces.* Advances in Colloid and Interface Science, 1998. **74**: p. 69-117.

103. Si, Y.F., et al., *Liquids Unidirectional Transport on Dual-Scale Arrays.* Acs Nano, 2018. **12**(9): p. 9214-9222.

104. Elzaabalawy, A. and S.A. Meguid, *Effect of surface topology on the wettability of superhydrophobic surfaces.* Journal of Dispersion Science and Technology, 2020. **41**(3): p. 470-478.

105. Liu, C., et al., *Design of superhydrophobic pillars with robustness.* Surface & Coatings Technology, 2019. **361**: p. 342-348.

106. Azimi, G., et al., *Hydrophobicity of rare-earth oxide ceramics.* Nature Materials, 2013. **12**(4): p. 315-320.

107. Handrea-Dragan, I.M., et al., *Patterning at the micro/nano-scale: Polymeric scaffolds for medical diagnostic and cell-surface interaction applications.* Colloids and Surfaces B-Biointerfaces, 2022. **218**.

108. Ammosova, L., K. Mönkkönen, and M. Suvanto, *Precise fabrication of microtextured stainless steel surfaces using metal injection moulding.* Precision Engineering-Journal of the International Societies for Precision Engineering and Nanotechnology, 2020. **62**: p. 89-94.

109. Papadopoulos, P., et al., *Wetting of soft superhydrophobic micropillar arrays.* Soft Matter, 2018. **14**(36): p. 7429-7434.

110. Kamegawa, T., K. Irikawa, and H. Yamashita, *Multifunctional surface designed by nanocomposite coating of polytetrafluoroethylene and TiO*

photocatalyst: self-cleaning and superhydrophobicity. Scientific Reports, 2017. **7**.

111. Wong, W.S.Y., et al., *Designing Plastrons for Underwater Bubble Capture: From Model Microstructures to Stochastic Nanostructures.* Advanced Science, 2024.

112. Si, Y.F., Z.C. Dong, and L. Jiang, *Bioinspired Designs of Superhydrophobic and Superhydrophilic Materials.* Acs Central Science, 2018. **4**(9): p. 1102-1112.

113. Lovincic Milovanovic, V., et al., *Modification of Surface Hydrophobicity of PLA/PE and ABS/PE Polymer Blends by ICP Etching and CF(x) Coating.* Materials (Basel), 2020. **13**(23).

114. Mohammadi, M.R., et al., *Production of PLA fibers with surface modifications and silver nanoparticle coating to impart antibacterial activity.* Polymer Bulletin, 2023.

115. Ye, Y., et al., *Engineering Environmentally Friendly Nanofiber Membranes with Superhydrophobic Surface and Intrapore Interfaces for Ultrafast Oil Dehydrating*. 2023, SSRN.

116. Chen, T.C., et al., *One-step fabrication of biodegradable superhydrophobic PLA fabric for continuous oil/water separation.* Applied Surface Science, 2022. **576**.

117. Hou, Y.Z., et al., *Review on Cell Structure Regulation and Performances Improvement of Porous Poly(Lactic Acid).* Macromolecular Rapid Communications, 2023. **44**(10).

118. Knoch, S., et al., *Dip-dip-dry: Solvent-induced tuning of polylactic acid surface properties.* Colloids and Surfaces a-Physicochemical and Engineering Aspects, 2019. **578**.

119. Verma, D. and K.L. Goh, *Effect of Mercerization/Alkali Surface Treatment of Natural Fibres and Their Utilization in Polymer Composites: Mechanical and Morphological Studies.* Journal of Composites Science, 2021. **5**(7).

120. Deivayanai, V.C., et al., *A comprehensive review on the biological conversion of lignocellulosic biomass into hydrogen: Pretreatment strategy, technology advances and perspectives.* Bioresource Technology, 2022. **365**.

121. Lin, L.N., et al., *Combination of Pre- and Post-Mercerization Processes for Cotton Fabric.* Materials, 2022. **15**(6).

122. Ferro, M., et al., *An Integrated Approach to Optimizing Cellulose Mercerization.* Polymers, 2020. **12**(7).

123. Sharma, H.S.S., et al., *Fine structure of chemically modified flax fibre.* Journal of the Textile Institute, 1995. **86**(4): p. 539-548.

124. Kim, J.T. and A.N. Netravali, *Mercerization of sisal fibers: Effect of tension on mechanical properties of sisal fiber and fiber-reinforced composites.* Composites Part a-Applied Science and Manufacturing, 2010. **41**(9): p. 1245-1252.

125. Brunnschweiler, D. and A.C. Parikh, *YARN-TENSION MEASUREMENT.* Journal of the Textile Institute Proceedings 2009: p. P63-P73.

126. Iwade, T., et al., *Quality Control Technology for Synthetic Fiber Manufacturing Process by Non-Contact Tension Meter Part 2: Non-Contact Measuring System for Running Yarn Tension.* Journal of the Textile Machinery Society of Japan, 2000. **53**: p. 15-24.

127. Larry S. Satterfield, M., S.C., *APPARATUS TO MEASURE YARN TENSION*, U.S. Patent, Editor. 1983, Milliken Research Corporation, Spartanburg, S.C.: United States.

128. Wang, T.Y., et al., *Development of a new low-cost instrument for dynamic friction coefficient measurement of yarns based on the entanglement method.* Journal of the Textile Institute, 2022. **113**(10): p. 2068-2079.

129. Mai, F., et al., *The Influence of Solid-State Drawing on Mechanical Properties and Hydrolytic Degradation of Melt-Spun Poly(Lactic Acid) (PLA) Tapes.* Fibers, 2015. **3**(4): p. 523-538.

130. Oksman, K., M. Skrifvars, and J.F. Selin, *Natural fibres as reinforcement in polylactic acid (PLA) composites.* Composites Science and Technology, 2003. **63**(9): p. 1317-1324.

131. Sadasivuni, K.K., et al., *Recent advances in mechanical properties of biopolymer composites: a review.* Polymer Composites, 2020. **41**(1): p. 32-59.

132. Schwarcz, J., *The Right Chemistry: Breaking down bioplastics' benefits and problems*. 2024, The Montreal Gazette.: The Montreal Gazette.

133. Swetha, T.A., et al., *A review on biodegradable polylactic acid (PLA) production from fermentative food waste- Its applications and degradation.* International Journal of Biological Macromolecules, 2023. **234**.

134. Dana, H.R. and F. Ebrahimi, *Synthesis, properties, and applications of polylactic acid-based polymers.* Polymer Engineering and Science, 2023. **63**(1): p. 22-43.

135. Gkountela, C.I. and S.N. Vouyiouka, *Enzymatic Polymerization as a Green Approach to Synthesizing Bio-Based Polyesters.* Macromol, 2022. **2**(1): p. 30-57.

136. Avérous, L., *Polylactic Acid: Synthesis, Properties and Applications*, in *Monomers, Polymers and Composites*

from Renewable Resources, A.G. Mohamed Naceur Belgacem, Editor. 2008, Elsevier: Elsevier. p. p 433-450.

137. A. J. Müller, e.a., *Crystallization of PLA-based Materials.* RSC Polymer Chemistry Series No. 12. **Chapter 3**.

138. Ghomi, E.R., et al., *The Life Cycle Assessment for Polylactic Acid (PLA) to Make It a Low-Carbon Material.* Polymers, 2021. **13**(11).

139. Ranakoti, L., et al., *Critical Review on Polylactic Acid: Properties, Structure, Processing, Biocomposites, and Nanocomposites.* Materials, 2022. **15**(12).

140. Benavides, P.T., U. Lee, and O. Zarè-Mehrjerdi, *Life cycle greenhouse gas emissions and energy use of polylactic acid, bio-derived polyethylene, and fossil-derived polyethylene.* Journal of Cleaner Production, 2020. **277**.

141. Bher, A., E. Castro-Aguirre, and R. Auras, *END-OF-LIFE SCENARIOS FOR POLY(LACTIC ACID)*, in *Poly(Lactic Acid): Synthesis, Structures, Properties, Processing, Applications, and End of Life*, L.-T.L. Rafael A. Auras, Susan E. M. Selke, and Hideto Tsuji, Editor. 2022, John Wiley & Sons: John Wiley & Sons.

142. Morao, A. and F. de Bie, *Life Cycle Impact Assessment of Polylactic Acid (PLA) Produced from Sugarcane in Thailand.* Journal of Polymers and the Environment, 2019. **27**(11): p. 2523-2539.

143. Yasin, N.M., S. Akkermans, and J.F.M. Van Impe, *Enhancing the biodegradation of (bio)plastic through pretreatments: A critical review.* Waste Management, 2022. **150**: p. 1-12.

144. Benn, N. and D. Zitomer, *Pretreatment and Anaerobic Co-digestion of Selected PHB and PLA Bioplastics.* Frontiers in Environmental Science, 2018. **5**.

145. Shrestha, A., M.C.A.A.V. Jansen, and B. Acharya, *Biodegradation of Bioplastic Using Anaerobic Digestion at Retention Time as per Industrial Biogas Plant and International Norms.* Sustainability, 2020. **12**(10).

146. Kalogirou, C., et al., *Assessing the Time Dependence of AOPs on the Surface Properties of Polylactic Acid.* Journal of Polymers and the Environment, 2023. **31**(1): p. 345-357.

147. Ren, Y., et al., *Effect of dielectric barrier discharge treatment on surface nanostructure and wettability of polylactic acid (PLA) nonwoven fabrics.* Applied Surface Science, 2017. **426**: p. 612-621.

148. Jeon, H.J. and M.N. Kim, *Biodegradation of poly(L-lactide) (PLA) exposed to UV irradiation by a mesophilic bacterium.* International Biodeterioration & Biodegradation, 2013. **85**: p. 289-293.

149. OECD, *Global Plastics Outlook*. 2022.

150. PlasticsEurope. *The Circular Economy for Plastics – A European Overview 2022*. 2023 [cited 2024; Available from: https://plasticseurope.org/.

151. World Economic Forum, E.M.F.a.M.C., The New Plastics Economy: Rethinking the future of plastics (2016).

152. *United Nations Environment Programme (2021). From Pollution to Solution: A global assessment of marine litter and plastic pollution. Nairobi. .*

153. Ambrosini, R., et al., *First evidence of microplastic contamination in the supraglacial debris of an alpine glacier.* Environmental Pollution, 2019. **253**: p. 297-301.

154. Sfriso, A.A., et al., *Microplastic accumulation in benthic invertebrates in Terra Nova Bay (Ross Sea, Antarctica).* Environment International, 2020. **137**.

155. Boelee, E., et al., *Water and health: From environmental pressures to integrated responses.* Acta Tropica, 2019. **193**: p. 217-226.

156. Wyles, K.J., et al., *Factors That Can Undermine the Psychological Benefits of Coastal Environments: Exploring the Effect of Tidal State, Presence, and Type of Litter.* Environment and Behavior, 2016. **48**(9): p. 1095-1126.

157. Ragusa, A., G. Principi, and M. Matta, *Pregnancy in the Era of the Environmental Crisis: Plastic and Pollution.* Clinical and Experimental Obstetrics & Gynecology, 2022. **49**(10).

158. Schwarcz, J., *Plastic, You Say?* . General Science, Office for Science and Society, McGill University, 2022.

159. D6400-21, A.S., *Standard Specification for Labeling of Plastics Designed to be Aerobically Composted in Municipal or Industrial Facilities.* ASTM International, West Conshohocken, PA, 19428-2959 USA, 2023.

160. Drumright, R.E., P.R. Gruber, and D.E. Henton, *Polylactic acid technology.* Advanced Materials, 2000. **12**(23): p. 1841-1846.

161. Wietecha, J., J. Kazimierczak, and A. Jeziorna, *Effect of the Surface modification of Cellulose nanofibers on the Mechanical Properties and Disintegrability of Specific PLA/Cellulose Composites.* Fibres & Textiles in Eastern Europe, 2023. **31**(6): p. 15-29.

162. Pisuchpen, T., et al., *Tuning Hydrophobicity and Water Adhesion by Electrospinning and Silanization.* Langmuir, 2011. **27**(7): p. 3654-3661.

163. Suzuki, F., et al., *Direct measurement of 185 nm radiation from low-pressure mercury lamps using diamond-based vacuum ultraviolet sensors.* Japanese Journal of Applied Physics Part 1-Regular Papers Brief Communications & Review Papers, 2006. **45**(8a): p. 6484-6485.

164. Koo, G.H. and J. Jang, *Surface modification of poly(lactic acid) by UV/Ozone irradiation.* Fibers and Polymers, 2008. **9**(6): p. 674-678.

165. Karthikeyan, A., et al., *Tuning Surface Properties of PLA for Capturing Nonpolar Compounds from Water.* Industrial & Engineering Chemistry Research, 2024. **63**(38): p. 16376-16385.

166. Ikada, E., *Photo- and Bio-degradable Polyesters. Photodegradation Behaviors of Aliphatic Polyester.* Journal of Photopolymer Science and Technology, 1997. **10**: p. 265-270.

167. Ho, K.L.G. and A.L. Pometto, *Effects of electron-beam irradiation and ultraviolet light (365 nm) on polylactic acid plastic films.* Journal of Environmental Polymer Degradation, 1999. **7**(2): p. 93-100.

168. Ikada, E., A. Tanahashi, and N. Morisaka, *Relationship between Photo Degradability of Polyesters and Their Molecular-Structures - Photo Degradability of a Polyester Having Phenylene Groups in the Chain Skeleton.* Kobunshi Ronbunshu, 1995. **52**(8): p. 472-477.

169. O'Shaughnessy, W.S., S. Baxamusa, and K.K. Gleason, *Additively patterned polymer thin films by photo-initiated chemical vapor deposition (piCVD).* Chemistry of Materials, 2007. **19**(24): p. 5836-5838.

170. Yousif, E. and R. Haddad, *Photodegradation and photostabilization of polymers, especially polystyrene: review.* Springerplus, 2013. **2**.

171. H.-Y. NIE, M.J.W.a.N.S.M., *Polymer Surface Modification: Relevance to Adhesion, Chapter: Atomic force microscopy study of UV/ozone treated polypropylene films*, ed. s. Edition. Vol. 2 2000, CRC Press. 16.

172. Dodiuk, H., et al., *UV treatment of surfaces with excimer lasers and its effect on adhesion properties.* First International Congress on Adhesion Science and Technology - Invited Papers, 1998: p. 387-405.

173. Olewnik-Kruszkowska, E., et al., *Degradation of polylactide composites under UV irradiation at 254 nm.* Journal of Photochemistry and Photobiology a-Chemistry, 2015. **311**: p. 144-153.

174. Bocchini, S., et al., *Polylactic Acid and Polylactic Acid-Based Nanocomposite Photooxidation.* Biomacromolecules, 2010. **11**(11): p. 2919-2926.

175. Janorkar, A.V., A.T. Metters, and D.E. Hirt, *Degradation of Poly(L-Lactide) films under ultravioletInduced photografting and sterilization conditions.* Journal of Applied Polymer Science, 2007. **106**(2): p. 1042-1047.

176. Zaidi, L., et al., *Effect of natural weather on the structure and properties of polylactide/Cloisite 30B nanocomposites.* Polymer Degradation and Stability, 2010. **95**(9): p. 1751-1758.

177. Bao, Q., et al., *Accelerated Degradation of Poly(lactide acid)/Poly(hydroxybutyrate) (PLA/PHB) Yarns/Fabrics by UV and O2 Exposure in South China Seawater.* Polymers, 2022. **14**(6).

178. Sato, S., et al., *Effects of irradiation with vacuum ultraviolet xenon excimer lamp at 172 nm on water vapor transport through poly(lactic acid) membranes.* Desalination, 2012. **287**: p. 290-300.

179. Tertyshnaya, Y.V. and M.V. Podzorova, *Effect of UV Irradiation on the Structural and Dynamic Characteristics of Polylactide and Its Blends with Polyethylene.* Russian Journal of Physical Chemistry B, 2020. **14**(1): p. 167-175.

180. Copinet, A., et al., *Effects of ultraviolet light (315 nm), temperature and relative humidity on the degradation of polylactic acid plastic films.* Chemosphere, 2004. **55**(5): p. 763-773.

181. Lesaffre, N., et al., *Recent advances on the ageing of flame retarded PLA: Effect of UV-light and/or relative humidity.* Polymer Degradation and Stability, 2017. **139**: p. 143-164.

182. Smith, B.C., *IR Spectral Interpretation Workshop. The Infrared Spectroscopy of Alkenes.* Spectroscopy, 2016. **31**(11): p. 28-+.

183. Ahmed A. Afifi, R.A.Y.a.H., *Fourier transform infrared spectroscopy study on early stage of salt stress in Jojoba plant.* Life Science Journal, 2013. **10**: p. 1973-1981.

184. Arwa Turki, A.E.O., Slah Msahli and Faouzi Sakli, *Infrared Spectra for Alfa Fibers Treated with Thymol.* J Glycobiol, 2018. **7**.

185. Stevie, F.A. and C.L. Donley, *Introduction to x-ray photoelectron spectroscopy.* Journal of Vacuum Science & Technology A, 2020. **38**(6).

186. Aguilar, Z.P., *Nanomaterials for Medical Applications, Chapter 2 - Types of Nanomaterials and Corresponding Methods of Synthesis*. 2013, Elsevier.

187. Minnes, R., et al., *Using Attenuated Total Reflection-Fourier Transform Infra-Red (ATR-FTIR) spectroscopy to distinguish between melanoma cells with a different metastatic potential.* Scientific Reports, 2017. **7**.

188. Li, D.W., et al., *Large-scale fabrication of durable and robust super-hydrophobic spray coatings with excellent repairable and anti-corrosion performance.* Chemical Engineering Journal, 2019. **367**: p. 169-179.

189. Ren, Y.P., et al., *Hydrocarbon plasma for treatment of biodegradable food containers.* Ieee Transactions on Plasma Science, 2008. **36**(4): p. 1306-1307.

190. Zhang, C.M., et al., *Melt Crystallization Behavior and Crystalline Morphology of Polylactide/Poly(ε-caprolactone) Blends Compatibilized by Lactide-Caprolactone Copolymer.* Polymers, 2018. **10**(11).

191. Brassard, D., M. Dubé, and J.R. Tavares, *Modelling resistance welding of thermoplastic composites with a nanocomposite heating element.* Journal of Composite Materials, 2021. **55**(5): p. 625-639.

192. Dever, J., et al., *Simulated space vacuum ultraviolet (VUV) exposure testing for polymer films*, in *39th Aerospace Sciences Meeting and Exhibit*.

193. Flury, M. and R. Narayan, *Biodegradable plastic as an integral part of the solution to plastic waste pollution of the environment.* Current Opinion in Green and Sustainable Chemistry, 2021. **30**.

194. Adhikari, D., et al., *Degradation of Bioplastics in Soil and Their Degradation Effects on Environmental Microorganisms.* Journal of Agricultural Chemistry and Environment, 2016. **5**: p. 23-34.

195. Ebnesajjad, S., *Chapter 2 - Surface Tension and Its Measurement*, in *Surface Treatment of Materials for Adhesive Bonding (Second Edition)*, S. Ebnesajjad, Editor. 2014, William Andrew Publishing: William Andrew Publishing. p. 7-24.

196. Guicherd, M., et al., *An engineered enzyme embedded into PLA to make self-biodegradable plastic.* Nature, 2024. **631**(8022): p. 884-890.

197. Qi, H., et al., *Low-temperature dyeing performance of polylactic acid fabrics pretreated with natural deep eutectic solvent.* Journal of Cleaner Production, 2024. **434**.

198. Boruvka, L. and A.W. Neumann, *Generalization of Classical-Theory of Capillarity.* Journal of Chemical Physics, 1977. **66**(12): p. 5464-5476.

199. Otts, D.B., E. Heidenreich, and M.W. Urban, *Novel waterborne UV-crosslinkable thiol-ene polyurethane dispersions: Synthesis and film formation.* Polymer, 2005. **46**(19): p. 8162-8168.

APPENDIX A ASSUMPTION OF WETTABILITY MODELS

One of the hypotheses of the Cassie-Baxter and Wenzel models is that they are founded on the Young's equation. This equation derived from the balanced force equation on a droplet neglects the line tension Γ at the three-phase interface. This assumption is not valid for droplet of the micrometric scale or smaller. In this case, the contribution of the triple line $\frac{\Gamma}{r_{drop}}$ should be also accounted in the force balance with r_{drop} being the contact radius illustrated in Figure 2.1. This equation is known as the Neumann-Boruvka's equation [54, 198]:

$$\gamma_{sg} - \gamma_{sl} - \gamma_{lg}\cos(\theta) - \frac{\Gamma}{r_{drop}} = 0$$

$$\cos(\theta) = \frac{\gamma_{sg} - \gamma_{sl}}{\gamma_{lg}} - \frac{\Gamma}{\gamma_{lg} r_{drop}}$$

APPENDIX B SUPPLEMENTARY INFORMATION ARTICLE

Section 1: Research in biodegradable and compostable materials since 1952

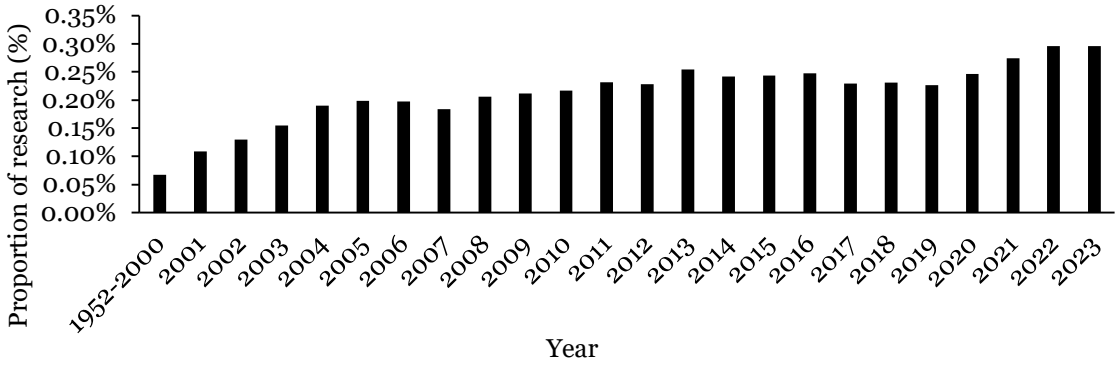

Figure B.1: Proportion of papers published in the research area of compostable and biodegradable plastics extracted from the Engineering Village Navigator (August 2024, using request: ((Biodegradable OR compost*) AND (polymer* OR plastic*)) over total number of paper published per year

Section 2: Molecular weight obtained from GPC results

UV is known to induce cross-linking. For example, using a UVC lamp with an emission peak at 254 nm, Otts et al. [199] have shown that crosslinking could occur when exposing thiol–ene polyurethane dispersions. Cross-linking is typically associated with the formation of higher molecular weight compounds, which should appear in the molecular weight distribution given by GPC. However, as shown in Figure B.2, the molecular weight distribution for the discs does not exhibit such higher-molecular-weight compounds. To verify whether larger molecular weight species were filtered prior to GPC analysis of the UV-exposed material, a dissolution test was performed. A solution was prepared using 30 mg of UV-exposed DDD-treated powder dissolved in THF and chloroform, both known as effective solvents for PLA. The solution was filtered through a 0.4 µm filter, and the residual mass on the filter was measured after evaporation of remaining solvent. For both THF and chloroform, approximately 4 wt.% of the material remained

on the filter. This figure is deemed to be low compared to the significant reduction observed in both number and weight average molecular weight. However, molecular weight values presented in the main body of article may thus be slightly underestimated. As such, the reported values should only be considered as an indication of chain scission occurring under the effect of UV on the surface. This conclusion is strengthened by a greater molecular weight reduction observed when comparing the first 20 µm of the surface with the whole disc exposed on both sides, or the powder as shown in Table 4.3. Molecular weight values for UV-exposed samples should not be interpreted beyond their use as an indication of surface-level chain scission.

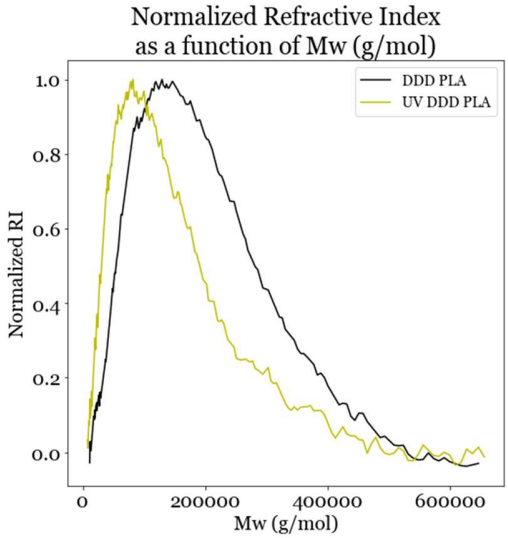

Figure B.2: GPC distribution for DDD-treated and 2h UVC exposed DDD-treated PLA discs

Section 3: DTG curves for DDD-treated and UV DDD-treated PLA discs

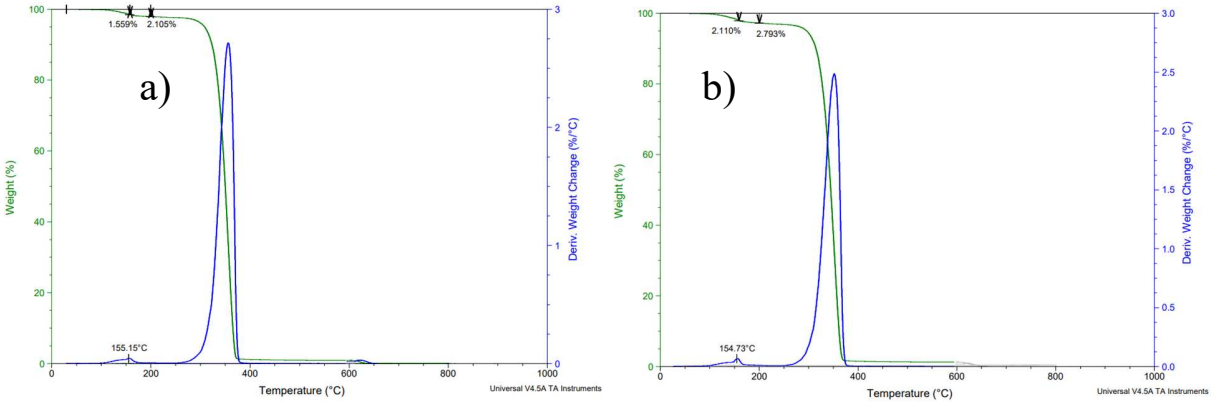

Figure B.3: TGA and DTG curves for a) DDD-treated and b) 2h UVC exposed DDD-treated PLA

Section 4: XRD and DSC results on powders

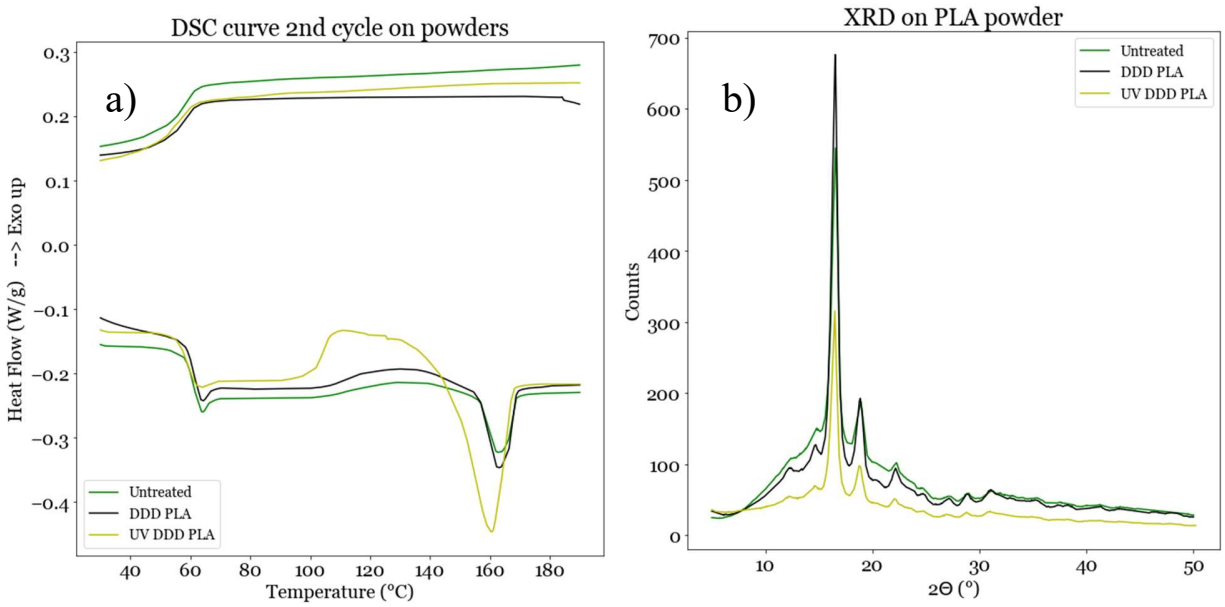

Figure B.4: a) DSC and b) XRD curves for Untreated (neat), DDD-treated and 2h UVC exposed DDD-treated PLA powders

Table B.1: Crystallinity rate χ_c obtained from DSC and XRD for Untreated (neat), DDD-treated and 2h UVC exposed DDD-treated PLA powders

Samples	Neat	DDD	UV DDD
χ_c DSC (%)	30.6 (± 0.1)	29.9 (± 0.8)	33.2 (± 2.5)
χ_c XRD (%)	18.6 (± 0.5)	31.5 (± 2.1)	34.4 (± 5.2)
Melting T° (DSC) (°C)	163.5 (± 0.7)	165.4 (± 0.1)	162.0 (± 0.1)

APPENDIX C SEM IMAGES OF TREATED MONOFILAMENT YARN AT 140 °C

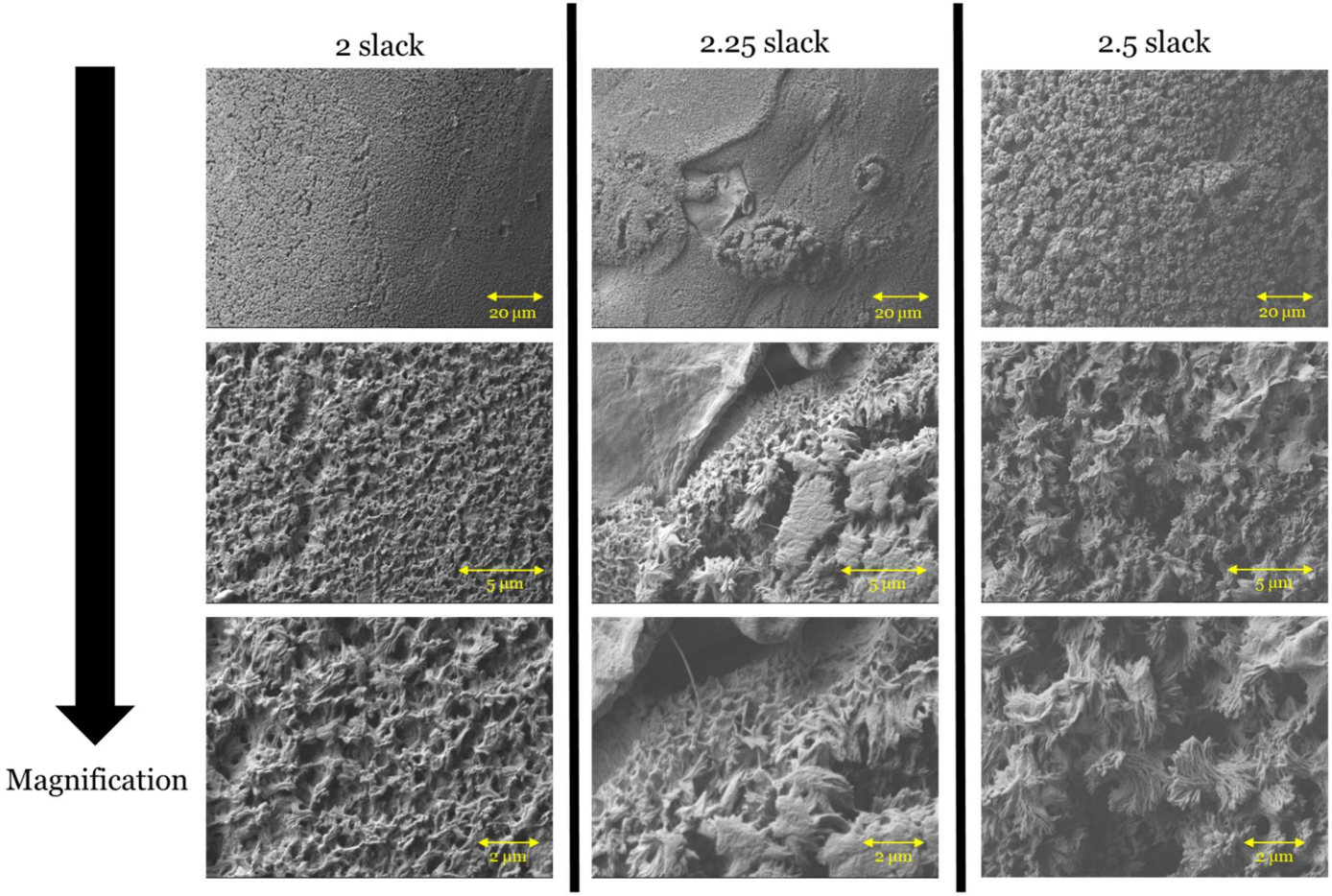

Figure C.1: High resolution SEM images of DDD-treated monofilament yarn with slack values of 2, 2.25, 2.5 using the U-bar process

APPENDIX D WETTABILITY TESTS ON YARNS

Several methods were tested to compare the wettability of the monofilament yarns treated with different slack. First method tested was inserting the yarn in the water contained in a transparent quartz and removing it, like in the Wilhelmy method to get the ACA and the RCA. This method is described as Method 1 and as seen in Figure below, the RCA is visible but not the ACA due to diffraction near the water surface. Same disadvantage has been encountered when putting the yarn in a drop of water instead of a bath. In Method 2, the yarn is curved to form a U-shape and dipped it in a pool of water contained in a transparent quartz. This method does not help in characterizing wettability as the untreated and the DDD-treated (with a slack value of 2) monofilament yarns hold the same contact angle. Finally, Method 3 is the experimental setup corresponding to the work of Bedarkar et al. [98] introduced in the literature review regarding laying a droplet on two parallel yarns and calculating the contact angle based on the wetting length observed. In practice the wetting length can be observed using a perpendicular view of the droplet between the two yarns. A second camera can be used to verify the view parallel to the fibers axis and confirm the shape of the droplet (droplet-bridge or barrel-shaped). These two last methods were the result of two interns, Noémie Lemoine and Isabella Smith. Future work will consist of measuring the wetting length on perpendicular view images for each samples, transcribing it to a real length using pixels/cm ratio of the video, and finally calculating the contact angles based on Bedarkar et al. work.

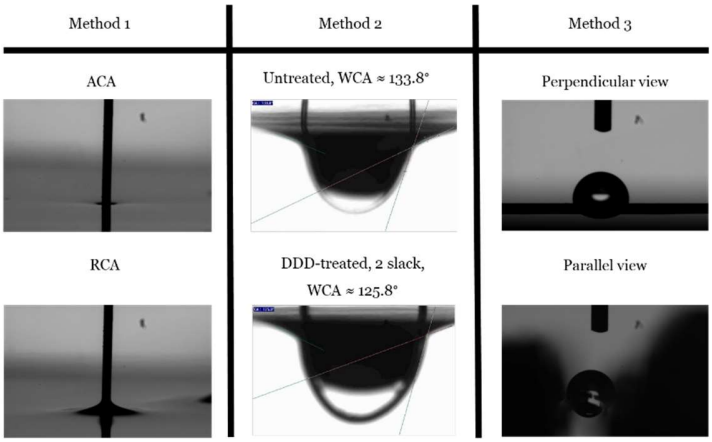

Figure D.1: Images illustrating the different methods tried to assess the wettability of a yarn. For Method 1 and 3 yarn treated with 2 slack was used

APPENDIX E DETAILS OF SOLAR SIMULATOR EXPERIMENT

According to Global Solar Atlas 2.0, map below represents direct normal solar irradiation.

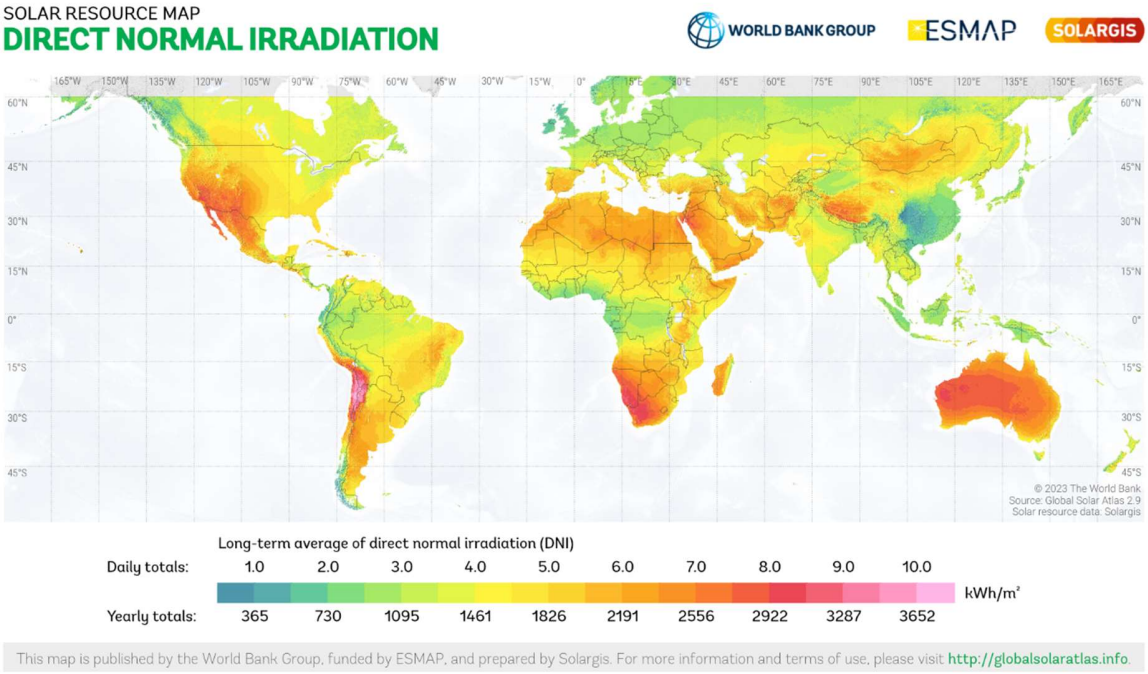

Figure E.1: Solar resource Map/Direct Normal Irradiation obtained from the "Global Solar Atlas 2.0, a free, web-based application is developed and operated by the company Solargis s.r.o. on behalf of the World Bank Group, utilizing Solargis data, with funding provided by the Energy Sector Management Assistance Program (ESMAP).As such, in France or in Canada we can see that regions are mostly in light green (3.5-4 kWh/m²/day) or yellow (4-4.5 kWh/m²/day). Some specific regions (on the edge of France South-East and near Calgary) seem to reach 5 kWh/m²/day. If we consider case of 4 kWh/m²/day, which globally represents well both countries, and we transform into our working unit (J/cm²/day), we get 1440 J/cm²/day. A year would then represent: 1440*365 = 525600 J/cm²/year. Solar simulator has an irradiance of 0.1 W/cm², which means that 24h exposure would represent an energetic dose of 8640 J/cm²/day. As such, a year outside means 525600/8640 ≈ 60.83 days in the simulator. Based on same data but with the yearly value 1461 kWh/m²/year we get 525960 J/cm²/year. Same as above, a year outside then represents: 525960/8640=60.88 days in the simulator which is a very minor

difference. The table below summarizes number of days in the simulator to represent irradiance values ranging from 3.5 to 5 kWh/m²/day.

Table E.1: Number of days in the simulator depending on daily average irradiance.

Irradiance per day (kWh/m²/day)	3.5	4	4.5	5
Days in the simulator to simulate a year (days)	53.23	60.83	68.44	76.04
Days in the simulator to simulate 4 months (days)	**17.74**	**20.28**	**22.81**	**25.35**

There are two major drawback to this method. First, monthly variation is not taken into account. If nets are supposed to be used during the 4 months period May – June – July – August, then we need to target exactly the average irradiance of these months (taking into account irradiance variation depending on the month). In Table 1, when we consider 4 months of exposure, we divide by three the average yearly energetic dose, which is under the hypothesis that every month has the same energetic dose which is not true. The other major downside is that only direct normal irradiance is considered.

As such another method was used to determine the equivalent time of exposure (correlation between time inside the simulator and time outside under sun exposure based on same energetic dose). IRDA, our field-testing partner, is located at Saint-Bruno de Montarville. As shown in the image below extracted from Solar Calculator website on Saint-Bruno de Montarville datasheet, these 4 months represent 45.0% of the yearly average solar irradiance.

Table E.2: Monthly solar irradiance throughout one year (exact year of measurement unknown)

Solar irradiance at optimal angle 39°		
Month	**Average Daily kWh/m²/d**	**Average Monthly kWh/m²/mo**
January	2.68	83
February	3.2	89.53
March	4.31	133.57
April	4.97	149.24
May	**5.52**	**171.16**
June	**5.49**	**164.68**
July	**5.81**	**180.04**
August	**5.59**	**173.33**
September	4.76	142.93
October	3.32	103.04
November	2.76	82.9
December	1.86	57.75
	Total yearly	**1531.19**

Focusing on May-August period, energetic dose during this 4-months-period is 689.21 kWh/m² which means 248115.6 J/cm². Same principle as before, solar simulator has an irradiance of 0.1 W/cm², which means that 24h exposure would represent an energetic dose of 8640 J/cm²/day. As such, exposure during May-August period can be simulated by 248115.6/8640 ≈ **28.72 days** in the simulator. To compare with Montreal datasheet, May-August 4-month-period represents 43.7% of the yearly average solar irradiance and would mean 28.40 days in the simulator.

To conclude on this topic, May-August equivalent energetic dose was deemed to represent 28.72 days in the solar simulator, whereas less precise equivalent correlation was used for monthly equivalent with the method based on 4 kWh/m²/day figure: 1 month equivalent being 5.07 days, 2 months equivalent being 10.14 days, 3 months equivalent being 15.21 days, and 4 months equivalent being 20.28 days in the solar simulator.